Investigations on development customized Shape memory alloy structures using Wire Arc Based Additive Manufacturing and Laser based Additive Manufacturing

A Thesis

Submitted in partial fulfillment of the

Requirements for the award of the degree

of

DOCTOR OF PHILOSOPHY

By

Shalini Singh

(1901103006)

DISCIPLINE OF MECHANICAL ENGINEERING

INDIAN INSTITUTE OF TECHNOLOGY INDORE

May 2023

INDIAN INSTITUTE OF TECHNOLOGY INDORE

CANDIDATE'S DECLARATION

I hereby certify that the work which is being presented in the thesis entitled **"Investigations on development customized Shape memory alloy structures using Wire Arc Based Additive Manufacturing and Laser based Additive Manufacturing"** in the partial fulfillment of the requirements for the award of the degree of **Doctor of Philosophy** and submitted in the **Discipline of Mechanical Engineering, Indian Institute of Technology Indore**, is an authentic record of my own work carried out during the time period from July 2019 to Nov 2022 under the supervision of **Prof. I. A. Palani**, Professor, Discipline of Mechanical Engineering, Indian Institute of Technology Indore and **Dr. C. P. Paul**, Head, LAM lab, Laser Development Industrial Applications Division, Raja Ramanna Center for Advanced Technology Indore.

The content presented in this thesis has not been submitted by me for the award of any other degree of this or any other institute.

Shalini Singh
19/5/2023

Signature of the student with date

This is to certify that the above statement made by the candidate is correct to the best of our knowledge.

19/5/2023

Signature of Thesis Supervisor #1
(Prof. I.A. Palani)
Date:19/05/2023

Signature of Thesis Supervisor #2
(Dr. C.P. Paul)
Date:19/05/2023

Shalini Singh has successfully given her PhD Oral Examination held on 19/05/2023.

Signature(s) of DPGC Convener
Date: 19/05/2023

Signature of PSPC Member# 1
Date: 19/05/2023

22/05/23

Signature of PSPCMember #2
Date: 22/05/2023

ACKNOWLEDGEMENTS

It gives me great pleasure to express my regards and profound gratitude to my project supervisor Prof. I.A. Palani (IIT Indore), Dr. C.P. Paul (RRCAT, Indore) for their expert guidance and unflinching support throughout project work. I am highly indebted to them for their painstaking attention to my project and the innumerable number of improvements suggested by them, which helped me, shapes my project to perfection. Also, i would like to thank my PSPC members Dr. Eswara Prasad Korimilli and Dr. Girish Verma for their guidance and cooperation. I would like to thank Prof. Suhas Joshi, Director of IIT Indore for the opportunity and support to conduct my research. I would like to thank Nanofab lab of University of Alberta, Canada, Taltech Characterization Facility of Taltech, Estonia, and Sophisticated Instrumentation Centre of IIT Indore for their support in providing characterization facilities. Special thanks to Dr. Jinoop, Dr. Mani Prabhu and Dr. Manikandan, Saurabh Nayak for always motivating me and this work was not possible without their help.

I am really grateful to Dr. Ahmed Qureshi (University of Alberta, Canada), Prof. K.G. Prasanth (Taltech, Estonia), Prof. Natalia Resnina (St. Peterburg State University) and Dr. A. Funk (Federal Institute for Materials Research and Testing Berlin, Germany) who provided me a helping hand by allowing me to undergo this interesting learning experience and always been a source of inspiration for me. I would like to thank all the faculty members of the department for providing me with all the required information and cooperation which played a vital role in the completion of my project on time. I would gratefully acknowledge the financial aid support received from Ministry of Human Resource and Development, European funding ASTRA 06 and OVDF SERB.

I would like to thank to all the researchers specially Dr. Jayachandran, Sunil Yadav, Deelip Kumar and Anshu Sahu for their suggestions and help during experiments.

I would also like to thanks my parents, friends and God for their support and strong belief in me. Special thanks to Richa Singh, Rohit and Gandharv Sharma for always being source of entertainment and support for me throughout my PhD.

SHALINI SINGH

PREFACE

Shape memory alloys (SMAs) have gained significant attention in recent years due to their unique properties, including shape recovery, superelasticity, and high damping capacity. These properties make SMAs ideal for use in a wide range of applications, including biomedical implants, aerospace structures, civil structures, and MEMS devices, among others. However, SMAs have their limitations, including hysteresis and a limited life cycle, which have restricted their use in bulk structures. To overcome these limitations, SMA porous structures have been developed, which have shown promise in biomedical implants and vibration dampers for civil structures, machineries, and automobiles.

This thesis focuses on the development of SMA integrated bulk samples using different Additive Manufacturing (AM) methods, such as wire and powder-based systems. The main aim is to develop an alternative manufacturing route for the fabrication of NiTi-based alloys and bimetallic shape memory composites with enhanced mechanical and shape recovery properties.

The use of Wire Arc Additive Manufacturing for SMA integrated porous structure fabrication has been challenging due to issues such as weld pool instability, heat accumulation effect, residual stress, spatter, and distortion. In this work, a laser hybrid system has been used to address these issues, and various parameters such as surface roughness, interpass temperature control, interlayer delay, and preheating have been optimized to improve the microstructural, structural, and mechanical properties of the samples.

Moreover, this thesis explores the use of Cu-based shape memory alloys as an alternative to Ti-based SMAs, which have some disadvantages, such as high cost and production costs. The study investigates the use of Selective Laser Melting and Hot Isostatic Pressing for the fabrication of CuAlNiMn integrated bulk samples, and the resulting morphological, structural, and mechanical properties have been investigated.

Overall, this thesis provides a comprehensive study of the development of SMA integrated bulk samples and bimetallic shape memory composites, along with an exploration of alternative manufacturing routes to improve the properties of SMAs.

ABSTRACT

Shape memory alloys (SMA) have been extensively studied for their unique properties and potential applications in various fields, including damping and vibration control systems, MEMS devices, and biomedical implants. However, their widespread use in bulk structures is limited due to flaws such as strong hysteresis and reduced life cycle. In this work, SMA integrated bulk samples have been prepared using various Additive Manufacturing (AM) methods, such as wire and powder-based systems. A novel approach to fabricating SMA porous structures using Wire Arc Additive Manufacturing has been explored, which was challenging due to issues such as weld pool instability, heat accumulation, residual stress, spatter, and distortion. A laser hybrid system has been used to address these issues by reducing surface roughness (from 24 µm to 2.8 µm) and enhancing mechanical properties and shape recovery (up to 2.4 mm of displacement). Interpass temperature control (200º C-400º C) and interlayer delay (10s-30s) have also been employed to reduce heat accumulation and residual stress and improve mechanical properties such as hardness (802 HV) and tensile strength (900 MPa). Microstructural, structural, and phase transformation analysis have been performed, along with a study of the mechanical properties and shape recovery behavior.

Bimetallic shape memory composites have been developed using NiTi as an active layer and other materials such as stainless steel, titanium, and copper as a passive layer. The influence of Wire Arc Additive Manufacturing (WAAM) on the grain structure, chemical composition, phase composition, and phase transitions in these composites has been investigated. The mechanical properties of these composites, including hardness (600 HV (NiTi-Ti), 410 HV (NiTi-Cu), 400 HV (NiTi-SS)), and compressive strength (750 (NiTi-Ti), 950 (NiTi-Cu), 570 MPa (NiTi-SS)) have been enhanced due to the formation of brittle intermetallic compounds at the interface.

Copper-based shape memory alloys (CuAlNiMn) have been fabricated using Laser Powder Bed Fusion (LPBF) and elemental powder through ball milling. Parameters such as power (300W-400 W) and scanning speed (100mm/s-300 mm/s) have been optimized. The highest density (99%) and good mechanical properties (Hardness- 590 HV and Tensile strength- 1600 MPA) have been achieved for the sample fabricated at 350 W and 100 mm/s. Hot Isostatic Pressing (HIP) has been employed to further enhance the density and mechanical properties of the

samples. The HIP temperature has been optimized (950°C-1250°C) with respect to relative density, morphology, and mechanical properties.

These findings have significant implications for the development and use of SMA-based materials in various fields. The results demonstrate the potential for SMA integrated bulk samples, bimetallic shape memory composites, and copper-based shape memory alloys, which can be fabricated using Additive Manufacturing techniques, to enhance mechanical properties and shape recovery behavior, thereby increasing their potential for use in various applications.

List of Publications

Journals

- Investigations on NiTi Shape memory alloy thin wall structures through Laser Marking Assisted Wire Arc Based Additive Manufacturing –**Shalini Singh** Natalia Resnina, S Balyev, I.A. Palani, C. P., S. Paul, Sk. Bindra - Journal of Manufacturing Processes, https://doi.org/10.1016/j.jmapro.2021.04.004 (Impact Factor -5.6)
- Wire Arc Additive Manufacturing of NiTi 4D Structures: Influence of Interlayer Delay Period on the Mechanical Properties, Microstructure, and Shape Memory Behavior- **Shalini Singh** , Alex , I. A. Palani, C.P. Paul , K.G. Prasanth -Journal of 3d Printing and Additive Manufacturing https://doi.org/10.1089/3dp.2021.0296 (Impact Factor -5.4)
- Mechanical Properties, Microstructure and Actuation Behavior of Wire Arc Additive Manufactured Nitinol - Titanium Bimetallic Structures- **Shalini Singh** E Demidova, N. Resnina, S. Belyaev, I. A. Palani, C.P. Paul , K.G. Prasanth Published -Journal of 3d Printing and Additive Manufacturing https://doi.org/10.1089/3dp.2021.0324 (Impact Factor -5.4)
- Microstructure and mechanical properties of NiTi-SS Bimetallic Structures Built using Wire Arc Additive Manufacturing- **Shalini Singh**, Jinoop A, I.A. Palani, C.P. Paul, K.G.Prasanth- Material letters https://doi.org/10.1016/j.matlet.2021.130499 (Impact Factor- 3.57)
- Effect of Interlayer Delay on the Microstructure and Mechanical Properties of Wire Arc Additive Manufactured Wall Structures- **Shalini Singh**, Arackal Narayanan Jinoop ,Gorlea Thrinadh Ananthvenkata Tarun Kumar,Iyamperumal Anand Palani ,Christ Prakash Paul andK.G. Prashanth, Mataerials, https://doi.org/10.3390/ma14154187 (Impact factor- 3.61).
- Laser Hybrid Wire Arc Additive Manufacturing for fabricating thin sections of Stainless Steel"-**Shalini Singh**, G.T.A.V. Tarun Kumar, Ashish Shukla, I.A. Palani, N. Resnina , C.P. Paul-Transactions of the Indian National Academy of Engineering https://doi.org/10.1007/s41403-021-00258-3.
- NiTi-Cu bimetallic structure fabrication through Wire Arc Additive Manufacturing **Shalini Singh,** Elena Demidova, Natalia Resnina, Sergey Belyaev, I.A. Palani, C.P. Paul ¯Under Review- The international Journal of Advanced Manufacturing (Impact Factor -3.2).
- Influence of the Interlayer Temperature on Structure and Properties of CMT Wire Arc Additive Manufactured Ni-Ti Structures- **Shalini Singh**,, Shirin Dehgahi, A.J. Qureshi, I.A. Palani , C.P. Paul – Under Review –Journal of Alloys and Compounds .
- Development of Cu-based shape memory alloy through selective laser melting from elemental powder mixture: Processing and characterization- **Shalini Singh**, I.A. Palni; Zhi Wang; Shirin Dehgahi; Ahmed Qureshi; A.N. Jinoop; C.P. Paul-Under Revision-Journal of Alloys and Compounds.

Conference

- Investigation on actuation characteristics of tailor-made NiTi shape memory alloy structures fabricated through wire arc additive manufacturing (WAAM) technique. Mani Prabu, S. S., Manikandan, M., Thakur, V. S., Sahu, A., & **Singh, S.** (2019). Investigation on actuation characteristics of tailor-made NiTi shape memory alloy structures fabricated through wire arc additive manufacturing (WAAM) technique.
- Theoretical Investigations on Influence of Inter-pass Cooling Conditions on Wire Arc Additive Manufactured Parts- Gorlea Thrinadh Ananthvenkata Tarun Kumar, **Shalini Singh**, Ashish Shukla, N. Resnina, S. Belyaev, I. A. Palani & C. P. Paul- ICAMMM 2021,Kancheepuram, TamilNadu, India.

Book Chapter

Introduction to Lasers and Processing's of Materials. Shukla, A. K., Kulkarni, A., **Singh, S.,** Jayachandran, S., Sahu, A., & Palani, I. A. (2022). In Advanced Engineering of Materials through Lasers (pp. 1-31). Springer, Cham.

Laser polishing of wire arc additive manufactured SS316L.Thakur, V. S., Manikandan, M., **Singh, S**., Mishra, S., Kaithwas, A., Mani Prabu, S. S., & Palani, I. A. (2020). In Advances in Additive Manufacturing and Joining (pp. 127-135). Springer, Singapore.

TABLE OF CONTENTS

LIST OF FIGURES

LIST OF TABLES

ABBREVIATIONS

Abbreviation		Description
1	SMA	Shape Memory Alloys
2	OWSME	One Way Shape Memory Effect
3	TWSME	Two Way Shape Memory Effect
4	SME	Shape Memory Effect
5	As	Austenite start temperature
6	A_f	Austenite finish temperature
7	Ms	Martensite start temperature
8	Mf	Martensite finish temperature
9	SEM	Scanning Electron Microscope
10	EDS	Energy Dispersive Spectroscopy
11	DSC	Differential Scanning Calorimetry
12	DAQ	Data Acquistion System
13	MEMS	Micro Elecro Mechanical Systems
15	WAAM	Wire Arc Additive Manufacturing
16	SLM	Selective Laser Melting

NOMENCLATURE

$a_{f,r}$- Ellipsoid x semi-axis (front or rear)

b -Ellipsoid y semi-axis

c -Ellipsoid z semi-axis (front)

q_f – Heat flux in the front ellipsoid

q_r – Heat flux in the rear ellipsoid

ν – Velocity

f_f – Heat fraction coefficient in the front ellipsoid

f_r – Heat fraction coefficient in the rear ellipsoid

η – Heat transfer efficiency

Q – Heat input

I – Applied Current and

V - Voltage

$f_{f,r}$ -Ellipsoid distribution factor (front and rear)

q_w= filler material

q_b- base material

V_{el} = Volume of the element (depends on mesh size)

λ_{act}= active material property

λ_{quie}= inactive material property

γ = activation variable

T= current simulation time;

ε = surface emissivity

ρ= density

k=material conductivity

C_p = specific heat capacity

A=area

∇T = temperature gradient

h = heat transfer coefficient

σ= Stefan’s constant

$T_{room=}$= room temperature

Dedicated to my Guides, God

Chapter 1

Introduction

1.1 Shape Memory Alloys

Shape memory alloys (SMAs) or "smart alloys" are a unique class of smart materials that can change their form (shape or size), and can return back to their original form with applied heat, stress, or magnetic field. They have the ability to produce very high actuation strain, stress, and work output due to reversible martensitic phase transformations [1]. Shape memory alloys are compact, robust, lightweight, frictionless, quiet, biocompatible, environmentally friendly, and possess superior properties in actuation, vibration damping, and sensing. Shape memory alloy was first discovered by a Swedish physicist Arne Ölander in 1932 [2]. Two researchers of the US Naval ordnance laboratory, William Buehler, and Frederick Wang discovered the shape memory effect (SME) in a nickel–titanium (NiTi) alloy in 1962 [2]. In 1970s, shape memory alloys were started using in the commercial products and devices. Since then, there have been tremendous developments in the field. Due to the aforementioned unique properties, the demand for SMAs has been increasing for the applications, such as micro-electromechanical systems (MEMS); robotics; consumer and industrial products; automotive, aerospace, and biomedical fields. Shape memory alloys are used in actuators for automotive and aerospace applications. Along with actuators, structural connectors, vibration dampers, manipulators, and some pathfinder applications in aerospace are also deploying shape memory alloys. SMAs have also been successfully used in micro-and macro-actuators for robotic fingers and hand, and artificial muscles for robotics applications [3]. SMA based actuators have been used in controlling flying robots. NiTi shape memory alloy is a prime candidate material for biomedical applications and used to make surgical tools, dental implants, bone implants, stents, and other medical equipment. While manufacturing parts/components of SMAs to be used in the field stated above, these materials have to undergo extensive fabrication and processing operations. Practically, SMAs can exist in two different phases with three different crystal structures, and six possible transformations [4]. While heating, the SMA begins to transform from martensite into austenite phase. The two temperature points during this transformation are—"A_s-austenite-start-temperature", where transformation starts and 'A_f-austenite-finish-temperature', where

transformation ends. Once an SMA is heated beyond A_s it begins to contract and transform into the austenite structure, i.e., to recover into its original form. This transformation is possible even under high applied loads, and therefore, results in high actuation energy densities [5]. During the cooling process, the transformation starts to revert to the martensite at martensite-start-temperature (*M*s) and is complete when it reaches the martensite finish-temperature (M_f). The highest temperature at which martensite can no longer be stress induced is called M_d, and above this temperature, the SMA is permanently deformed like any ordinary metallic material [5]. Three possible shape change effects in SMAs are given in the subsequent sections.

1.1.1 Pseudoelasticity

Due to pseudoelasticity (also called superelasticity), the SMA reverts to its original shape when the applied deformation stress is removed [6]. It is done by the subsequent recovery of the deformation strain when the stress is removed. Fig.1.1 illustrates the pseudoelasticity mechanism where the material from point "A" is stressed at a constant temperature while being in a stable austenite phase. The resulting deformation is elastic until a certain point "*B"*, where the material reaches the state that the martensitic transformation begins. From this point on, the transformation that takes place is accomplished under a constant stress, while the strain continues to increase, until a maximum strain level (point C). The maximum strain level varies according to the material. The curved section between points (B) and (C) is termed the stress "plateau." At this point, the phase transformation from austenite to martensite is completed and the curve that describes the behavior of the material is different. This new behavior usually presents a small temperature hysteresis ($A_f - M_s$), whereas the "parent" martensite interfaces present some mobility. Further stressing the material from point (C) will only lead to elastic deformations of the detwinned martensite. Finally, after the stress is removed, the material begins to return to its stable austenite phase, until it fully transforms this phase (point D), thus the cycle can be repeated.

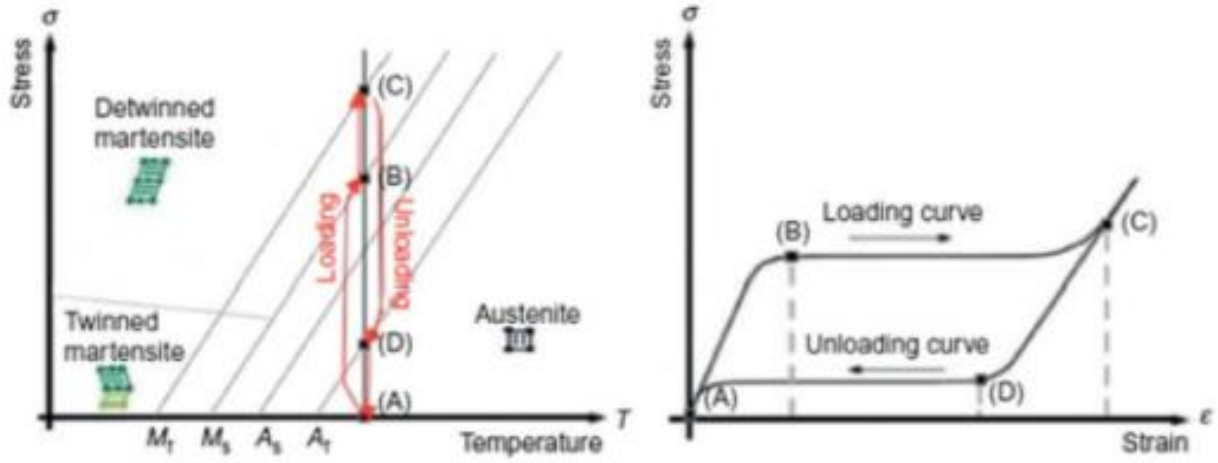

Fig.1.1 Stress and temperature and stress and strain [6-7]

1.1.2 Shape Memory Effect

As SMA materials are heated from low temperature phase to high temperature phase, shape memory effect (SME) occurs. It explains the effect of restoring the original shape of a plastically deformed material by heating it above transformation temperature. It involves the transition from one form of crystal structure to another. This phenomenon of changing from one crystalline phase to the other crystalline phase is known as "thermo-elastic martensitic transformation". At temperatures below the transformation temperature, SMAs are in martensite phase. In this condition, the SMA material is soft and can be deformed quite easily by detwinning. The microstructure is characterized by self-accommodating twins. Heating above the transformation temperature recovers the original shape and converts the material to its high strength austenite phase [7]. The transformation from the austenite to martensite and the reverse transformation from the martensite to austenite do not take place at the same temperature.

1.1.2.1 One-way Shape Memory Effect:

At low temperature, a SMA material can be plastically deformed. This deformation involves the movement of highly mobile boundaries (twin boundaries, martensite / martensite interfaces). Upon heating, SMA material reaches Austenite phase with the initial orientation and so the

specimen reverts to its original shape. While cooling, no additional shape change takes place; this effect is called “oneway shape memory effect”. The one-way effect can be repeatedly induced by deforming SMA in the martensitic state. Initially, in a SMA material displaying one-way SME, there is no movement on heating. The shape change starts at As temperature and get completed in a small temperature range (e.g. 10 to 30 K). The As temperature of NiTi SMAs can be significantly tuned by suitable selection of the chemical composition of the alloy and dopants.

1.1.2.2 Two-way Shape Memory Effect:

SMAs with a two-way shape memory effect (TWSME), "remember" both a high temperature shape (austenite) and a low temperature shape (martensite). Though, TWSMAs can switch from their low temperature shape to their high temperature shape, their recoverable strain is usually about half of their corresponding one-way SMAs. To produce a two-way effect, it is necessary to induce a special mechanical/thermal treatment in a SMA. One method to produce a two-way effect is based on a severe deformation in the martensitic state. In addition to this, there are still some other methods to produce a TWSME. They are (1) SME training, (2) stress-induced martensite training, (3) combined training, (4) forces of inactive surface layers and etc [8]. During heating, the specimen will move towards its original shape and the high temperature shape gets formed. On cooling again, the pre-existing martensite plates will accommodate the stress field of the induced dislocation structure and preferred martensite variants forms, which give rise to the formation of low temperature shape. Thus, by temperature cycling one gets the two-way effect. This method of the production of the two-way effect can be used for training in the NiTi alloys, since it displays high ductility.

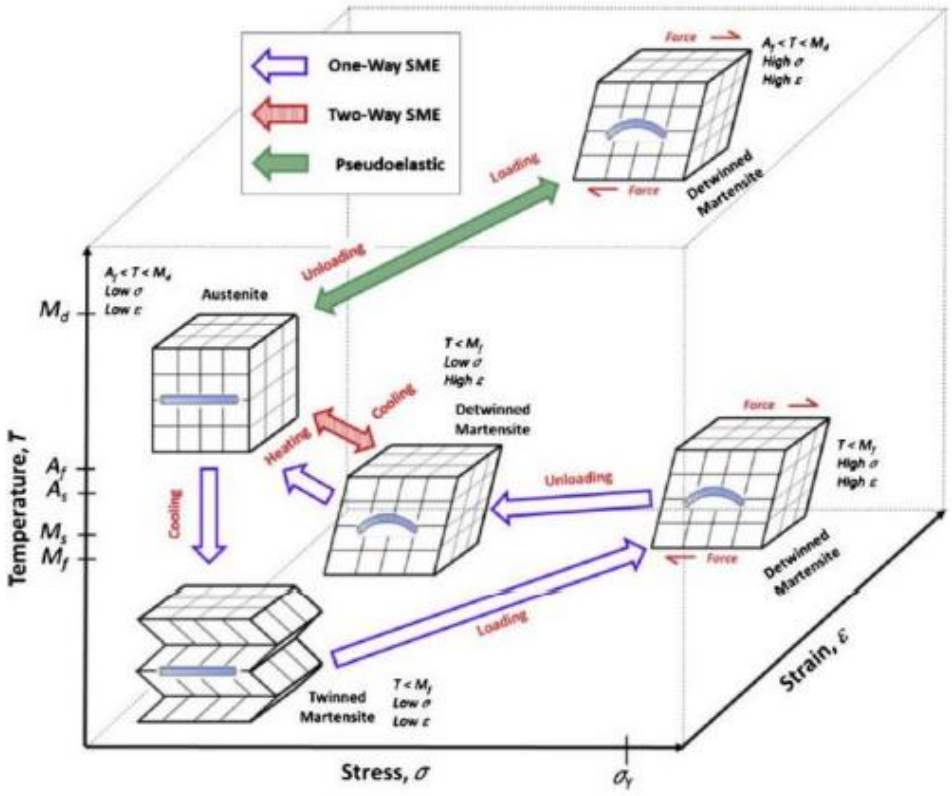

Fig.1.2 A description of shape memory phenomena – one way shape memory effect, two way shape memory effect and pseudoelasticity [9]

Fig. 1.2 illustrates 3D illustrations of different shape memory phenomena, including stress and temperature, stress and strain (one-way shape memory effect, two-way shape memory effect, and pseudoelasticity).The purple colored arrows highlights the transformation from austenite to martensite on cooling (forward reaction), the deformation of the martensite and the transformation of deformed martensite back to the austenite phase(reverse reaction). In thermoelastic transformations, the transformation from the parent phase to the martensite phase and the reverse transformation temperature are represented by M_s, M_f, A_s and A_f temperatures respectively. Ms (martensite start) signifies the beginning of the martensite formation and Mf (martensite finish) signifies complete formation of martensite. The As (Austenite start) is the beginning of the reverse reaction that is the formation of austenite and A_f (Austenite finish) marks the end of the reverse reaction that is complete formation of austenite [9].

1.1.3 Types of Shape Memory Alloys

There exists a wide range of metals, polymers, ceramics, and other materials that show the shape memory effects. Shape memory alloys (metals) are available in a wide range, as given below [9]:

• Iron-based alloy Fe–Mn–Si;

• Copper-based SMAs such as Cu–Zn–Al; Cu–Al–Ni, Cu–Al–Ni–Mn, and Cu–Sn;

• Nickel–Titanium based alloys such as NiTi, NiTiCu, NiTiPd, NiTiFe, NiTiNb, NiFeGa, and NiTiCo;

• Kovar (29% Ni, 17% Co, 0.3% Si, 0.1% C and Fe balance);

• Hi-temperature shape memory alloys such as TiNiPd, TiNiPt, NiTiHf, NiTiZr,ZrRh, ZrCu, ZrCuNiCo, ZrCuNiCoTi, TiMo, TiNb, TiTa, TiAu, UNb, TaRu,
NbRu, and FeMnSi;

• Magnetic shape memory alloys, namely, NiMnGa, FePd, NiMnAl, FePt, Dy, Tb, LaSrCuO, ReCu, NiMnIn, and CoNiGa.

1.1.4Application of shape memory alloys

1.1.4.1Tool clamping device

Due to increasing demands in technology, it is required to increase efficiency and throughput of the industries. This requires models to relate online monitored parameters like, vibration, temperature, cutting force, vibration with tool degradation, Shape Memory Alloy (SMA) damping and product quality. The relationships can then be used as an input for dynamic process control and maintenance planning in manufacturing industries. The SMA structures proposed here dampen out such vibrations and prevent overheating, thereby increase life of the tool and quality of the product output. This SMA ring acts as passive damper that takes up the heat and actuates itself thereby reduces vibrations and provide dampening effect.

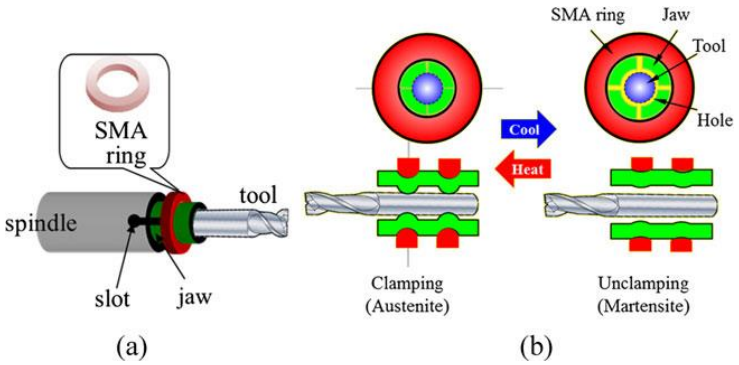

Fig.1.3 (a) Configuration and (b) operating principle of SMA tool holder [10]

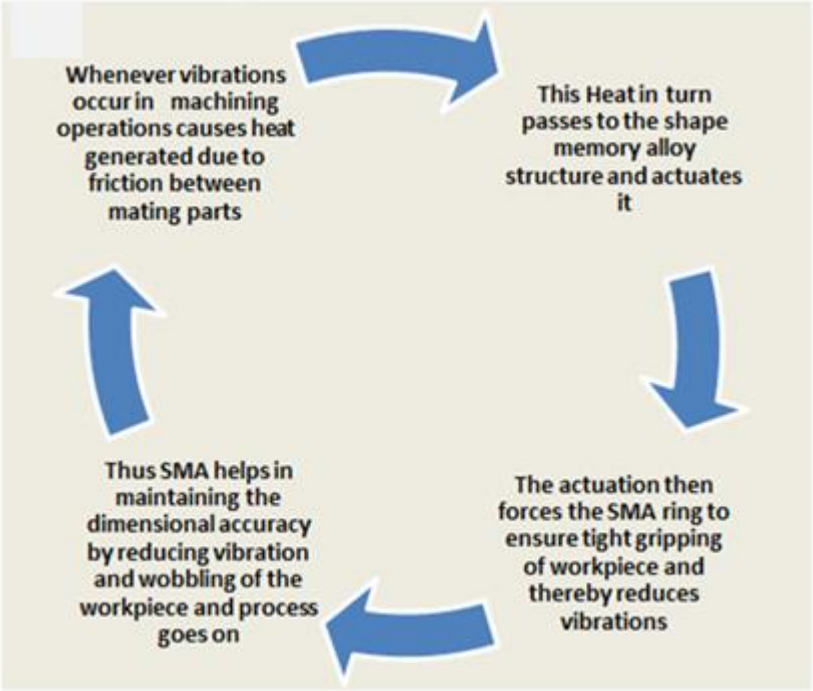

Fig. 1.4 Process Chart showing the mechanism of the proposed Idea

1.1.4.2 Bio-Medical Application

The application of SMA in the bio-medical field can be categorized into three. 1) Orthodontic field 2) Orthopedic field 3) Vascular field 4) Neurosurgical field. It was introduced in the biomedical field in 1975, by Dr. Andreason of Lowa University. The Usage of Ni-Ti Wires in the buccal cavity at the austenitic phase has been employed for recent years in dental diagnosis with multi-brackets. These NiTi wires generate an all-round force for the brackets for good dental movement. SMAs wire also found application in Palatal arches. Table 1 illustrates the historical developments of alloys in the bio-medical field, Figure 1[11].

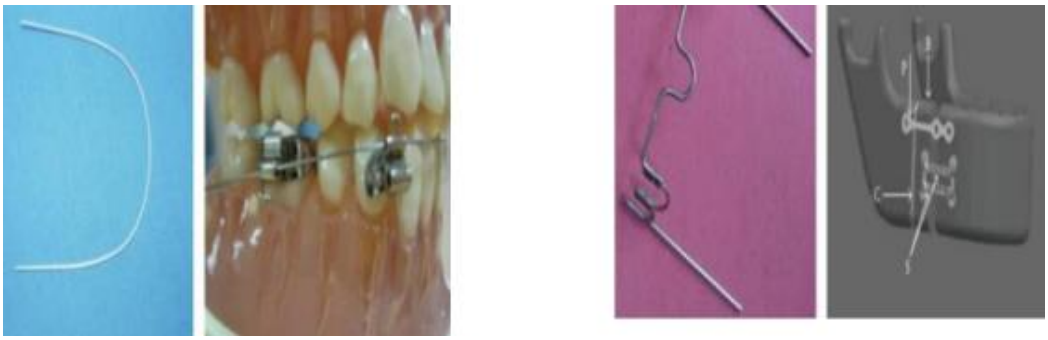

Fig. 1.5 SMA orthodontic wires and distractors [11]

Pseudo elastic behavior of SMA in Orthodontic field, for orthodontic distractors [12]. The Pseudo elastic effect of the Ni-Ti alloy is also used as a nail in fractured elongated bones. In both Orthodontic and Orthopaedic treatments, physiotherapy of partially atrophied muscles is exploited through the properties of SMA materials [13].

Fig 1.6. (a) SMA plate for mandible fracture (b) Spinal vertebrae spacer. [11]

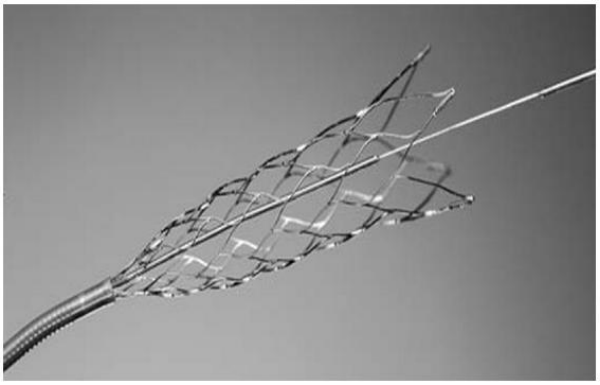

Fig. 1.7 Ni-Ti Neurosurgical stent [16]

Simpon filter was the first ever used vascular instrument in SMA application. NiTi alloys are also used as a neurosurgical stents. Stents are nets made up of metallic which opens a stenotic vessel that enables the flow of blood to peripheral tissues. Recently stenotic and cardiac valves were made of this alloy. Coils, stents, and micro guidewires are also the other applications of this alloy, Figure (14) [14]. The stents treatments aim to recover the flow of blood flow through the

narrowed lumen. Because of the rigidity of SMA coils and stents, they are preferred over the conventional or classical type one. Micro guide waves are used for positioning the stent [11].

1.1.4.3 Aerospace application

This industry is looking for improved materials and solutions for its applications. Wind morphing is a practical solution that can be met in different conditions [15]. Researchers have brought to light both the shape memory and pseudoelastic effects in solving industrial problems of aerospace. Implementation of this technology in fixed-wing aircraft, rotorcraft, and spacecraft has gained importance. It describes the aerospace application of alloys and the challenges faced by the designer of such a system [16]. SMA coupling of hydraulic lines has impressive application in fighter jets, people gathered their great interest in aerospace application. Some of the applications are sealers, actuators, vibration-dampers, etc, Figure (6-7).

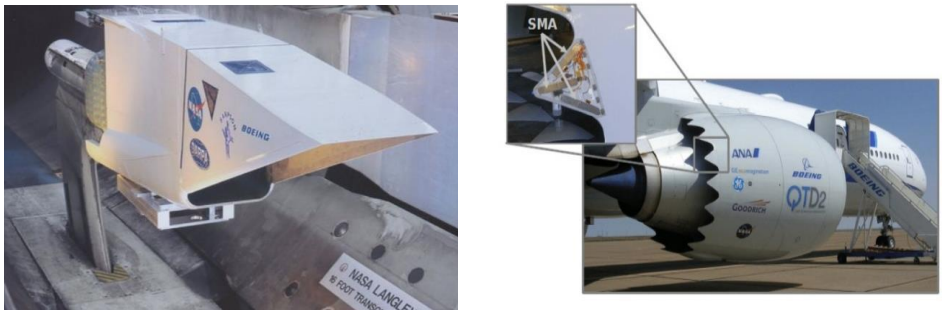

Fig. 1.8 (a) SMA airplane wing [16], (b) Boeing variable chevron [17].

A program was used to develop and demonstrate the shape memory alloys to optimize the performance of lifting bodies. An SMA Tube was used to initiate wing expansion by twisting. Though the alloy was able to deliver the required actuation the tube, in particular, was not able to deliver at full effort span wing. This work was performed by the Air Force Research Lab (AFRL). The Smart and Aircraft and Marine Propulsion System Demonstration (SAMPSON) program introduced the use of such materials in modifying the geometry of inlet conditions of different propulsion systems of aircraft. Validation was done on a full-scale F-15 inlet. First wind tunnels was developed at NASA in which one SMA is set in opposition to another [11]. This effect can be used to rotate the inlet cowl to change its cross-section of area. SMA bundles were loaded in two different directions, heating one bundle resulting in deformation which is used to recover its original form. After the bundle in heating condition was cooled, the earlier detwinned bundle was again heated, and actuation occurred in the opposite direction [17-18]. The Adaptive

Nozzle made of SMA is a most developed product which is used to aid noise reduction in gas turbine engines. In aircraft, SMA thin plates are attached to Ti-6Al-4V alloy. At a high power setting, the hot SMA will actuate and employ the serration in the air flowing of engines. At low power settings, the engine allows Ti-component which is passive elastic is used to reset the serration of SMA to returned configuration [19].

1.2. Fabrication of Shape Memory Alloy (Conventional Processes)

1.2.1 Manufacturing challenges of NiTi and NiTi based bimetallic strucure

NiTi (Nickel-Titanium) is a shape memory alloy that exhibits unique properties such as shape memory effect, superelasticity, and high damping capacity, making it a promising material for various applications in industries ranging from biomedical to aerospace. However, the manufacturing of NiTi-based structures is challenging due to its high reactivity with oxygen, strong hysteresis, and limited ductility, which limits its deformation capacity.

There is few manufacturing challenge which is given below

- Controlling composition and microstructure to achieve desired properties Achieving uniformity and consistency in microstructure and properties across large production runs
- Optimizing processing parameters, such as heat treatment and deformation conditions, to achieve desired properties
- Overcoming issues with machining and joining due to high hardness and shape memory effects
- Reducing surface defects, such as cracks and pores, that can lead to premature failure
- Controlling the shape memory effect during processing and fabrication
- Managing the complex deformation behavior of NiTi, including stress-induced martensite formation and twinning
- Achieving a balance between shape memory effect and superelasticity

One of the significant challenges in NiTi manufacturing is its strong hysteresis, which causes a reduction in the life cycle of NiTi products. Researchers have proposed several methods to overcome this challenge, such as joining NiTi with other materials, including Stainless Steel, Titanium, and Copper, to create bimetallic structures. The aim is to improve the mechanical

properties of NiTi by inducing brittle intermetallic compounds at the interface of the bimetallic structure. A study by S. Iqbal et al. investigated the influence of Wire Arc Additive Manufacturing (WAAM) on the grain structure, chemical composition, phase composition, and phase transitions in bimetallic shape memory composites containing TiNi shape memory alloy as an active layer and other materials (Stainless Steel, Titanium, and Copper) as a passive layer. The results showed that the mechanical properties of the bimetallic structure were enhanced due to the formation of intermetallic compounds at the interface.

Another challenge in NiTi manufacturing is its limited ductility, which makes it difficult to deform NiTi structures. Researchers have proposed several methods to improve the deformation capacity of NiTi, such as incorporating porosity in the structure. Porous NiTi structures exhibit enhanced mechanical properties and can be used as implants and vibration dampers for civil structures, machinery, and automobiles. However, the fabrication of porous NiTi structures is challenging, and there is limited literature available on the subject. A study by A. Gupta et al. investigated the fabrication of NiTi porous structures through Powder Bed Fusion (PBF) Additive Manufacturing (AM). The study revealed that the pore morphology, size, and distribution could be controlled by varying the process parameters such as laser power, scan speed, and hatch spacing.

In addition to the above challenges, NiTi manufacturing is also challenging due to its high reactivity with oxygen, which causes the formation of oxide layers on the surface, leading to poor adhesion and reduced mechanical properties. Researchers have proposed several methods to mitigate this challenge, such as the use of protective atmospheres during manufacturing. A study by Y. Li et al. investigated the effect of protective atmospheres on the microstructure, mechanical properties, and corrosion behavior of NiTi fabricated through Selective Laser Melting (SLM) AM. The study revealed that the use of an argon atmosphere during LPBF resulted in a significant reduction in the oxide layer thickness and improved the mechanical properties of the NiTi structure.

In conclusion, NiTi manufacturing is challenging due to its strong hysteresis, limited ductility, and high reactivity with oxygen. Researchers have proposed several methods to overcome these

challenges, such as incorporating porosity in the structure, joining NiTi with other materials, and using protective atmospheres during manufacturing. However, there is still a need for further research to overcome the challenges in NiTi manufacturing and to explore the full potential of this promising material.

Table 1 Manufacturing of NiTi

Manufacturing Methods	**Classifications**	**Quality of Product (in terms of surface finish and dimensional accuracy)**	**Defects**	**Post-processing required**
Casting	VAR	Average	Average (C and O2, segregation)	Machining
VIM	Average	Average (C and O2, segregation)	Machining	Low
Powder metallurgy	Conventional sintering	Low	High (mixing and sintering defects)	Surface treatment
SHS	High	Average (microstructure control)	Surface treatment	High
HIP	High	Average (decrease internal micro-porosity)	Surface treatment	High
MIM	High	Average (larger parts difficult to fill in furnace)	Surface treatment	High
SPS	High	High (complex parts cannot be fabricated)	Surface treatment	High
Additive manufacturing	SLM	Very high	Low/minimum	Not required
SLS	Very high	Low/minimum	De-burring	Very high
LENS	Low	Low/minimum	De-burring	Very high
EBM	High	Low/minimum	Not required	Very high

1.2.2 Machining of NiTi

Due of its distinct attributes and resistance to deformation, SMA is challenging to machine, and the process results in significant tool wear. The preferred cutting techniques for this material are consequently abrasive ones like grinding and abrasive saws. The cutting speed and feed rate, which should be selected as being high enough, have a considerable impact on the machinability of NiTi. Due of the high ductility and unusual stress-strain behavior, poor chip breaking and the development of burrs are additional issue. Tool wear is still an issue when machining these alloys despite the improvement of the machining variables. Although it increases microhardness in the subsurface zones of the part, drilling NiTi components at high cutting feeds and speeds helps increase tool life and improve work piece quality [20].

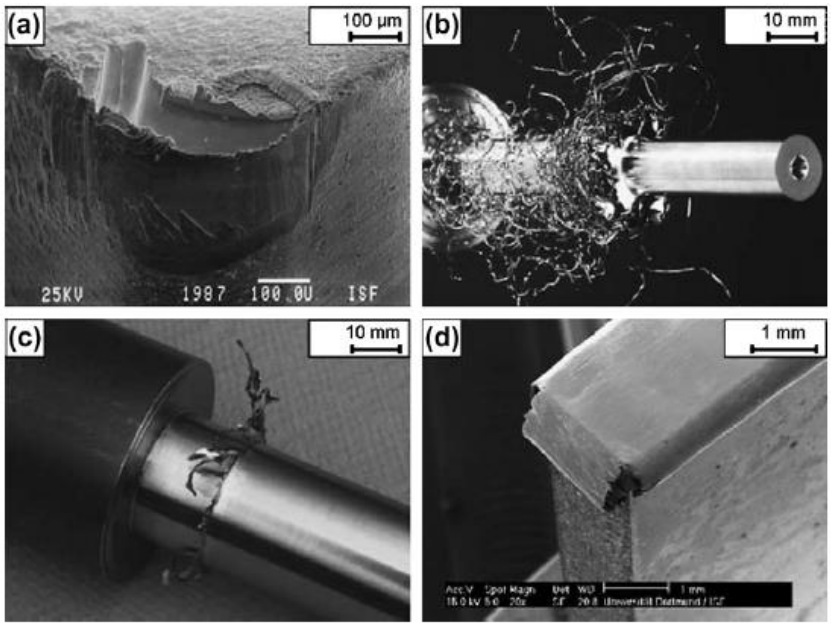

Fig. 1.9 Major drawbacks in machining NiTi shape memory alloy: (a) high tool wear, (b) undesirable chip formation , (c) formation of burrs after turning (d) and grinding.[adapted from : reference [20]]

1.2.3 Casting and Powder Metallurgy

One of the popular traditional methods for generating NiTi is casting process. This method involves high-temperature melting processes that raise the impurity content (for example, carbon

and oxygen) and, as a result, lead to the creation of Ti-rich phases like TiC and Ti4Ni2OX. These secondary phases' development results in a degradation of NiTi's functional characteristics. The difficulty of these super-ductile alloys' machining techniques, which results in increased tool wear, is another issue with this technology since machining is utilized to create the final shapes from these alloys [21].

Another traditional method for creating near-net-shape devices is powder metallurgy (PM). Prior to PM processing, powder preparation is necessary. This method's high impurity pick-up, which is caused by the powder particles' large surface area, is one of its main drawbacks. Additionally, these methods are constrained in their ability to control the size and shape of porosity when required as well as the intricacy of the produced pieces. [22].

1.2.4 Need for additive manufacturing for shape memory alloy fabrication

Due to SMA's low workability and high tool wear [23] during fabrication, it is challenging to mold into complicated geometries using traditional techniques. Similarly, fabrication of polycrystalline Cu-based SMA structures is challenging due to the material's fragility [24–28]. These problems are easily solved by using additive manufacturing (AM), which eliminates the requirement for tooling and enables the manufacture of SMA parts with complicated shapes straight from CAD models. Numerous review publications have focused on advancements in the field of AM of SMAs. Elahinia et al. [21–22] evaluated the AM techniques utilized to create NiTi components and outlined the various variables influencing the behavior of the samples they obtained. The original powder properties, AM process parameters, and heat treatment were taken into consideration. Similar to this, Wang et al. [24] looked at how additively manufactured NiTi (AM-NiTi) samples' functional and mechanical characteristics were affected by selective laser melting (SLM) settings. In addition to generating NiTi SMAs, AM was successfully used to create Cu-based [29], CoNi [30], and Ni-Mn-Ga SMAs [31]. In contrast to NiTi, however, there isn't nearly as much research being done in this field. Reviews on this subject need to be updated frequently due to the rapid growth of additive manufacturing technology and the significant amount of scholarly output devoted to additively made SMAs. Additionally, despite the growing significance of other SMA compositions and the availability of literature addressing AM of non-NiTi SMAs, the majority of evaluations that are now available appear to concentrate solely on AM-NiTi. Due to its ability to get around many of the difficulties that come with using

traditional techniques, additive manufacturing (AM) has attracted a lot of attention over the last two decades for processing NiTi.

Current AM solutions are broadly classified in powder bed, flow-based, and binder jetting systems.

1.2.4.1. Powder bed systems

Powder metal beds are used in powder bed fusion (PBF) or powder bed systems (PBS) [32] to create products with predetermined 3D forms. Raking metal powder layers across a work surface, typically with a thickness of 20 to 100 μm [33, 34-36], produces the powder bed. Designated places on the powder's surface are heated and melted by an energy source, typically an electron or a laser beam [35], which bonds together pieces of the powder layer in accordance with the desired CAD design. Following solidification, a piston compacts the work area to provide room for the subsequent powder layer to be deposited. The procedure, shown in Fig. 1.10, is repeated until the entire 3D shape is constructed.

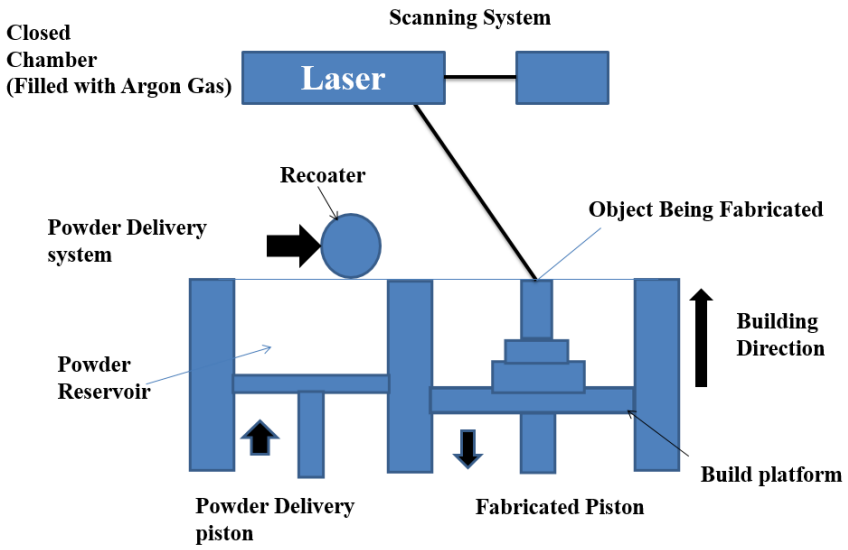

Fig. 1.10 Powder bed system

The most commonly used techniques for melting the metal powder are Electron Beam Melting (EBM) and Laser Beam Melting (LBM). The difference between the two techniques is the type

of energy source used: EBM uses electrons whereas LBM uses photons, as illustrated in Fig. 1.11.

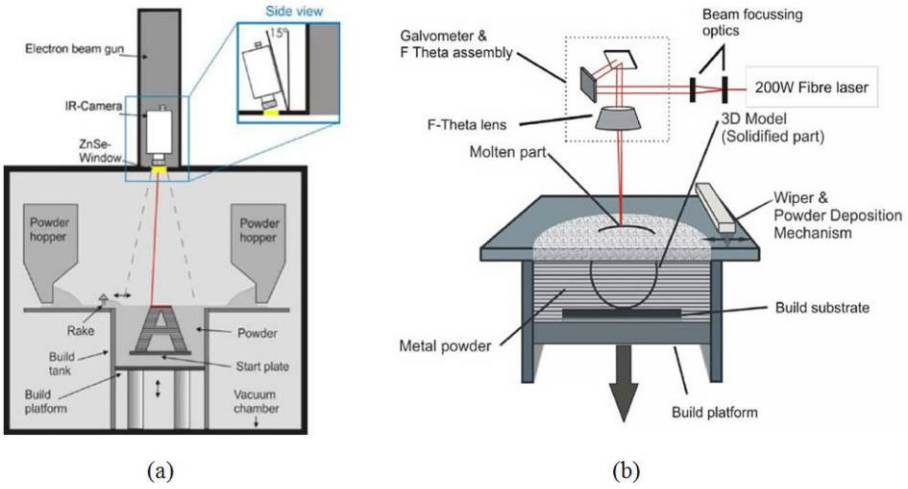

Fig.1.11 Schematic representation of (a) EBM and (b) LBM systems [15]

The procedure is carried out in a sealed space that is either vacuum-filled or filled with an inert gas (such as nitrogen, argon, etc.) to prevent oxidation. The mechanical qualities of the produced item are protected from contamination by non-metallic elements (impurities) such oxygen and carbon [37]. To reduce the stress brought on by heating, the chamber is preheated to a predetermined temperature depending on the material. With different energy source types, the preheating temperature of the chamber varies, ranging from about 100 °C for laser processes to 700 °C–1000 °C for electron beam processes [38]. EBM often produces parts with higher surface roughness than LBM, necessitating additional post-processing. In comparison to PBS based on lasers, the technique also permits quicker construction rates. Despite being restricted to a relatively small build volume, powder bed techniques can typically create complex parts with high resolution features while maintaining dimensional control [38–40].

1.2.4.2. Flow-based systems

One or more nozzles are used in flow-based AM systems (FBS) to deliver and fuse metal into the build surface in the form of powder or wire [38,40]. An inert carrier gas or gravity feed is used to inject the material, with a shielding gas being used to prevent oxidation in the molten regions.

Then, for each material layer, a laser fuses particular areas in accordance with a predetermined CAD model, as shown in Fig. 1.12.

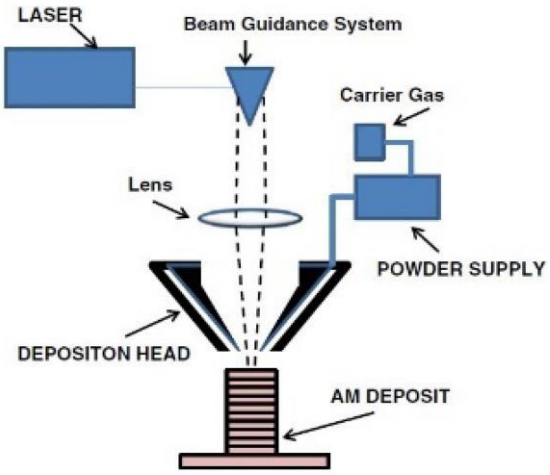

Fig. 1.12 Schematic representation of the DED process. The material is deposited through the deposition head and is simultaneously targeted by the laser beam [14].

Layer by layer, the process is continued until the 3D model is created. Direct Metal Deposition (DMD), wire and arc additive manufacturing (WAAM), and Laser Engineered Net Shaping (LENS) all make use of FBS technology [41]. Flow-based systems are not limited to a specific build volume, unlike PBS. They are therefore frequently employed to deposit additional features on rather big sections [41]. PBS's relative lack of precision, which raises the need for more postprocessing, is a drawback, too.

1.2.4.3 Binder jetting

A printer head resembling an inkjet is used in the additive manufacturing (AM) process known as binder jetting to release drops of binder material (glue) on a power bed in a targeted manner. Based on the CAD model of the desired product, the binder distribution is made. With the major distinction of using a binder rather than a heat source to combine powder particles, the process is somewhat similar to SLM in design and operation. With BJ technology, complexly crafted items consisting of metal, polymer, or ceramics may be built up quickly. Figure 1.13 is a schematic representation of a BJ printer.

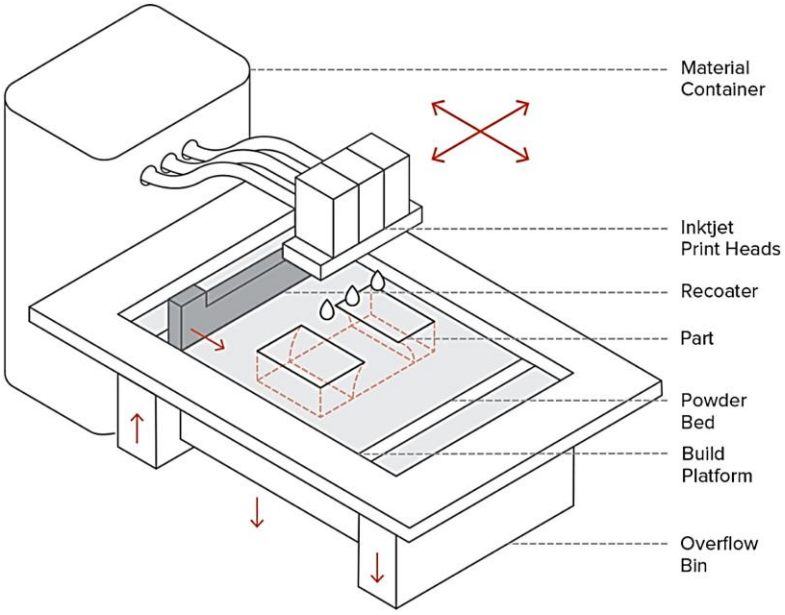

Fig. 1.13. Schematic representation of a binder jetting 3D printer [100]

Since no heat is generated during the fabrication process, problems caused by too much heat, such as warping and modifications to the material's microstructure and composition, are avoided. This makes it possible to produce huge quantities of goods. Unlike other AM techniques, all unused powder can be recycled. However, to increase their cohesiveness and mechanical performance, BJ printed items often need post processing through curing, sintering, extrusion, etc. The quality of the printed result also depends on the properties of the powder utilized as well as factors like the thickness of the powder layer, the saturation of the binder, the speed of the deposition, the printing techniques, and the post-processing.

In the following sections, the microstructure, printability, phase transformation temperatures and thermomechanical properties of SMAs fabricated using different AM technologies are discussed.

1.2.4.4. Wire arc additive manufacturing

An alternative direct energy deposition technique is wire arc additive manufacturing (WAAM). The metal is melted and the product is constructed layer by layer using an electric arc rather than a laser or electron beam [42]. WAAM's high deposition rates, which are typically between 1 and 10 kg/h, and resolutions of almost 1 mm enable it to produce intricate near-net-shaped structures in a comparatively short amount of time. The potential of WAAM therefore sits between slower

laser-based systems with good accuracy and higher deposition rate electron and plasma technologies with reduced accuracy [43].

The WAAM technique's schematic is shown in Fig. 1.14. The WAAM technique's core tools are a 3D axis manipulator and an arc welding setup. The method is currently not entirely automated because manual involvement is needed at various production stages. To achieve geometrical criteria, the printed object's surface polish needs to be further machined. But WAAM has been used to print steel [44], aluminum [45], and titanium [46] things with success. With regard to the manufacturing of SMAs employing the WAAM technique, very few works [47] have been published in the literature, which undoubtedly open the door for further investigation.

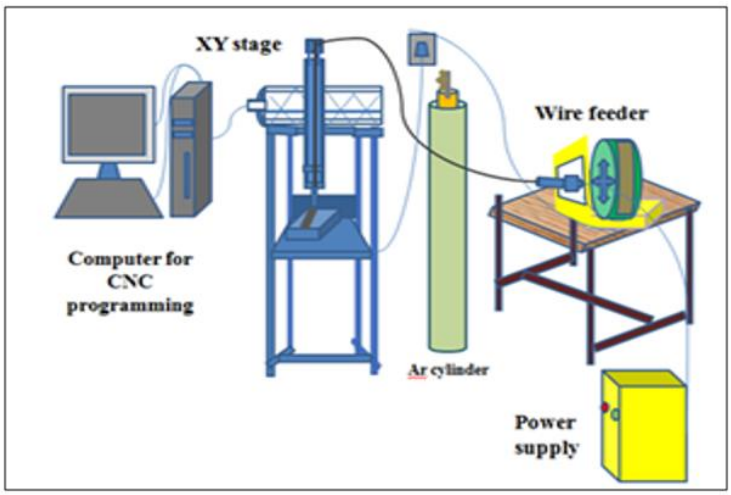

Fig.1.14 Schematic illustration of the wire and arc additive manufacturing (WAAM) process

1.3 Literature Survey

1.3.1 NiTi fabrication through WAAM

The significant attractions of WAAM are low cost, high material efficiency, and high deposition rate [47]. Despite the fact that this process is widely used to produce steel, Cu-Al, Fe-Al, Ti-based, and other alloys, it was not used to deposit NiTi form memory alloy until 2018[48-54]. In 2018, Wang et al. used a GTAW-based WAAM process to melt pure Ti and Ni wires and deposit NiTi alloy with 53.5 percent Ni on a Ti substrate to develop Ni-rich NiTi alloy. The sample structure, which was rather heterogeneous, included the NiTi matrix as well as Ni-rich

precipitates like Ni_4Ti_3 and Ni_3Ti. The presence of very weak heat release and heat absorption peaks was revealed by differential scanning calorimetry analysis of martensitic transitions in different sections of the Ni-rich NiTi sample [55-56].

Zheng et al. used a GTAW-based WAAM method to fabricate a 5-layered NiTi sample on a NiTi substrate using Ni - 49.5 at. percent Ti wire as the feedstock to resolve this problem. There were no defined correlations between the structure, the martensitic transformation, and the mechanical behavior in different layers, despite the fact that the martensitic transformation and superelasticity were investigated in this research [57]. However, understanding how the layer structure influences the functional behavior of NiTi alloy components produced by WAAM requires such correlations. Despite the fact that the accuracy of the as-built parts may be lower than that of laser or electron beam-based MAM systems, WAAM is currently being adopted by both academia and industry due to the technique's inherent advantages. An electric arc is used as a heat source in this process to melt the feed material into wire form [58]. The required geometry can be obtained with the help of an XY stage or CNC workstation, and Z shift of the welding torch will aid in the deposition of multiple layers one over the other. Wall structures can be considered as a fundamental building block to build complex-shaped engineering components using WAAM. In addition, wall structures are widely used to build engineering components in the aerospace, power sector etc., where light-weighting is required. They are also significant for the fabrication of 3D parts, like - porous structures, cooling channels for heat exchangers, fins, and landing gear ribs [59]. Several researchers are working in developing wall structures using WAAM and to control the geometry of the wall structures. Venturini et.al adopted different strategies to build T-shaped wall structures using WAAM with optimized back surface and arc stability [60]. Li et.al observed that varying heat dissipation is one of the critical restrictions of WAAM, which degrades spatial precision and restricts efficiency. It was concluded that the modification of process parameters and increasing heat dissipation by thermoelectric cooling can resolve challenges related to melt-pool geometry [61]. Yang et al. used double electrode gas metal arc welding (DE-GMAW), a variant of the normal GMAW technique. It allows to reduce the base metal heat input and keeps the current constant by using a gas tungsten arc welding (GTAW) bypass torch [62]. With DE-GMAW, the width of built walls decreased with an increase in bypass current, while the height was observed to increase with an increase in bypass current for the same deposition rate. Besides the above, researchers attempted to use laser-

assisted WAAM to control the geometry of WAAM built wall structures. Nasstrom et.al studied the effect of introducing a laser beam to a WAAM system and investigated the geometry and material properties. Also, the effect of laser beam position with respect to the wire and arc was investigated. The topology of WAAM generated structure was improved using the trailing laser [63]. Zhang et.al used a low power pulsed laser assisted Metal Inert Gas (MIG) arc welding to build metallic components. The effect of laser parameters on the geometry of wall structures was investigated, and it was observed that the width and height fluctuation reduced with the addition of a low power laser [64]. Thus, it can be concluded that several attempts are being carried out globally to control the melt-pool instability, residual stress, spatter, and distortion during WAAM. During wire arc additive manufacturing, multi-layer deposition causes heat to build up, raising the preheat temperature of the previously formed layer. This causes process instability, which results in mechanical property changes and deviations from the specified dimensions. In addition, the accumulation of preheating temperature changes the cooling rate during the WAAM deposition, especially which results in differences in the metallurgical characteristics (like microstructure, grain morphology, dislocation density, etc.). Thus, the geometry and metallurgical characteristics of WAAM-built structures can be controlled by varying the temperature distribution during the process. Literature shows that researchers have attempted to vary the process parameters and process conditions to control the temperature distribution and thereby control built characteristics [65-66].

According to Wang et al. [67], the distance between the trailing end and the center of the molten pool increased by 1.95 mm from the first to the fifth layer due to increased heat accumulation during WAAM. Similar findings were previously published (Zhao et al.) during the thermal investigation of multi-layer WAAM deposition [68]. Zhou et al. developed a three-dimensional model to simulate arc formation and metal transfer behavior during WAAM [69]. For both single-bead and overlap deposition, the distribution of thermal conductivities and molten pool properties were studied. Because of the lower net heat flow, the molten pool's high-temperature zone is smaller during overlapping deposition than during single-bead deposition [69]. Even though this modeling and experimental study has offered some useful information, the underlying processes of arc characteristics and metal transfer behavior related to heat accumulation remain elusive due to the complexity of the WAAM process. The properties of WAAM built structures can be controlled by controlling the interlayer temperature. This can be

done by applying changes in specific dwell time or employing forced cooling [53]. Controlling the interlayer temperature can also aid in controlling the oxidation during the deposition especially during the processing of reactive materials [70-73]. Denlinger et al. found that the inter-layer dwell length, which is linked to thermal characteristics of the material, has a significant influence on the residual stresses and distortion in as-fabricated nickel and titanium alloy components [74]. Considering the wide applications (actuators, vibration damper, etc.) of WAAM built SMAs for customized MEMS devices, it is necessary to build thin wall structures with tailored geometries and built characteristics.

1.3.2 Copper based shape memory alloy fabrication through LPBF

Ti-based SMAs exhibit a good yield strength, an excellent ductility and a good corrosion resistance,in addition to an excellent SME [2]. However, Ti-based SMAs have some disadvantages when compared with Cu-based SMAs, such as high cost of the alloying elements and a relatively high production cost due to the pronounced reactivity of titanium with oxygen [75-78].Therefore, Cu-based SMAs have been widely studied due to their relative low cost, better thermal and electrical conductivity, easiness to process and higher transformation temperatures. Among the Cu-based SMAs the most interesting belong to the families of Cu-Al-Ni and Cu-Al-Zn. The Cu-Al-Zn are less expensive than Cu-Al-Ni alloys, however the Cu-Al-Ni have better thermal stability and higher operating temperatures [79-80]. The Cu-Al-Ni alloys also exhibit a great potential for applications in medical devices, as shown in tests for cytotoxicity [81], and also exhibit good corrosion resistance even in aggressive chlorine solutions [82]. Due to these characteristics, the Cu-Al-Ni SMAs present a high commercial potential, being considered the most promising Cu-based SMAs [83].Unfortunately, Cu-Al-Ni SMAs do not exhibit mechanical Properties as high as those reported for Ti-Ni, present in glow ductility, low fatigue life and tendency for intergranular cracking [76-82]. Due to this, the applications for these SMAs are limited. The addition of manganese has substantially improved their ductility without significantly affecting the transformation temperatures. Others alternatives have been sought to improve the mechanical properties of these alloys, among which grain refinement stand out, that can be obtained by small additions of alloying elements, thermomechanical treatment ,rapid solidification or powder metallurgy [76,84-87].In CuAlNiMn elemental powder has been fabricated through LPBF.

Alternative route for refining the grains is using rapid solidification techniques like melt-spinning, melt extraction [84], spray forming [87] as well as selective laser melting or powder metallurgy through cold compaction of water-atomized powders followed by hot extrusion [84]. As an additive manufacturing technique, LPBFcreates a bulk part layer-by-layer through the melting of specific, predefined areas of a powder bed [87]. The processing of a thin powder layer (20–100m) on massive substrate plates in combination with small laser spot diameters (about 100m) results in high intrinsic cooling rates [88]. These unique processing conditions have a strong impact on the microstructure (i.e. grain size) and, in turn, also on the mechanical performance. A key aspect of LPBF is the resulting porosity, which can be relatively high compared to conventionally processed material and which can cause early failure [88]. The effect of the processing parameters on the final density of the LPBF parts has been intensively studied mainly for Fe- and Ti-based alloys through the analysis of so-called single-tracks[76,88]. For Cu-based alloys, research focusing on the optimization of the relative density after selective laser melting has been done for copper-aluminum, copper-tin systems, or even pure copper alloys [89]. There are only a few publications on the fabrication of shape-memory alloys using LPBF, i.e., Ni-Ti shape-memory alloy or Cu-based shape-memory alloy [89-91]. Not only the mechanical properties are affected by the processing parameters but also the shape-memory properties can be modified using different parameters during selective laser melting [91]. The transformation temperatures of Cu-based SMAs are known to strongly depend on the chemical composition and the phases as well as the grain size in which, the transformation temperatures decrease with decreasing grain size [91-92]. This makes LPBF a very attractive method to process because the laser energy density can be controlled by the main parameters like the laser power, the scanning speed, and the spacing of the processed tracks (hatching distance) [88]. Consequently, the microstructure and the thermo-physical properties of alloys can be adjusted and designed to some extent [91]. Also, the influence of the scanning strategy has been investigated and it shows a tendency towards more anisotropic (textured) microstructures when scanning vectors are not rotated during processing [92-95]. In an attempt to improve the surface quality and to reduce micro-porosity, Yasa et al. [96] and Yadroitsev et al.[97] have combined a laser remelting treatment with conventional selective laser melting. In other words, the scanning strategy and laser remelting can be considered additional variables to modify and optimize microstructures. Post processing techniques can also help in mechanical and microstructural

properties enhancement. Hot Isostatic Pressing (HIP) is a powerful technique which showed to improve the mechanical performance of LPBF fabricated parts. Wang et.al; investigated the effect of HIP and they concluded that grain size and cell size have been increased after HIP process [98].

1.4 Layout of thesis

Shape Memory Alloy (SMA) is an essential component for several Micro Electro-Mechanical Systems (MEMS), such as actuators in valves and micro-pumps. Nitinol or Nickel-Titanium is a widely used SMA due to its outstanding thermo-mechanical behavior, pseudo-elasticity, and biocompatibility. Nitinol finds applications in various engineering fields for developing sensors, structural elements, actuators, etc. However, fabricating customized SMA-based thin structures is crucial and challenging for specific device requirements using conventional manufacturing techniques. The conventional techniques also suffer from an inability to build highly complex and customized structures. In this study, Wire Arc Additive Manufacturing (WAAM) has been used for NiTi fabrication. The key advantages of using the WAAM process for depositing NiTi structures are high speed of sample production, cheaper equipment, and lower operating costs (wire cost is substantially lower than pre-alloyed powders). With the help of WAAM, not just thin section but also complex structures like porous honeycomb structures have been fabricated. Developing SMA integrated complex structures, for example, porous structures, are of great interest due to their applicability towards biomedical implants and vibration dampers for civil structures, machinery, and automobiles (Fig.1.15). The viability is due to the distinctive stress-induced martensitic phase transformation and the substantial hysteretic loop during cyclic loading. In this study, various issues related to the WAAM system have been solved for the fabrication of complex and thin structures through WAAM. In this study, Laser Hybrid WAAM technique was used to change the surface energy of the substrate to form SMA integrated thin section. Parameters were optimized with the help of static analysis, and also preheating, interlayer delay, and interpass control have been used for reducing deposition regarding issues related to WAAM.

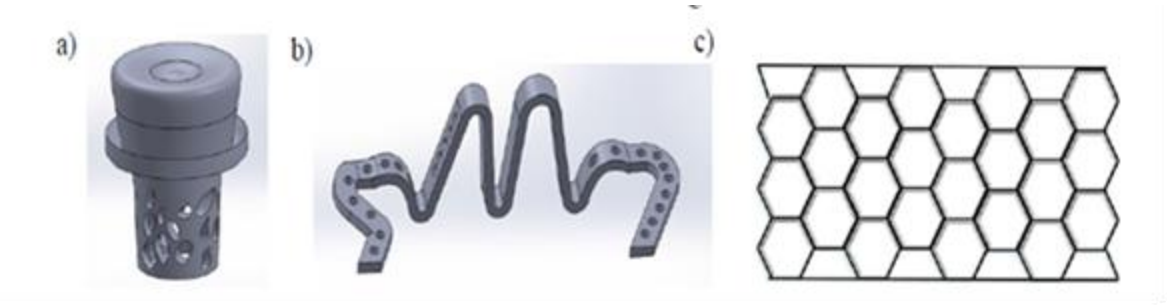

Fig 1.15 Porous NiTi structures (a) Root of dental implant (b) Traumatic surgical implant and (c) Honeycomb structure as dampers

The widely used SMA currently is NiTi for its maverick nature of getting adapted to all sought environments. However, NiTi has limitations in the aspect of hysteresis, which sequentially reduces the life of the NiTi product. In order to overcome this, NiTi has been joined with Stainless Steel, Titanium, and Copper. Dissimilar joining of Nickel-titanium (NiTi) alloy with other metallic alloys can be used to widen the applications of NiTi for developing artificial bones and joints, guide wires, and stents. The bimetallic joint of NiTi and Ti/SS/Cu is required for applications that require tailored properties at different locations within the same component, as well as to increase design flexibility while reducing material costs. Till now, there was no reported literature on bimetallic structure fabrication through WAAM.

For higher temperature applications, Copper-based Shape Memory Alloy (Cu-SMA) has been studied since Cu-based alloys were not available in the form of wire, so powder-based systems have been used. Cu-Al-Ni SMAs do not exhibit mechanical properties as high as those reported for Ti-Ni, presenting glow ductility, low fatigue life, and tendency for intergranular cracking. Due to this, the applications for these SMAs are limited. The addition of manganese has substantially improved their ductility without significantly affecting the transformation temperatures. Instead of pre-alloyed powder, elemental powder has been used, which reduces the wide gap between powder and wire-based additive manufacturing systems due to pre-alloyed powder's cost

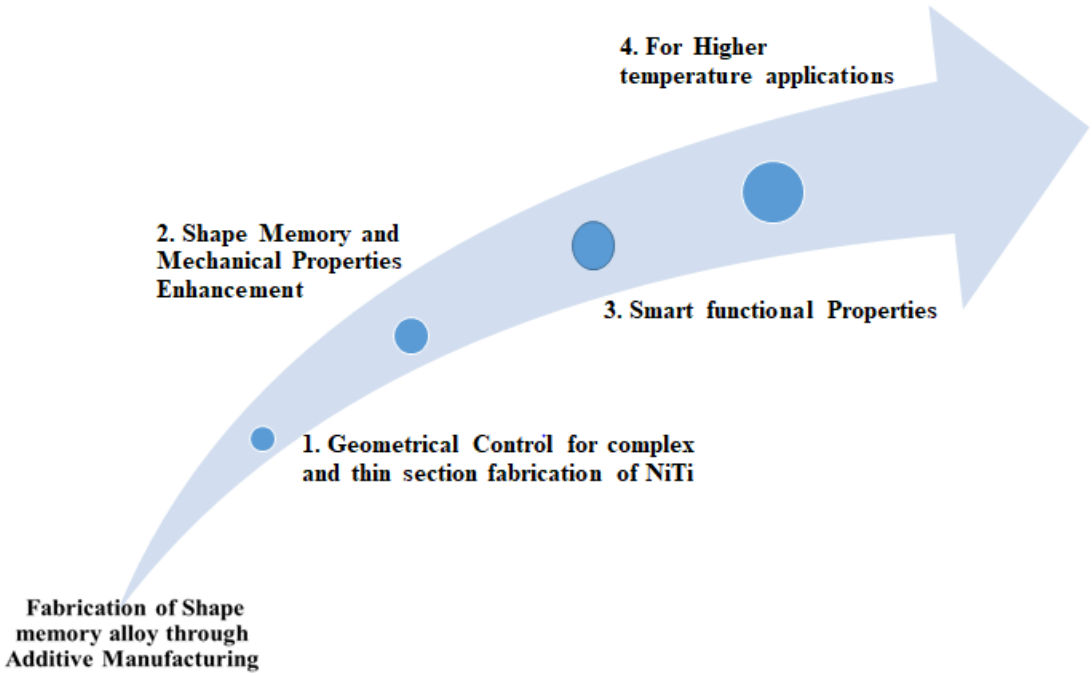

Fig1. 16 Flow representation of thesis objective

Chapter 2

Overview of material and methods

2.1 NiTi-based alloys

NiTi alloys exhibit fascinating properties such as superelastic behavior, reversible strains during heating or cooling, low stiffness, nearly bone-comparable mechanical behavior, and excellent corrosion resistance. For AM made NiTi alloys, the most exciting feature is perhaps the possibility of manipulating the shape memory behavior of AM made NiTi components using the laser parameters. For instance, the final microstructure and hence transformation temperatures can be altered by a modification of the scan parameters and scan strategy. On the other hand, AM design freedom enables manufacturing complex geometries such as porous structures with repeatable unit cells that may change the shape memory behavior of the component. Nitinol wires with composition $Ni_{50.9}Ti_{49.1}$ and 1.2 mm diameter is used as the feedstock material for this work. Table 1 presents the properties of NiTi used for deposition [48-49].

Table 2 Properties of NiTi wire

Properties	Value
Density	6.45 gm/ cm^3
Melting Point	1310 °C.
Resistivity	76-82 ohm-cm
Thermal Conductivity	0.1 W/cm-°C
Heat Capacity	0.077 cal/ gm-°C
Ultimate Tensile Strength	754 – 960 MPa
Typical Elongation to Fracture	15.5%
Typical Yield Strength	100MPa-560MPa
Latent Heat	5.78 cal/ gm
Elastic Modulus	28 – 75 GPa
Poisson's Ratio	0.3

AM fabrication of NiTi alloys is reported to be very successful. This enables engineering/customizing the desired functional property (i.e., shape memory effect or in contrast superelasticity) according to any specific application. Despite some concerns over Ni ion release, the corrosion resistance and biocompatibility of AM made NiTi-alloys are considered to be adequately high due to the presence of surface oxide films on the manufactured components.

2.2 Experimental Setup of WAAM:

Gas Metal Arc Welding (GMAW) machine (Make and model: ESAB Inverter MIG 400) is used for WAAM of Ni-Ti. Fig.2.1 presents the schematic of WAAM system used for deposition, which essentially consists of a welding torch, wire feeder, and motorized XYZ stage. The wire feeder supplies the wire as a feedstock to the welding torch and XY stage is used to move the welding torch in a layer. The G and M code control the XY stage movement, and the M code controls the XY stage movement from the Repitier host device. This system has been used for all work for NiTi which has been explained in chapter 3 and 4.

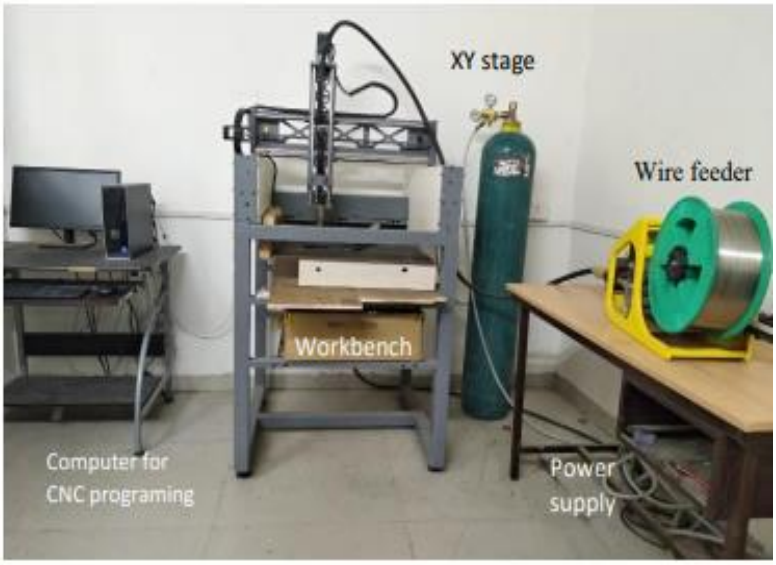

Fig. 2.1 Wire Arc Additive Manufacturing Experimental Set-up

2.3 Characterization tool

The wire-cut electrical discharge machine is used to cut deposited samples transverse to the laying direction. Further, samples are prepared using standard metallographic practice. A one-color pyrometer Sensortherm METIS M318 (Sensortherm GmbH, Sulzbach, Germany) with a temperature range of 150 to 1200°C and a spectral range of 1.65–2.1 m was used to measure the temperature on the surface of the previously deposited layer and a thermal camera was also used Optris Xi 400 2 (18° lens) with a temperature range of 100 to 1500 °C. The width and height are measured at various locations using a sick profilometer (PRO2-N100B25A1 (6052874)).Porosity distribution is measured using the X-ray tomography technique (Make and Model: ZEISS and Xradia 620). WAAM built wall structures are scanned with Comet Blue Light LED 3D Scanner (Make and Model – ZESIS and COMET L3D) for obtaining the 3D image. The microstructure is analyzed using an optical microscope (Make and Model: Carl Zeiss Axiovert A1 inverted).X-ray diffraction studies (XRD) is performed using an X-ray diffractometer (Make & model: BRUKER-D8 Advance) from 20 to 90 ° (step size: 0.02 ° and dwell time: 0.5s). The Scherrer equation is used to compute crystallite size, and JCPDS file number 00-035-1281 is utilized to calculate XRD lattice parameters. Scanning electron microscope (SEM) attached with Energy Dispersive Spectroscopy (EDS) (Make & Model: S-4800 Hitachi) is used for microstructural and composition analysis. The surface contact angle is determined using an optical tensiometer (Make and Model: Attension® Theta Lite 101) with water as the wetting agent. Images of the drop shape are recorded every 30 seconds. The average values of the contact angle are determined based on 10 measurements. The marking depth is measured by a 2D Height gauge. Roughness for marked trench on titanium pate is measured with the help of an optical profilometer (Make and Model: Wyko NT9100). The microhardness at 1.96 N load is measured using Vickers microhardness tester (Make and Model: WlterUhl- VMHT002) with a dwell period of 10 seconds. The sample size (as per ASTM 9) with dimensions of 3 mm width and 6 mm length was used for compression test. Testing Machines Limited, West Midlands, UK) was used for tensile test.The tensile test samples (ASTM: E8/E8M – 13a) were dog bone samples with a total length of 20 mm that was used (Fig. 2.2).

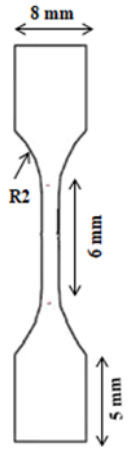

Fig. 2.2 LPBF build sample for tensile testing

2.4 Methodology of smart structure fabrication through Additive Manufacturing

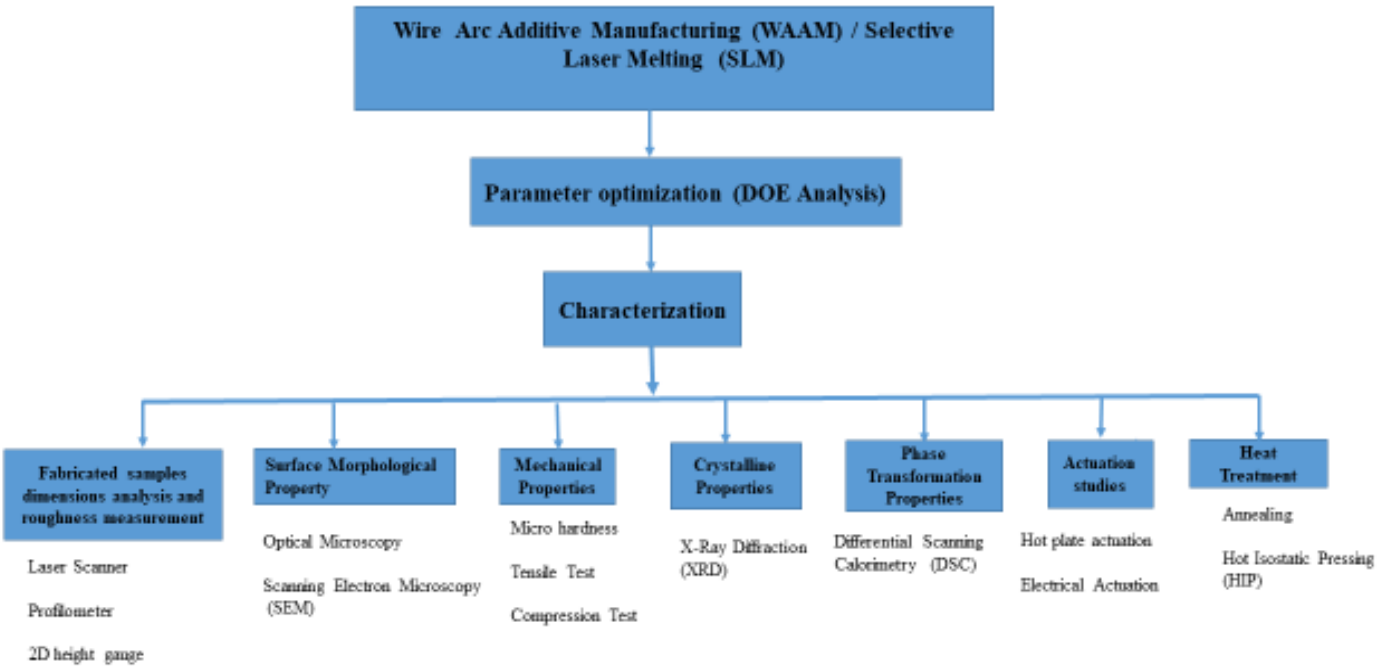

Fig. 2.3 Methodology flowchart

Chapter 3

Investigations on NiTi Shape memory alloy thin wall structures through Laser Marking, Interlayer delay and Interpass Control Assisted Wire Arc Based Additive Manufacturing

3.1 Laser Marking assisted WAAM

Fabricating customized SMA based thin structures are crucial and challenging for specific device requirements using conventional manufacturing. The above issues can be addressed using advanced manufacturing techniques, like -Wire Arc Additive Manufacturing (WAAM) technique. However, fabrication of the thin-wall structures with controlled geometry using WAAM is technically challenging due to melt-pool instability, residual stress, and distortion during fabrication. One of the methods to address the above issues is hybridization of WAAM with pre-surface treatment using Laser-marking. In the present work, the effect of number of laser passes during laser marking is investigated and the deployment of laser-marking treatment before deposition of each WAAM layer reduced the surface roughness (24 μm to 2.8 μm) and surface energy, which reduces the track width. The defects and distortions are successfully eliminated with 2 mm width of marked laser track on which thin section is fabricated. The fabricated samples are systematically investigated using characterization techniques to examine their surface morphological and mechanical properties. Shape Memory recovery of the fabricated sample is also investigated through its actuation characteristics by joule and hot plate heating with maximum achieved displacement of 2.4 mm. Through this technique, feature size of WAAM can be reduced, which will play a significant role in fabrication of complex components with thin structures.

3.1.1 Experimental Setup

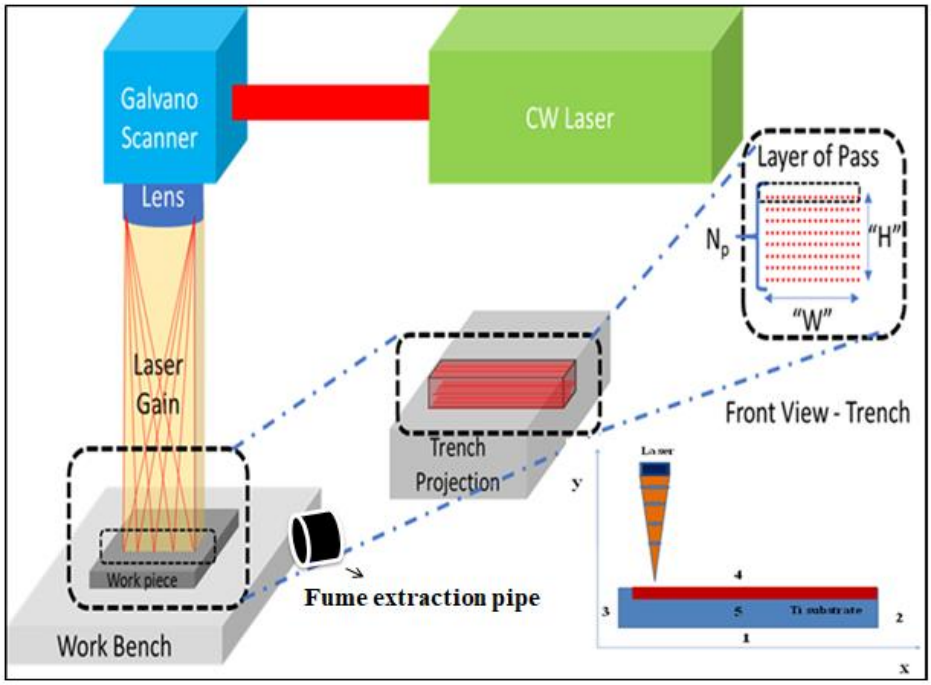

Fig.3. 1 Schematic diagram of laser marking Setup

Fig. 3.1 presents the schematic of laser marking setup used for the experiments. Titanium substrate of thickness 10 mm is used as a substrate material. Titanium is selected as the substrate material primarily due to the compositional compatibility with nitinol [99-100].

A continuous Ytterbium-doped fiber laser of wavelength 1064 nm with maximum power 50 W is used for the laser marking. The laser beam path is controlled using a Galvano scanner and focused using flat field lens on the surface and a fume extraction pipe was also used for evaporated material and fume removal from the working environment. The laser system is computer-controlled, allowing the generation of geometric patterns. A constant laser power and scanning speed of 50 W and 50 mm/sec, respectively are used during the study. Laser marking is performed by varying the number of passes at a constant laser power and number of passes.

Gas Metal Arc Welding (GMAW) machine (Make and model: ESAB Inverter MIG 400) is used for WAAM of Ni-Ti and other details about system has been given in section 2.2.The deposition is carried out on two levels. Initially, single tracks are deposited by varying the wire feed rate and voltage. The scan speed, argon gas flow rate and stand of distance used for deposition are 8.57 mm/s, 20 l/min and 15 mm, respectively. The voltage and wire feed rates are varied between 17 – 18 V and 4.5 – 5.5 m/min, respectively, for the single track analysis. The tracks

with continuity and uniformity are selected for wall deposition. Thus, voltage of 17.5 V, feed rate- 5.5 m/min, current of 120 A and dwell time of 600 sec between layers is used for building wall structures.

3.1.2 Numerical Modeling

Numerical modeling is used to find the temperature variation along the processed trench length on the Ti substrate. The simulation study is carried out using COMSOL to simulate the moving laser beam as a heat source over the physical domain. The temperature distribution is determined through interaction modeling of the selected materials with the laser beam in TEM_{01} mode. The heat conduction principle is considered and solved as the main physics for this problem as shown in equation 1, where Q is heat input, t is time, k is thermal conductivity, ρ is density, C_p is specific heat capacity, A is the cross-section of the material, T is the temperature difference, and Δx is the distance between the heat sources. The conduction speed depends on the material density, specific heat capacity, thermal conductivity, temperature difference, and material [101]. Table 3 presents the material properties of Titanium used for simulation.

Table 3 Properties of Titanium

Density(G/ cm^3)	4.5
Thermal Conductivity (W/mK)	15-20
Melting Point (^oC)	1670
Heat of fusion($kJ*mol^{-1}$)	14.5
Specific heat capacity($J*mol^{-1}*K^{-1}$)	25.06
Elastic modulus (GPa)	115
Phase	Solid

$$\frac{\Delta Q}{\Delta t} = -kA\left(\frac{\Delta T}{\Delta x}\right) \rho C_p \frac{\partial T}{\partial t} + \nabla.(-k\Delta T) = Q \ldots\ldots\ldots\ldots (1)$$

The heat source with a Gaussian profile along *x*-direction is described according to the Beer-Lambert law [29] as shown in equation 2, where P, R, r_b are the laser output power, the absorption coefficient, the reflection coefficient, and the effective laser radius, respectively.

$$Q= \frac{2P\alpha}{\pi r_b^2} (1-R) \exp\left(\frac{-2x^2}{r_b^2}\right) \exp(-\alpha y) \quad \ldots\ldots\ldots\ldots\ldots\ldots\ldots (2)$$

X is the transverse coordinate, where *x*= 0 is the beam center position, and *y* is the longitudinal coordinate, where *y* = 0 is the surface of the material. Beam spot diameter of 600 µm is used for the analysis. Table 4 lists the boundary conditions applied to each edge numbered in Fig. 3.1. Free tetrahedral meshing is used for the analysis. The Dirichlet condition is followed by setting surface temperature T_0 constant value at boundaries 1 and 3. The heat flux between the sample and the atmosphere is known at boundaries 5 and 2 due to heat losses attributable to radiative and convective heat transfer [102-103].

Table 4 Boundary conditions of the simulation model according to the edge numbers indicated in Fig.2.1

Boundary	Boundary conditions
1,3	$T= T_0$
5,2	$n*(k\nabla T) = h_{Ti} (T_0-T)+ \sigma\varepsilon_{cTi} (T_{04}-T^4)$
4	$n*(k_{c\,Ti}\nabla T) =0$

3.1.3 Results and Discussion

3.1.3.1 Effect of Laser Marking on Titanium Substrate

Fig. 3.2a presents the typical temperature distribution obtained using numerical simulation. It can be seen from Fig. 3.2b that the temperature increases with increase in the number of passes. In the present work, it is observed at a constant laser power and scanning speed, melting temperature is achieved after 25 passes and vaporization temperature is achieved after 50 passes. Thus, experimental work is carried out by using 50 passes and the number of passes is increased by 50 to understand the effect of number of passes on the marking depth.

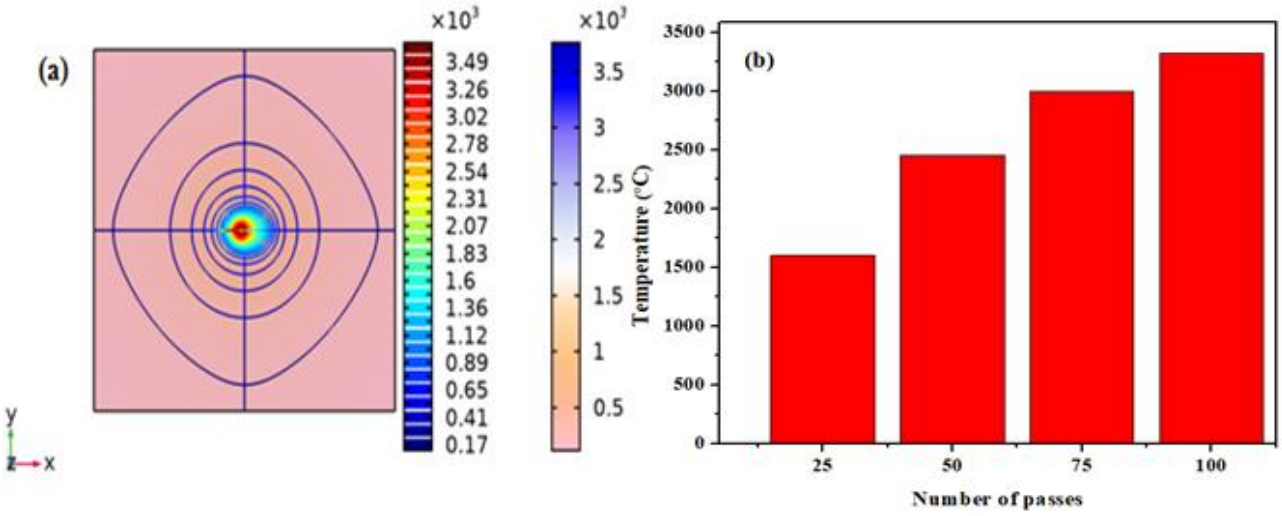

Fig.3.2 (a) Temperature distributions through titanium plate and Laser marked surface (b) Temperature vs number of passes during laser marking graph

Table 5 presents the effect of the number of passes on the surface roughness, contact angle, and depth of the laser marking trench, and Fig. 3.3 (a) presents the typical image of the Laser marking trenches generated on the material surface. It is observed that at a constant scanning speed and laser power, channel depth increases with an increase in the number of passes, while the channel width is only slightly affected. This is primarily due to the more amount of laser energy available at the substrate surface, which increases the vaporization depth. Also, as the number of passes increases, the substrate's temperature increases, increasing the substrate's laser absorptivity. A consistent observation through the images reveals a non-flat bottom. The TEM_{01} mode of beam makes shallower grooves at the center of bottom with more in-depth at the sides. The TEM_{01} mode allows concentrating low energy at the center of the beam and more energy at the edges. The roughness profile reduced with an increase in the number of laser passes due to the consistent impact of laser beam irradiation and the rapid vaporization of materials.

Table 5 Effect of number of laser passes on marking depth, roughness and contact angle

Sr. No.	No. of passes	Laser Power(Watt)	Depth	Roughness (µm)	Average Contact angle(°)

1	350	50	1.5 mm	2.8	89.7
2	300	50	1mm	3.12	83.4
3	250	50	857 µm	5.9	76.9
4	200	50	638 µm	11.2	71.25
5	150	50	457 µm	13.52	65.1
6	100	50	358 µm	18.7	46.1
7	50	50	250 µm	21.3	44.3

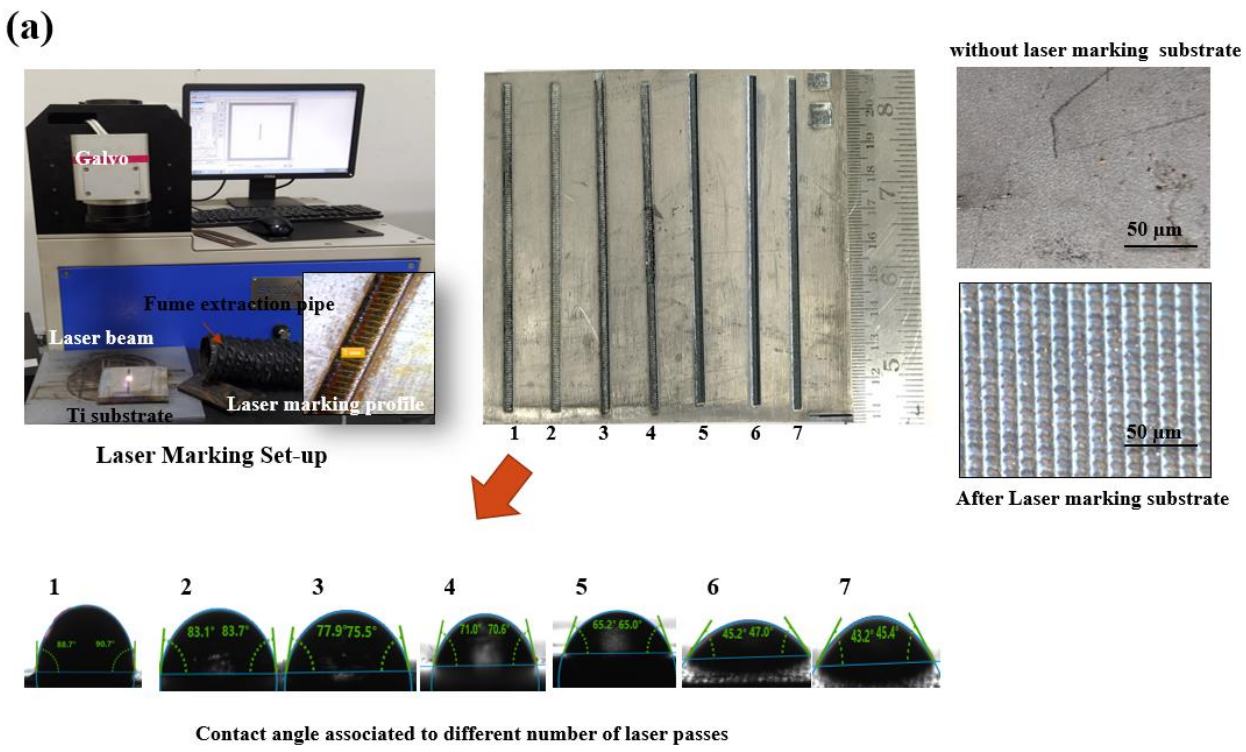

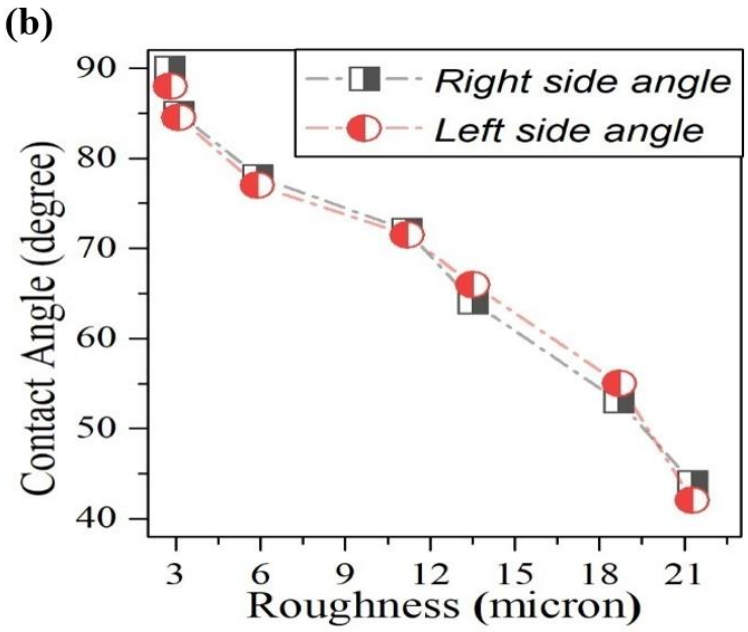

Fig. 3.3 (a) Schematic of Laser marking process on titanium plate (b) Contact Angle vs. Roughness graph

The roughness of substrate strongly modifies the wettability of surface. The wettability of surface is analyzed in terms of surface free energy (SFE) Fig.3.3 (b) shows the inverse relation between contact angle and surface roughness of the marked surface. The contact angle is measured after deposition with a single water drop on substrate with and without laser treatment. Different planar faces along the crystal interfaces have different surface energies and, therefore, different contact angles. Young's equation (Eq. (3)), which is applicable for surface tension calculation, is valid for smooth surfaces and can be modified using the parameter of roughness (r).

$$\text{Cos } \theta = \frac{r(\gamma_{sv} - \gamma_{sl})}{\gamma_{lv}} \quad \ldots\ldots (3)$$

Where, θ is the contact angle of the surface, $\gamma_{sv}$is the interfacial tensions of the solid-vapor phases, γ_{sl} is the interfacial tensions of the solid-liquid, γ_{lv} is the interfacial tensions of the liquid-vapor phases, and r is the roughness ratio. The roughness ratio is determined from a 3D roughness parameter and is defined as the ratio between the actual and projected solid surface area (r=1 for a smooth surface and r > 1 for a rough one). [104-105].

3.1.3.2 Microstructure and XRD analysis

Fig. 3.4 (a) and(c) presents the microstructure of the base titanium plate before marking and Fig. 3.4 (b) and (d) presents the microstructure after laser treatment. The microstructure consists of elongated α-Ti and the presence β-Ti lamellae in the inter-granular region before marking (Fig 3.4 c). The as-received microstructure suggests it had been undergone cold rolled process. The average grain size varied between 350 μm to 250 μm and 50 μm to 100 μm for before and after marking, respectively. Laser surface melting led to significant refinement of the microstructure and due to a very high cooling rate, which also caused acicular α-martensite formation as shown in Fig 3.4 (d). Fig. 3.4 (e) shows the XRD graph for titanium substrate before laser treatment and after laser treatment. Before laser treatment, mixture of α titanium and β titanium belonging to the hexagonal lattice structure is present. However, after laser treatment, titanium oxides and nitride (JCPDS 38-1420) are found, belonging to tetragonal and monoclinic structures, respectively. The formation of titanium oxide and nitrides are the reason for the color change after laser treatment. If the surface temperature is held below the boiling point of titanium, 3550 K, during laser irradiation, the titanium's surface product, titanium nitride, is expected to form by a liquid titanium-ambient gas reaction.

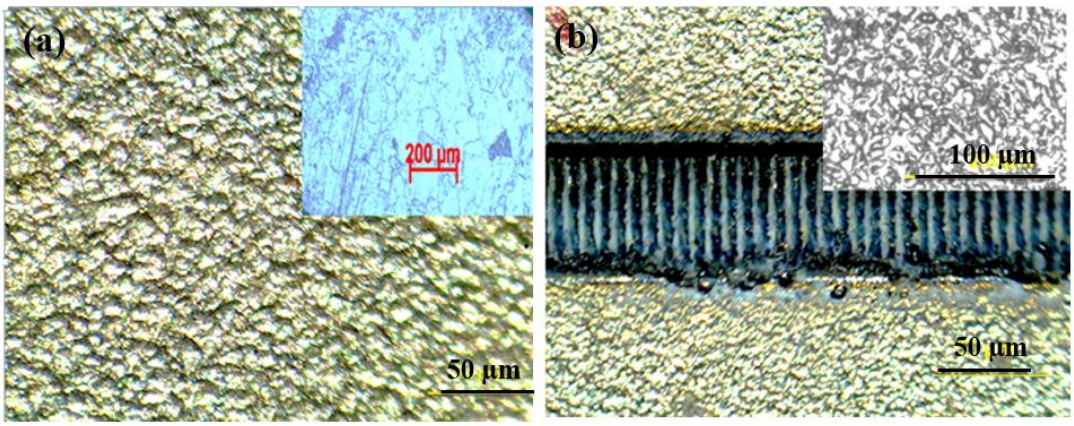

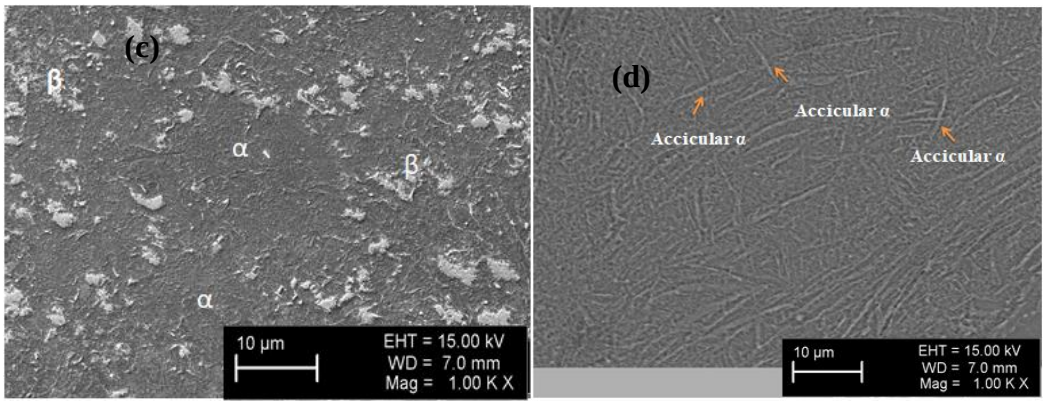

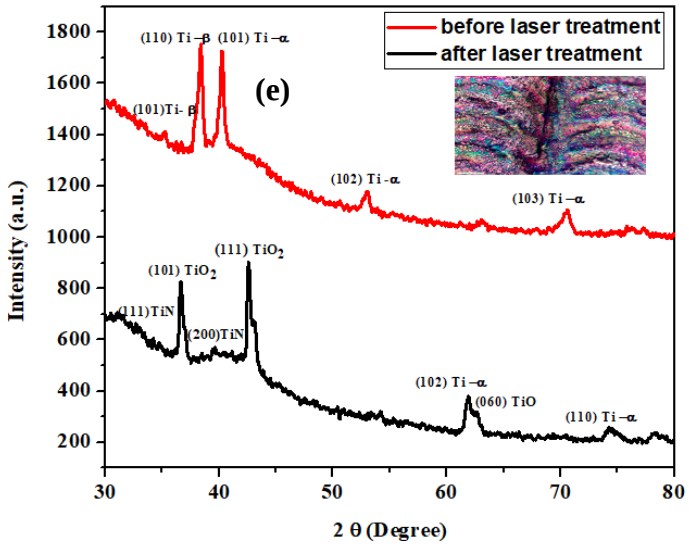

Fig. 3.4 Titanium plate (a) before laser treatment,(b) after laser treatment, (c) SEM result for without marked substrate, (d) SEM image of laser marked substrate, and (e) XRD graph for titanium plate

Nitrogen can diffuse into the vicinity of the surface and forms an interstitial nitrogen solid solution in α-titanium phase. Laser marking has been done in open environment so atmospheric nitrogen will react to titanium substrate and form nitrides. With increasing laser passes, the temperature in the irradiated area of sample rises, which enhances the diffusion of nitrogen into the surface [106-108]. The decrease in the β-Ti content due to laser surface melting is significant. The volume fraction of β-Ti following melting is attributed to the stabilization of acicular martensite in the structure during rapid quenching. After laser treatment, the titanium color will change due to galvanometric effect (which enables the investigation of the accumulative thermal

effects)in which different compounds (oxides and nitrides) will form [109].Formation of α and β will also get affect due to temperature variation and cooling rate during the laser marking. Hence, during the laser heating, zones with temperatures above and below the β transus (882℃) will be transformed into β phases or keep α phases unchanged, respectively. The formation of β-Ti is suppressed by nitriding [110].

3.1.3.3. Process optimization for WAAM (effect of process parameters and quality)

In WAAM deposited tracks (Fig. 3.5) most specimens show signs of slight oxidation on the bead surface as well as in the substrate's heat-affected zone. In certain cases, the oxidation occurred as a blue or purple and if the thickness of the oxide layer decreases, pigment changes to gold or straw pigment.These geometric properties are called humping and undercutting. The fluid flow within the molten pool can cause the 'humping' and 'undercutting' [111]. The alleged force behind the movement is that of Marangoni effect, or more precisely the thermo capillary effect, in which fluid movement is induced by changes in surface tension [111].Heat input per unit length will help study the effect of welding parameters on Marangoni force which will affect the weld bead geometry.This parameter is referred to as the linear energy and is defined as ($IV=Q_w$)….. (4)

Where I is current, V is voltage and Q_w heat input.

Due to high energy spatter and non uniformitywas present throughout the all track. Ripples are also present throughout the tracks due to oscillation frequency of arc [111] .Parameters was optimized on the basis of track quality for deposition which is shown in Fig. 3.5 and observed width and height were also mentioned in Fig.3.6 (a)& (b). In all cases, the bead was not considered acceptable for AM applications due to their excessive height variations and dis-continuities; therefore they were excluded from further evaluation. But still 6th track is continuous so for the further evaluation experiment was repeated for the same parameter.

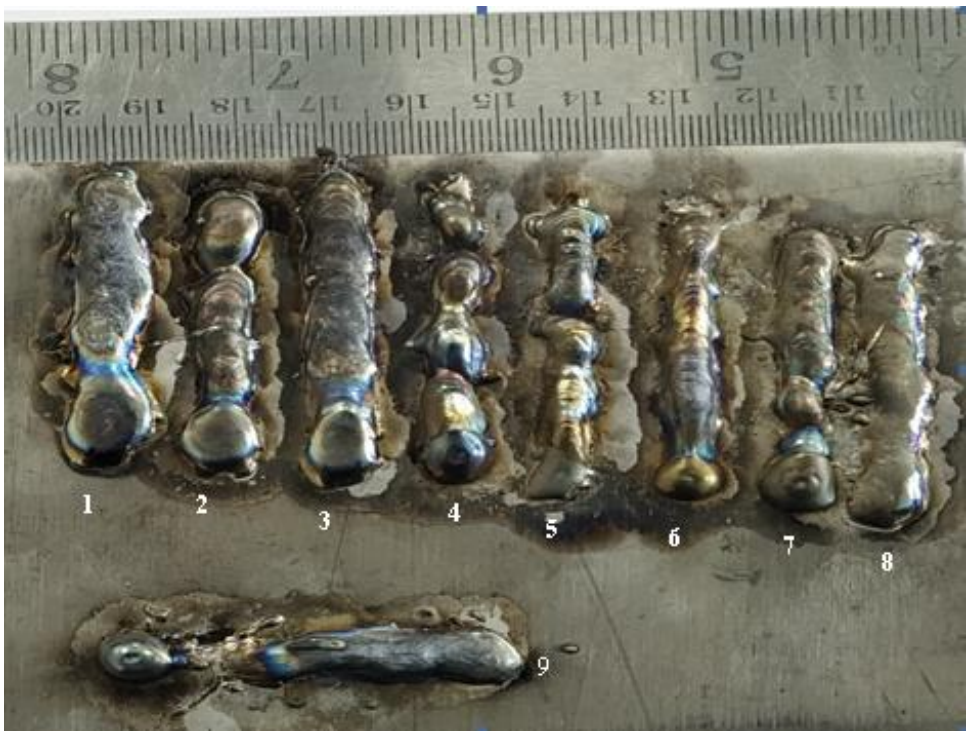

Fig.3.5 WAAM track deposition at different parameters

Table 6 Optimized parameters for the WAAM Deposition

Bead No.	Wire feed rate(m/min)	Argon gas flow rate (L/min)	Voltage (V)	Heat Input(J/mm)	Torch travel speed (mm/s)	Remarks Linear Energy
1	4.5	20	17	11.985	8.57	Voltage was insufficient due to which spatter is more
2	5	20	17	10.79	8.57	Height is more because weed feed rate is high but discontinuity is still there

						throughout the track
3	5.5	20	17	10.03	8.57	Voltage is insufficient due to which spatter is there
4	4.5	20	17.5	10.85	8.57	Feed rate is very less due to which depressions are present throughout the track
5	5	20	17.5	11.11	8.57	Voltage is high for this feed rate because of which undercutting and discontinuity is present
6	5.5	20	17.5	9.53	8.57	Continuity is there but still ripples is there
7	4.5	20	18	10.35	8.57	For this voltage feed rate is not sufficient
8	5	20	18	9.9	8.57	Voltage is high due to which weld bead width is high and arc is and travel is too slow at this parameters
9	5.5	20	18	9.27	8.57	Travel speed - too fast

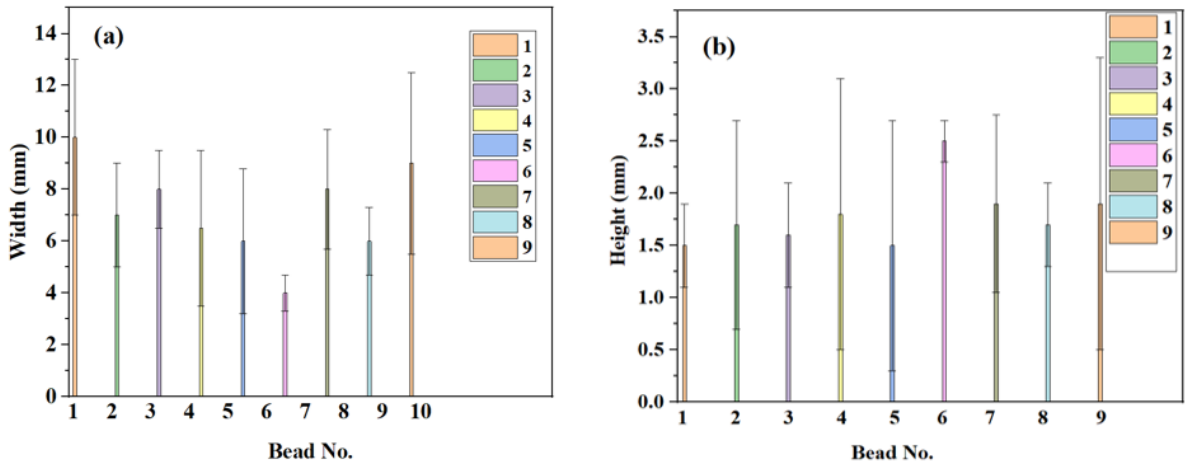

Fig.3.6 Effect of WAAM parameter on the wall (a) height and (b) width in thw WAAM built NiTi-based walls.

3.1.3.4 Effect of Laser marking on WAAM structures

3.1.3.4.1 WAAM deposite single tack and multi layer profile

In additive manufacturing, the track geometry is a building block for deposition of any complex shaped component. 1st layer was the layer deposited on the Ti substrate for after laser marking and without laser marking. Otimized parameter was also used for multi layer wall deposition. Roughness and surface energy will change after marking along with a 1.5 mm deep track will provide the path for unstable melt pool. The Ni concentration in the NiTi wire used for the WAAM sample production was 50.9 at. %. Therefore, the composition after 2nd layers was close to the composition of the initial wire for the without laser marked sample and there will not be any modification in the mechanical and shape recovery behaviour. On the other hand, the Ni concentration in the 1st and layers was lesser than in the wire for without laser marked sample after deposition. Formed phases and structure will get modify due to laser treatment on the deposited track which will increase the Ni rich phase which will enhance mechanical properties along with shape recovery behaviour. The single star mark (refer Fig. 3.7a) indicates the deposition done after laser marking, and the double star (refer Fig. 3.7a) shows deposition without laser marking. In WAAM, it can be observed that as the numbers of layers increase, the track width also increases. When the first layer is deposited, the substrate is flat, and due to the surface tension, the melt pool tries to form curvature; hence track has some concavity on its

surface. As the second layer is deposited on the first layer's curved surface, the molten metal, starts flowing due to the gravitational force, which leads to an increase in width. It is also being observed that the laser marking deposition is more uniform and thinner as compared to without marking deposition. The fluid flow within the molten pool can cause the 'humping' and 'undercutting' [111]. The alleged force behind the movement is that of the Marangoni effect, or more precisely, the thermocapillary effect, in which fluid movement is induced by changes in surface tension [112]. Ripples are also present throughout the tracks due to the oscillation frequency of the arc [113]. Contact angle test is also performed for marked deposited track after marking to predict further layer formation (shown in Fig 3.7(b)). Laser treatment on the deposited track will reduce porosity and cracks and along with this it will improve shape recovery by increasing the R phase which will increase amplify the two way shape memory effect which will form due to temperature increment above 700^{o}C during the laser treatment on the deposited layer. Both Ni rich phases (as shown in Fig 3.8 (f)) could be found after laser treatment which will contributed in the formation of R phase [115].Due to this shape recovery is high for laser marked sample [116].

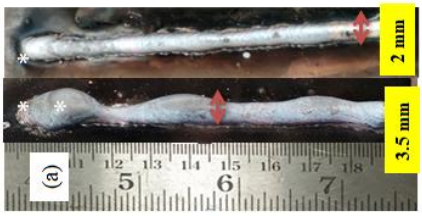

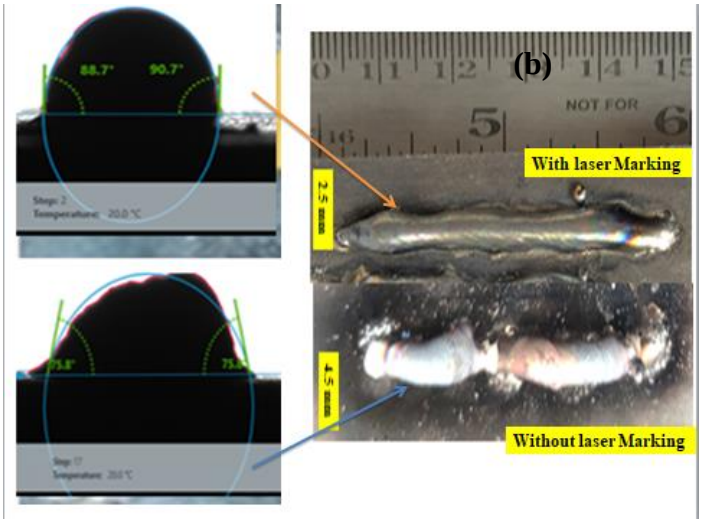

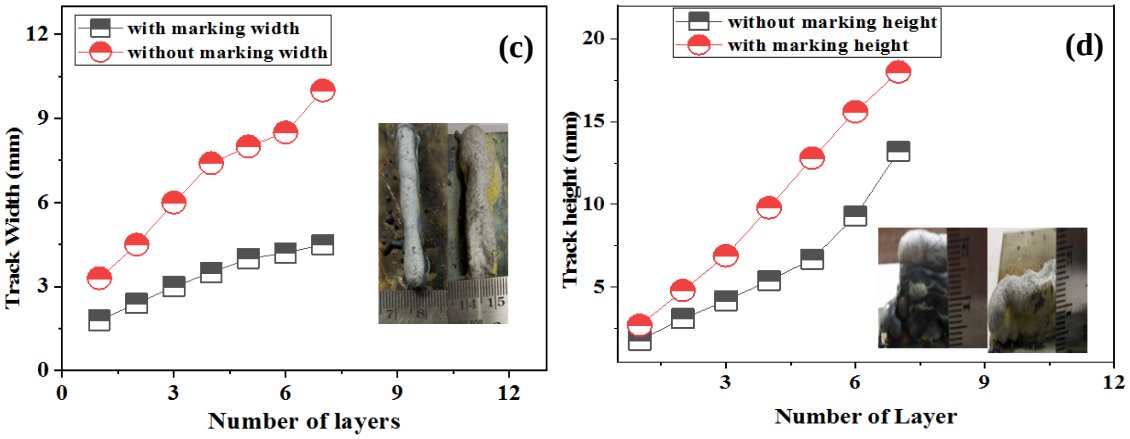

Fig. 3.7 (a) WAAM deposited track with marking and without marking (b) WAAM deposition of double-layered track along with contact angle, (c)Track width Vs. number of layers graph and (d) track height Vs. number of layers graph

It is observed that the track width after laser marking is less compared to the track width without marking. This happens because laser marking provides the path to flow the molten metal in the confined zone. It is also observed that the tracks built with laser marking are uniform without any ripples and depression along the track length due to the melt pool's stability. The difference in track height and track width after laser marking is shown in Fig.3.7 (c, d) up to 7 layers, and in this, laser marking is done before each track deposition. After each layer, laser marking will change surface roughness, wettability, and free surface energy of the previously deposited layer.

3.1.3.4.2 Microstructure studies

Fig. 3.8 (a) and (c) depicts the microstructure of WAAM sample built without and with laser marking. The columnar grains were found in samples built with and without laser marking. However, samples without laser marking revealed relatively coarser grain structure. The grain size is found to be ranging from 60 µm to 120 µm for without laser marked sample and 20 µm to 35µm for a marked sample. Fig.3.7 (b, d) show the SEM elemental mapping results of WAAM deposited tracks without and with marking.

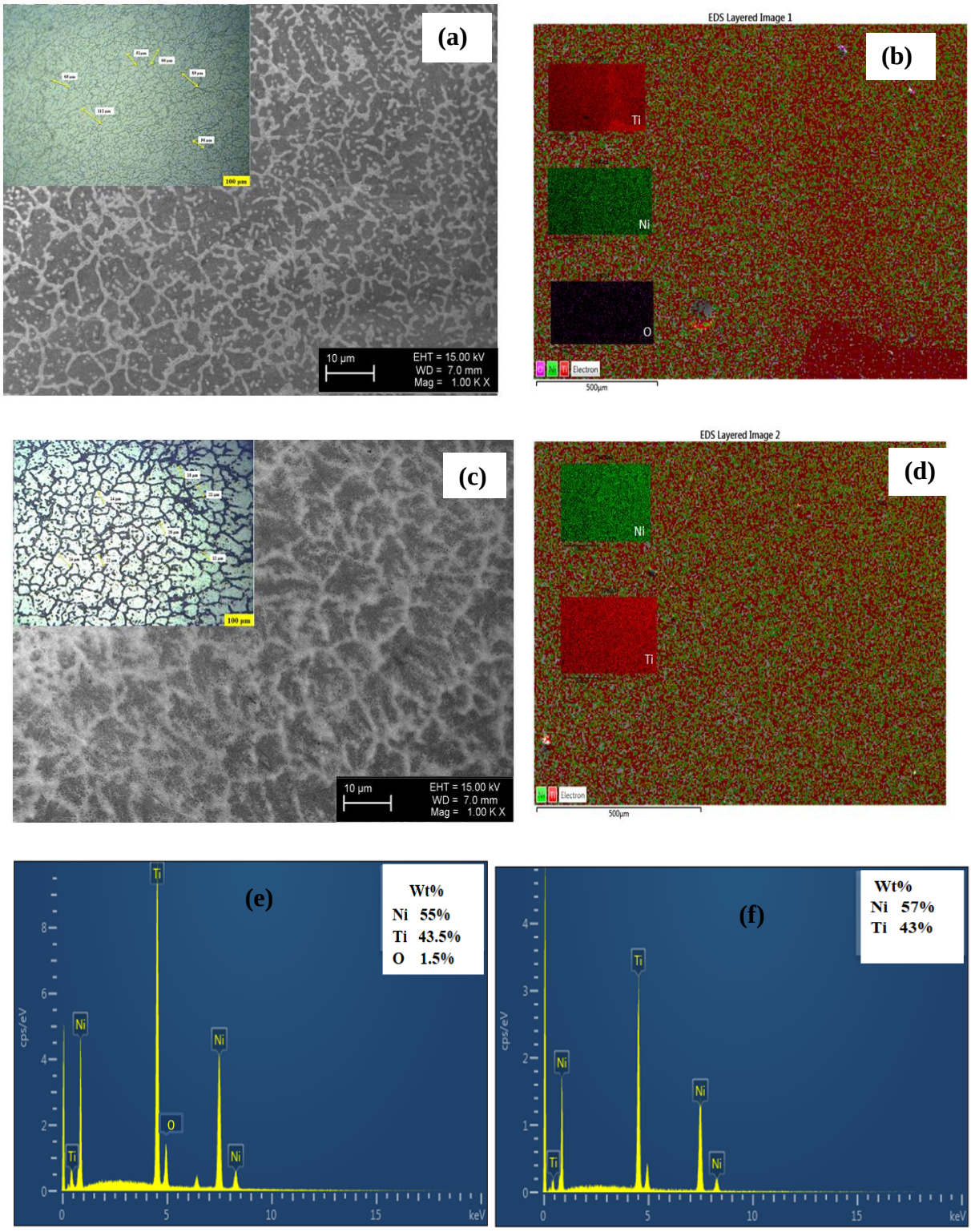

Fig. 3.8 (a) SEM result for without Laser marked sample, (b) Elemental mapping results for without Laser marked sample, (c) SEM result for marked sample and (d) Elemental

mapping results for marked sample, (e) EDS result for without marked sample and (f) EDS result for marked sample

Different regions rich in Ti and Ni are located in different layers. In samples without laser marking, oxides layers are formed due to low cooling rates as compared to the marked sample. Wide surface area in laser marked samples leads to high heat flow to the substrate/ previous layer leading to higher cooling rate. At high-temperature, titanium will react to atmospheric oxygen, and melt pool of walls built without marking lead to more contact between the atmosphere and melt pool leading to oxide formation. Even with the inclusion of such unexpected oxides, the WAAM structure still has a structural and elemental discontinuity. When faced with a huge oxide island, the weld pool bypasses the island and changes the wetting boundary to an irregular curve until the weld pool passes it completely.

3.1.3.4.3 Mechanical Properties

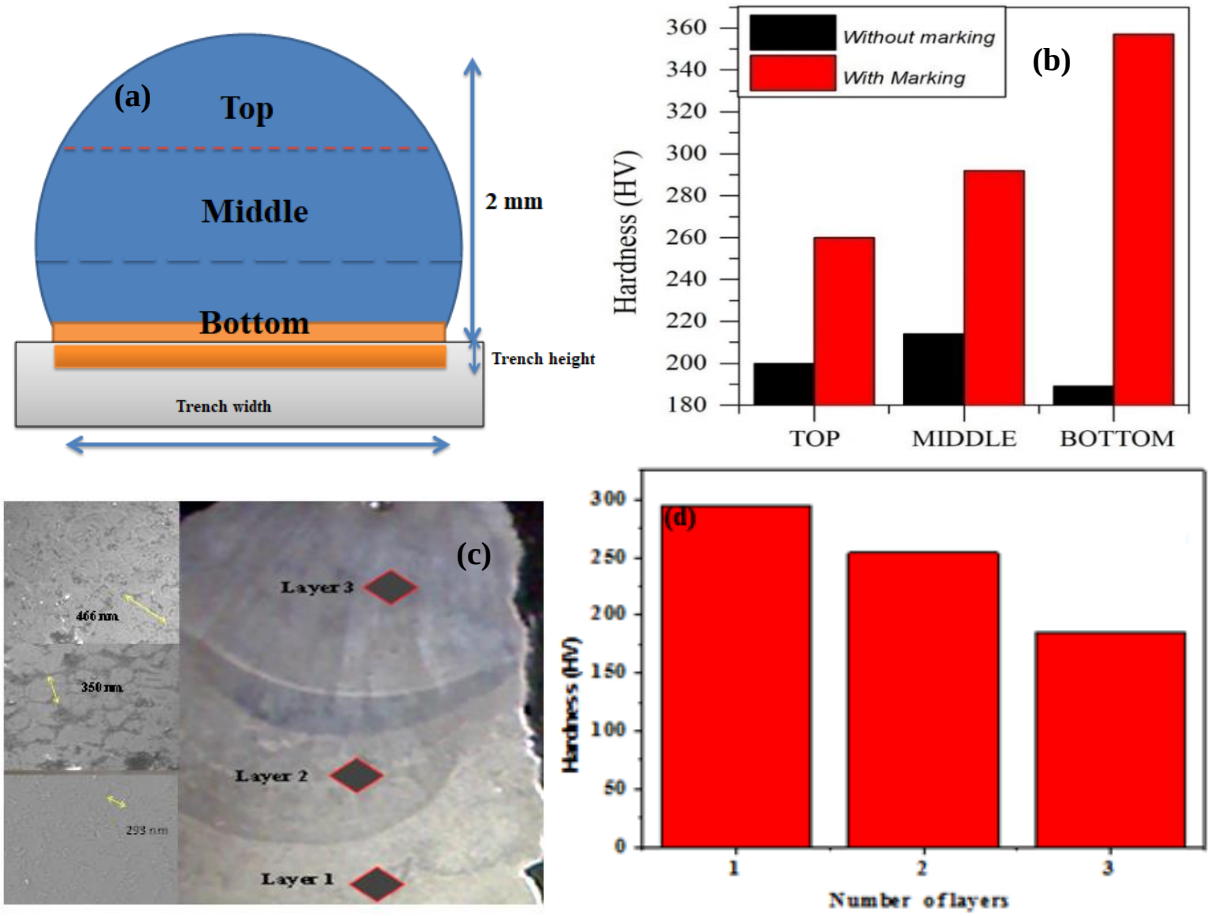

Fig.3.9 (a) Location at which microhardness measured (b) Microhardness value, (c) Panoramic view along with SEM image and (d)hardness test of a multilayer structure

The average micro-hardness of the single-track of WAAM deposited NiTi varies from 200 HV to 350 HV, as shown in Fig. 3.9 (b). It can be seen that the hardness of the bottom section is higher than the middle section and the top section. The laser marking provides a larger cooling rate due to its large surface area and high heat flow to the substrate. The middle section and the top section have a relatively low cooling rate because of the low thermal gradient in the melt pool. After each layer of deposition in the wire arc additive manufacturing (WAAM) process, the deposited metal experiences a rapid cooling rate, which leads to high residual stresses and, in some cases, micro cracks. These issues can lead to a reduction in the mechanical properties of the final product. Laser marking after each layer in the WAAM process can help to alleviate these issues by reducing the residual stresses and improving the mechanical properties of the deposited wall. The laser heats the deposited metal, causing a more gradual cooling rate and allowing for the reduction of residual stresses. Laser treatment is done after each layer deposition for reducing porosity and increasing grain refinement due to this hardness is higher than the without marked sample as shown in Fig. 3.9 (d) [117]. In order to evaluate the bulk mechanical properties of the samples, compression test was carried out as shown in Fig.3.10. It can be seen that laser marked samples have higher strength due to grain refinement, lower porosity and Ni rich phase formation. The results from the compression test are in line with the results obtained from metallurgical characterizations [106].

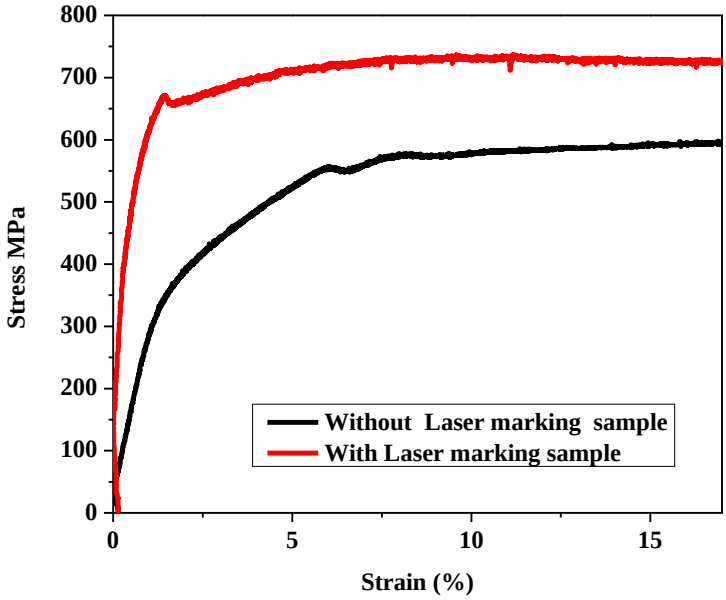

Fig.3.10 Compression behavior of NiTi with and without laser marking

3.1.3.4.1 Actuation studies

A set-up based on Joule heating (electrical actuation) is utilized for the testing of suitability of using the WAAM sample in MEMS application to evaluate the sensing and bending capabilities as shown in the schematic diagram in Fig. 3.10 (a) and schematic of hot plate is also shown in Fig. 3.11 (g). Fig. 3.10 (b), (c), (d) and (e) shows the change in recovery angle with respect to time and temperature of the hot plate. Generally, the actuation properties of the shape memory alloy relays on the latent heat of transformation and specific heat of the SMA due to various thermal response and properties. Mainly, the setup based on Joule heating is made up of a laser displacement sensor, data acquisition module, an Arduino-relay circuit with programmable power supply. In the ice bath, sample NiTi sample was bent around a mandrel with a radius of 2 mm (in the martensite state). This results in a 25% bending deformation of the samples. After unloading, both samples were characterized by the same residual strain. Then, at room temperature, one side of the sample was fixed, and the other was connected to a load of 35 g (Fig. 3.11 a). The NiTi based SMA undergo phase transformation below 150 ^{o}C, which affects the actuation behavior of SMA. In addition, the various properties such as the thermal conductivity and electrical resistance of SMA affect the shape change during the actuation of the

SMA structure [118]. Hence, the thermomechanical behavior and the identical experimental conditions were selected after detailed optimization. The heating and cooling of the SMA structures is switched by Arduino relay circuit for a duty cycle of 15 seconds. The actuation response and dynamic displacement characteristics during real time experiment is analyzed by applying a sequence of potential with the varying voltage, current with frequency for obtaining their actuation response. For this actuation analysis, loads of 25 g, 5 Volt voltage and 3 Amp current were used. The power supply with Lab view is interfaced. The maximum deflection of 2.4 mm, and 1.5 mm is calculated for multi cycles of heating and cooling.

In Lab view, program channel configuration for acquiring the actuation and configuration data for programmable power supply is done. The NiTi alloys based SMA shows stable actuation with the sufficient load carrying capacity. Electrical actuation and hot plate actuation shows difference in displacement due to non-uniform heating during joule heating. As compared to hot plate actuation, the heat loss is higher during electrical actuation because of higher temperature during electrical actuation. The higher temperature during electrical actuation attracts more heat loss. In addition, hot plate actuation was carried out without load, while a load of 25 g was present in electrical actuation, which resulted in lower shape recovery in electrical actuation. The difference in shape recovery for laser marked and without marked sample is shown in Fig 3.11 (e) and (f). The generated stress field can have an adverse effect on the process of detwinning [40]. This can be primarily due to a difference in the stress pattern between samples built with and without laser marking.

A certain amount of external work must be expended when a NiTi sample is subjected to plastic deformation. A small portion of this work is stored in the lattice as scored energy in the form of residual strain, resulting in a high density of lattice defects. Both the defects and the internal stresses can act as a negative factor to the movements of martensite interfaces. Thermally induced diffusion and annihilation of lattice defects occur when deformed metals are heated, and the accumulated energy is released in the form of heat. This may explain why the barrier stress for martensite reorientation has decreased and the damping capacity has increased [114].

Laser treatment can help to remove the potential existence of the stress field. Nevertheless, Laser treatment can also lead to precipitate formation, which can contribute to a

better recovery of the shape observed [118]. The increase in superelasticity compared to non-laser treated samples was attributed to the precipitation hardening effect caused by Ni_4Ti_3 precipitate formation during laser treatment on the deposited track. Ni_4Ti_3 precipitation has been related to the formation of the rhombohedral phase (R-phase) [114-118].A rise in shape recovery behavior will also be influenced by R phase grain refinement for the laser marked sample, which is shown in Fig 3.11 (e) and (f).

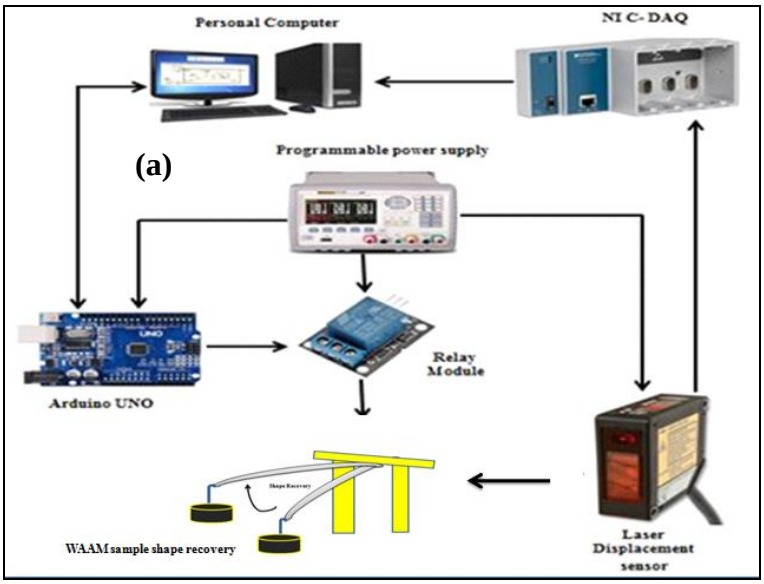

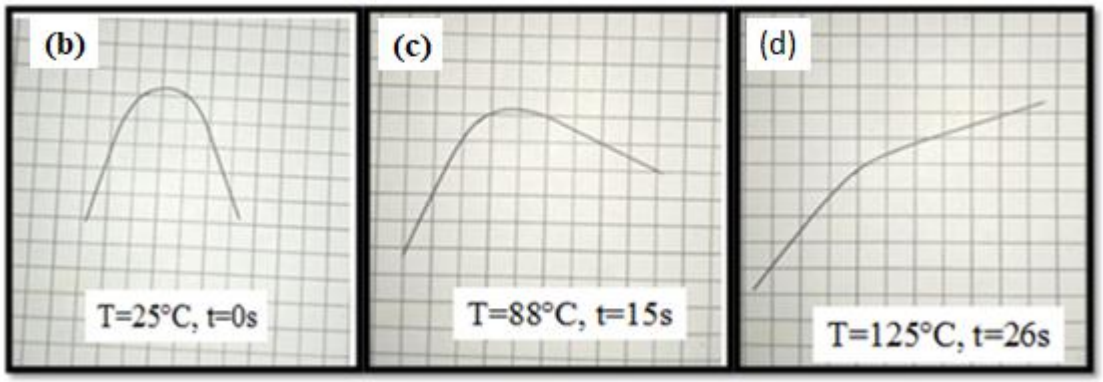

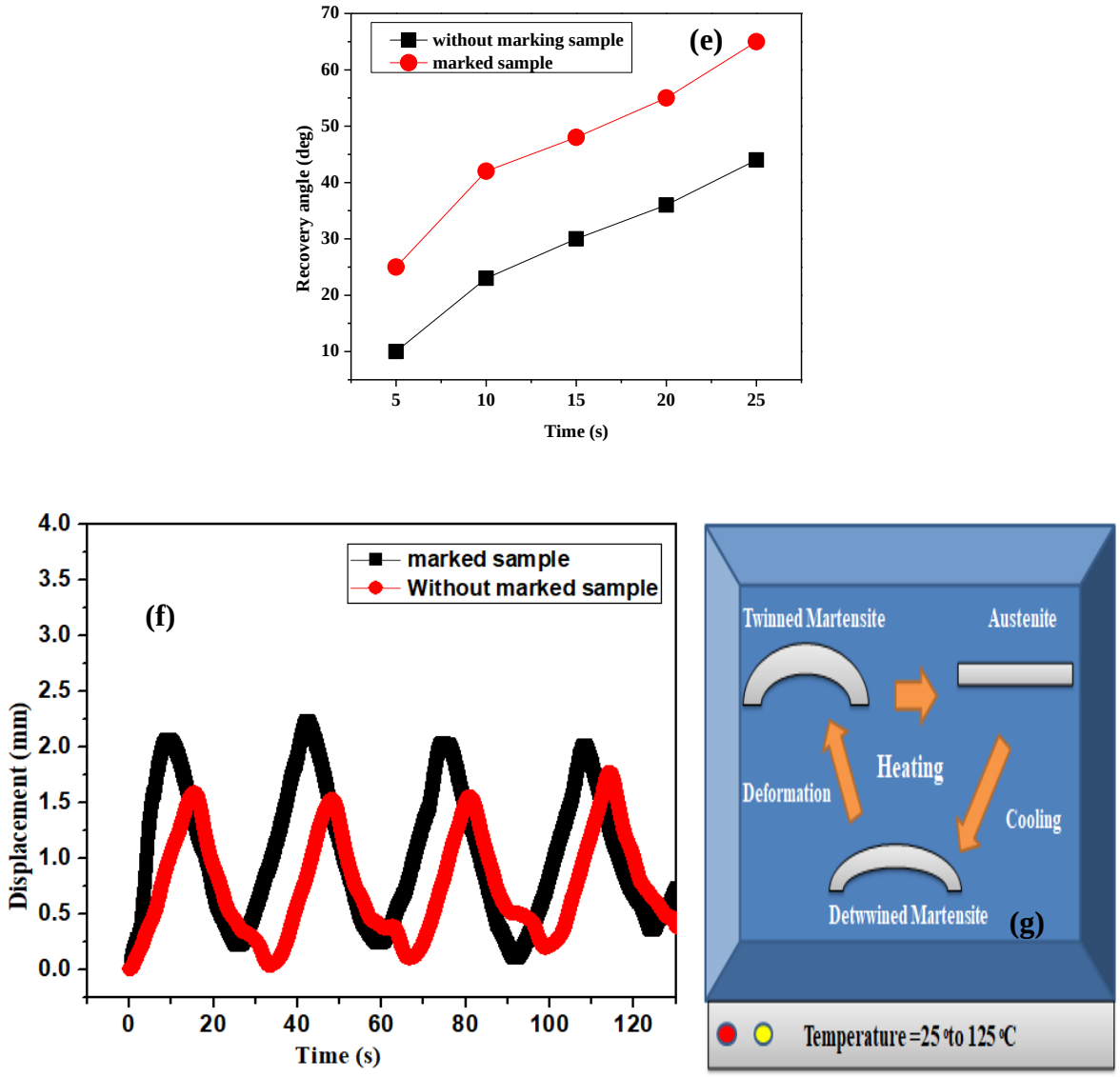

Fig. 3.11 (a) Schematic diagram of actuation behavior analysis, (b),(c),(d) Shape Recovery during hot plate actuation, (e) Recovery angle Vs. time graph, (f) Time vs. Displacement graph for WAAM samples and (g) Schematic of hot plate

3.2 Influence of Interlayer Delay

Multi-layer deposition causes heat accumulation during wire arc additive manufacturing, which rises the preheat temperature of the previously created layer. This leads to process instabilities, which result in deviations from the desired dimensions and mechanical properties changes. During wire arc additive manufacturing deposition of the wall structure, a systematic research is carried out by adjusting the interlayer delay from 10 to 30 seconds. Issues like melt-pool

instability, residual stress, distortions, and heat accumulation during the process are particularly important when constructing wall structures since the process works on the principle of depositing layer-by-layer. As the wall structures are built by laying single tracks one over the other, excessive heat accumulation takes place during the process. The heat accumulation increases the preheat temperature of the previously deposited layer during the multi-layer deposition.

As a result, the objective of this research is to investigate how varied interlayer delay periods impact the microstructure, shape memory properties and mechanical properties of a WAAM built NiTi-based SMA.

For interlayer delaye same material and experimental setup has been used which has been used in section 3.1.The WAAM deposition is carried out with different interlayer delays of 10 s, 20 s, and 30 s, respectively for six subsequent layers Excepting the change in the interlayer delay time, all other parameters were kept constant for all the six layers. Scanning speeds, voltages, feed rates, argon gas flow rates, and standoff distances for deposition are 8.57 mm/s, 17.5 V, 5.5 m/min, 20 l/min, and 15 mm, respectively. The deposition was performed in an open chamber and no specific cooling system was used for the WAAM deposition process. Other details about the WAAM system has been given in section 2.2.

3.2.1 Numerical Modelling

ABAQUS 6.20 software is used to perform 3D finite element simulations for thermal analysis of the WAAM process.

For the analysis, the following assumptions are taken into account.

- In the beginning, the boundary conditions are applied to the substrate material at ambient temperature (i.e. 298 K).
- For simplicity, the deposit's geometry is considered to stay constant throughout the process, and the surface is assumed to be completely flat.
- The effects of convection and radiation are taken into account.
- It is believed that deposition is isotropic and homogenous.

Temperature-dependent material properties are assumed, and their values are based on published reports [18-22]. The heat conduction equation (refer to equation 5) [119] is used to compute the temperature distribution.

$$\frac{\Delta Q}{\Delta t} = -k * A * \left(\frac{\Delta T}{\Delta x}\right) * \rho * C_p * \frac{\partial T}{\partial t} + \nabla.(k * \nabla T) = Q \quad (5)$$

Free convection boundary conditions are established on the bottom and top surfaces of the base plate, as well as on the vertical surfaces of the wall. According to literature correlations [120], the convection coefficients for the top surface of the base plate, the bottom surface, and the vertical surface of the wall are 8.5 W/m^2 K, 4 W/m^2 K, and 12 W/m^2 K, respectively. General radiation to the environment boundary condition is included, with the material emissivity set at 0.2 [120].

The heat loss q_{loss} from the building structure's surface due to convective heat transfer and radiation is taken into account. q_{loss} is calculated using the following equation [121].

$$q_{loss} = h(T-T_{room}) + \varepsilon\sigma\ k_b(T^4 - T^4_{room}) \quad (6)$$

The chosen mesh for the wall was made up of cubic pieces, as described in previous papers. In the bedplate, the mesh size is doubled in the X and Z axes to minimize computing time. Two models are used to compute the idle time provided during deposition: one for cooling and the other for heating (deposition) simulation. The heat source, which is employed only in the heating model, is the only difference between the two models in terms of material characteristics, mesh topology, and boundary conditions. At the end of the heating procedure, the deposition of the current layer is simulated without any idle time. The beginning circumstances for the cooling phase are determined by the end state of this simulation, which includes the initial temperature field and the active/inactive state of the elements. The initial value of the (T_{max}) variable determines the first element activation state. After then, the cooling simulation begins, modeling the workpiece's thermal behavior during the idle time following the deposition of the current layer. The defined idle time is then utilized as input for the new layer's heating simulation. This study's heat source model is a modified version of the double ellipsoid model [25], which has been adapted for the GMAW process. The heat distribution function is depicted in Equation 7:

$$q_b\ (x, y, z, t) = \frac{6*\sqrt{3}*Q*f_{f,r}}{a*b*c_{f,r}*\pi*\sqrt{\pi}} * e^{\left[-3*\left(\frac{x}{a}\right)^2 + \left(\frac{y}{b}\right)^2 + \left(\frac{\varepsilon}{c_{f,r}}\right)^2\right]} \quad (7)$$

The boundary conditions used for modelling heat sources are presented in equations 4 and 5.

$$q(x,y,z,t) = \begin{cases} q\_f \ for \ z \geq z0 \\ q\_r \ for \ z < z0 \end{cases} \quad (8)$$

$$\text{and, } \frac{ff}{cf} = \frac{fr}{cr} \text{ where } f_f + f_r = 2 \quad (9)$$

If equation 9 is met, the words $f_{f,r}$ are distribution factors with different values for the frontward and backward ellipsoids. The heat input of the welding process is divided into two power density contributions in the suggested heat source: the base metal (q_b) and the filler or deposited metal (q_w) (refer to equation 10)

$$q_w = \frac{Q}{V_{el}} \quad (10)$$

If the condition in equation 11 is met, the amount of power transmitted to both the base q_b and the filler metal q_w can be regulated, where η = 50% [106].

$$Q = q_b + q_w = \eta * I * V \ (W) \quad (11)$$

The temperature distribution results show that the measurement point is critical for heat distribution and correlations between energy input and actual temperatures. A molten pool's shape may vary due to the substantial increase in temperature. A change in the shape of a molten pool might cause the geometric shape of the deposited layer to deteriorate. As a result, the created model will be beneficial in the future for the development of a feedback control system for WAAM process temperature management.

3.2.2 Results and Discussion

3.2.2.1Thermal Analysis

Using finite element analysis, the influence of interlayer delay on the preheat temperature of the previously built layer during WAAM is studied. Fig. 3.12 depicts the average temperature distribution generated by the simulation. The impact of interlayer delay on the preheat temperature is shown in Fig. 3.12 for various values of interlayer delay determined by numerical simulation and pyrometer. Temperature was measured on top of the fabricated wall. The variations/differences are displayed as error bars. The maximum variation in the preheat temperature between experimental values and simulation is under 2%. A short interlayer delay time results in higher preheat temperature, which has a preheat effect on the deposition of the subsequence layers. Furthermore, as the deposition progresses from the bottom to the top layer,

the preheat temperature for a given delay time rises. This is mostly due to the substrate effect, which causes fast heat dissipation at the lower layers. As the deposition moves to the top layer, the heat accumulation increases, and the heat dissipation rate reduces.

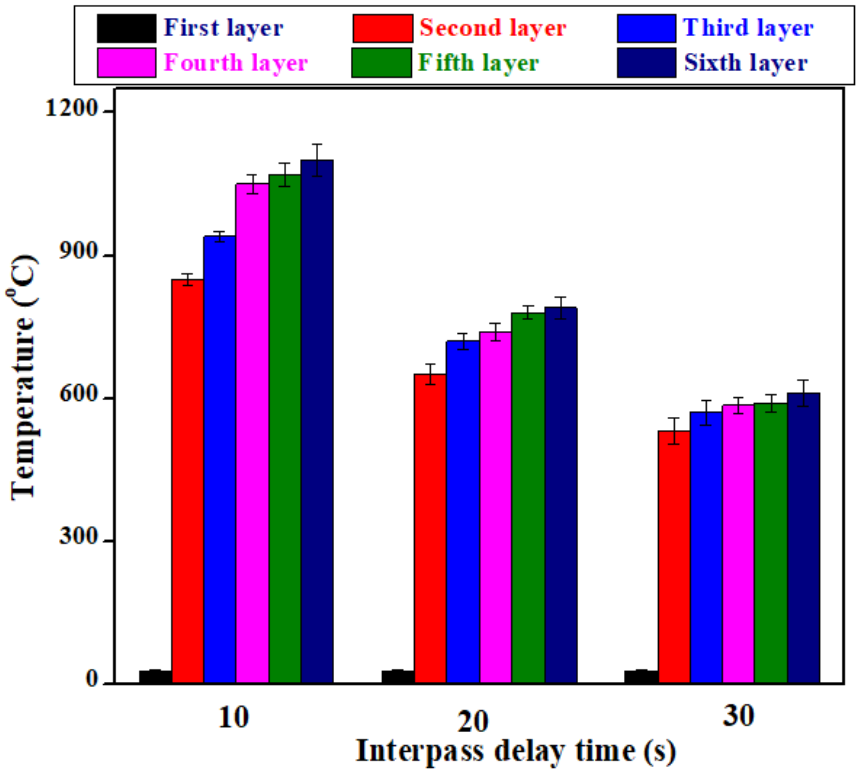

Fig 3.12 Temperature distribution profile observed in the WAAM samples according to the model

3.2.2.2 Geometrical Analysis

Fig. 3.13 (b-d) shows the 3D scan images of the WAAM structures deposited at different interlayer delay times. When the interlayer delay is increased from 10 to 20 s, the wall height increases by 23%. For instance, when the interlayer delay is increased from 20 s to 30 s, the wall height increased by 34% (Fig. 3.13 e). With an increase in interlayer delay from 10 s to 20 s and 20 s to 30 s, the reduction in wall width is observed to be 33% and 47%, respectively (Fig 3.13 f). Regarding Fig. (3.13), the increase in the deposit height and decrease in the deposit width with an increase in the interpass delay can be explained as follows: During the WAAM process, the deposited material experiences significant heating

and cooling cycles, which can affect the material's microstructure and mechanical properties. By increasing the interpass delay, the deposited layers have more time to cool, which can cause the deposited part to shrink in width due to thermal contraction. At the same time, the height of the part can increase due to the increased solidification time, which allows for more complete melting and bonding between adjacent layers.

This phenomenon can also be explained by considering the heat input during the WAAM process. When the weld pool is too hot, the molten metal tends to flow more easily, resulting in a wider deposit. However, when the temperature is lowered, the viscosity of the molten metal increases, causing it to flow less easily and resulting in a narrower deposit.

The viscosity of the molten metal is also influenced by the temperature, with higher temperatures leading to lower viscosity and easier flow.

Therefore, by increasing the Interpass delay, the temperature of the previously deposited layer has more time to dissipate, resulting in a decrease in the temperature of the new layer during deposition. This decrease in temperature can cause an increase in the viscosity of the molten metal, resulting in a narrower deposit. On the other hand, if the interpass delay is reduced, the temperature of the previous layer may still be too high, resulting in a wider deposit due to easier flow of the molten metal. Thus, at higher layers, the outward flow of the melt pool will be higher, which leads to larger widths. Cracks and depression are also observed at the lower interlayer delay due to the heat accumulation effect and residual stresses. 'Humping' and 'undercutting' can be caused by fluid movement inside the molten pool (as seen in Fig. 3.13 a) [110]. The Marangoni effect, also known as the thermocapillary effect, is a phenomenon in which fluid motion is regulated by variations in surface tension [112]. Because of the arc's oscillation frequency, ripples can be seen throughout the tracks [110], (as seen in Fig. 3.13 a).

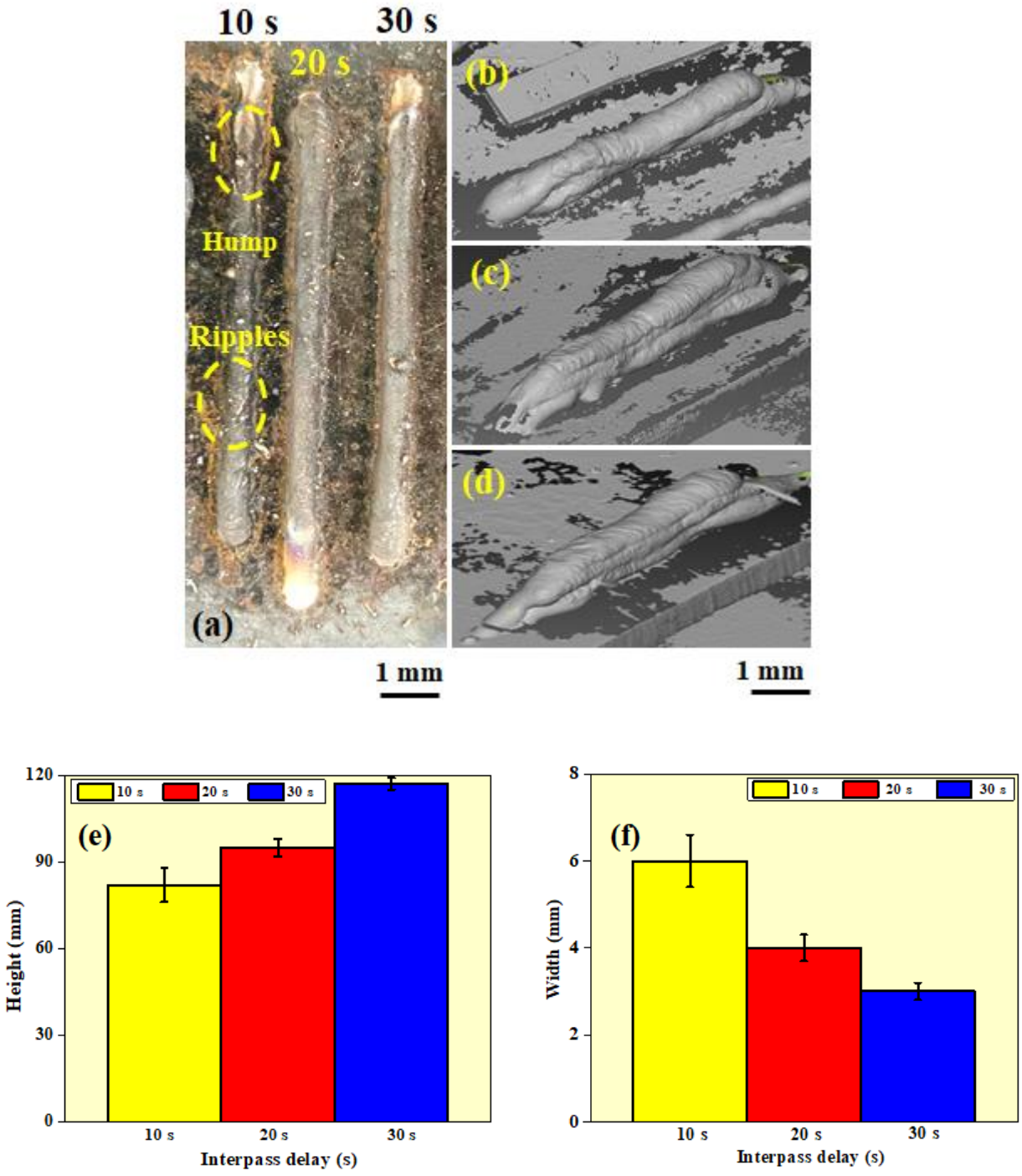

Fig. 3.13 WAAM deposited walls with different thermal delay periods and, laser scanning images of deposited walls with the interlayer delay periods of (b) 10 s, (c) 20 s and (d) 30 s, Effect of interlayer delay on the wall (e) height and (f) width in thw WAAM built NiTi-based walls.

3.2.2.3 Density Measurement and Metallurgical Characterization

The porosity of the NiTi wall structures built with different interlayer delay periods is analyzed using computer tomography. Fig. 3.14 (a-c) presents the 3D image of the sample indicating the presence of porosity. The average size of the pores is in the range of 304 µm, 150 µm, and 30 µm for walls built with 10 s, 20 s and 30 s interlayer delay, respectively. The variation in the size of the pores can be attributed to the increase in the temperature at the lower interlayer delay period that can lead to cracking in addition to the usual porosity. The density of the wall structures is 93%, 97%, and 99.8 % for walls built with the interlayer delay of 10 s, 20 s, and 30 s, respectively. It can be observed that when the interlayer delay increases, the density of the wall structures rises. This is due to the significant drop in melt pool temperature (increase in interlayer delay, reduces the peak melt pool temperature). The reduction in the melt pool temperature suppresses the vaporization of the material, which leads to a reduction in the porosity with an increase in interlayer delay. Furthermore, a reduction in melt pool turbulences combined with a rise in interlayer delay improves its density. The variation in porosity is partly a function of melt pool size and the variable degassing behavior during WAAM, according to the literature [74]. Larger weld pools combined with short welding periods result in different-sized solidification pores. The density is lower than the other counterparts because a large melt pool size is observed at the lower interlayer delay. The existence of much fewer hydrogen entrapment sites, such as grain boundaries, and the release of hydrogen into the environment by arc forces, might explain the lower porosity in the 30 s delay sample [122].

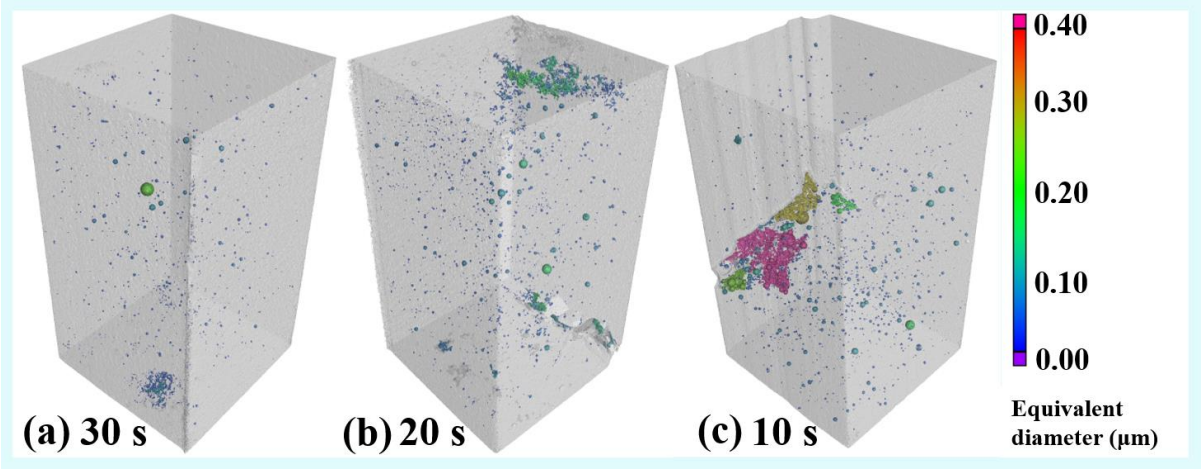

Fig. 3.14 Chotomography results for WAAM deposited interlayer delay (a) 30 s, (b) 20s and (c) 10s

Fig. 3.15 (a-c) presents the microstructural images obtained using SEM for the WAAM built NiTi walls. It shows that walls built with higher interlayer delay show finer grains in comparison to lower interlayer delay samples [6,26]. This is mainly due to the higher solidification rate and subsequent formation of fine grain structure for walls built with higher interlayer delay. Fig. 3.15(a) shows the schematics of grain growth for the different interlayer delay periods. Impressively, slower solidification in 10 s resulted in larger grains (54% larger in size) than walls built with 30 s delay. In addition, dendrites also serve as nucleation sites for pores during solidification (as shown in Fig. 3.15. The higher porosity in the sample with a 10 s interlayer delay can be attributed to the existence of a larger grain boundary area and the availability of appropriate interdendritic spaces. The liquid metal gets undercooled as the temperature difference from the bottom to the top of the molten pool decreases, causing the solidification front of the columnar grains to destabilize [123]. The columnar to equiaxed transition (seen in Fig. 3.16) may occur when deposition progresses from bottom to top layers, as the temperature gradient decreases and the interface movement velocity increases. The SEM elemental mapping findings of WAAM deposited tracks for samples with an interlayer delay of 10 s, 20 s, and 30 s are shown in Fig. 3.17. Distinct spectrums containing different Ti and Ni-rich areas are observed. Oxides layers are visible in samples generated with a 10 s and 20 s interlayer delay, compared to a 30 s sample, due to the lower cooling rate. At high temperatures, Ti may react with atmospheric oxygen and for walls built with 10s and 20 s interlayer delay, interlayer preheat

temperature is high. Inner oxides are similarly multilayered, with complicated and non-uniform compositions. Oxides in the WAAM structure can cause structural and elemental discontinuity. The waviness of the oxidized surface cause's arc length variation and, as a result, arc voltage fluctuation. Oxides have different electron emission capabilities than the matrix, and the waviness of the oxidized surface cause's arc length variation and, as a result, arc voltage fluctuation. Because of their higher melting temperature and lower density than the matrix, oxides will float on the surface of the weld pool. When the weld pool encounters a large oxide island, it flows through it, changing the wetting boundary to an uneven curve until the island is completely passed.

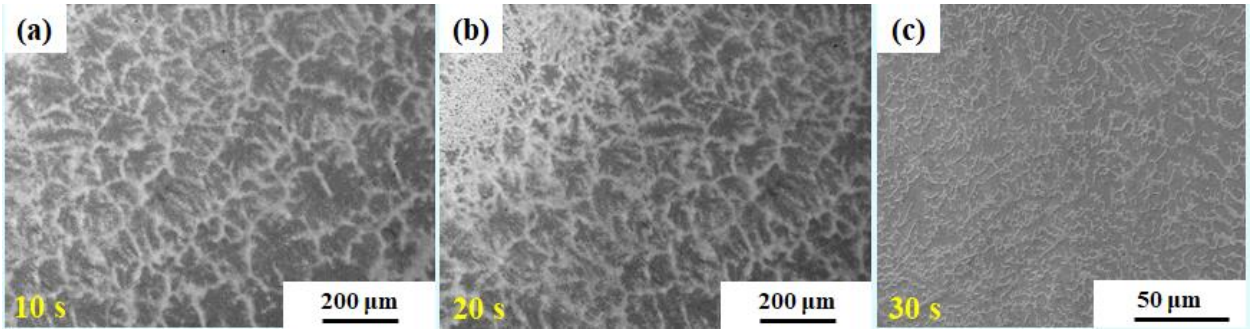

Fig. 3.15 Scanning electron microscopy images of the WAAM built NiTi samples with an interlayer delay of (a) 10 s, (b) 20 s, and (c) 30 s.

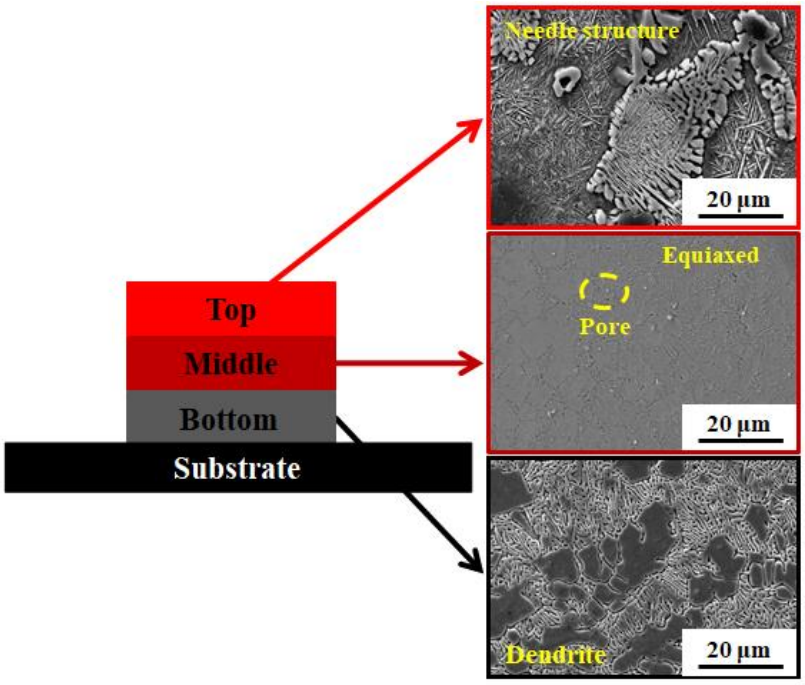

Fig. 3.16 Schematics illustrating the melt pool characteristics and their grain growth

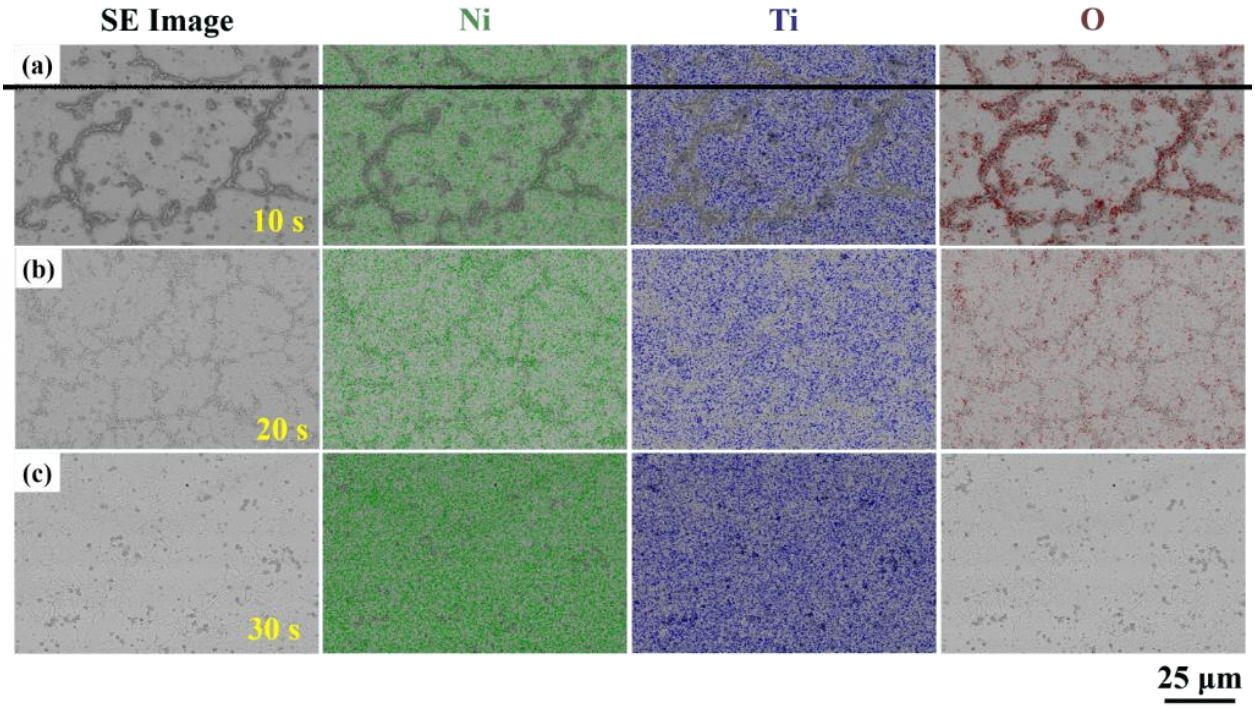

Fig.3.17 Elemental Mapping of the WAAM built NiTi samples as a function of interlayer delay (a) 10 s, (b) 20 s, and (c) 30 s

The XRD patterns of NiTi deposited walls as a function of different interlayer delay periods is presented in Fig. 3.18(a, b). The existence of the B2 phase is revealed by the high-intensity martensitic peak at 44.38° and 64.7° along the planes (020) and (200). The creation of Ni_4Ti_3 may be seen at 78.81°, which corresponds to (110). The change in the temperature history during deposition has a major impact on phase evolution, resulting in a distinct anisotropic microstructure. The two-way shape memory effect in NiTi is increased due to the presence of Ni_4Ti_3. The Ni_4Ti_3 precipitates, in general, lead to the R phase transformation [124]. The estimated value of crystallite size is 37± 10 nm, 14 ±6 nm, and 7±5 nm for walls built with 10 s, 20 s, and 30 s delay, respectively. The crystallite size reduces with an increase in interlayer delay, which is evident from the broadening of the peak. A shift in the peak position is also observed (refer to Fig. 3.18 b) with variation in the interlayer delay, which is primarily due to variations in the thermal strain as per the Braggs law [125].

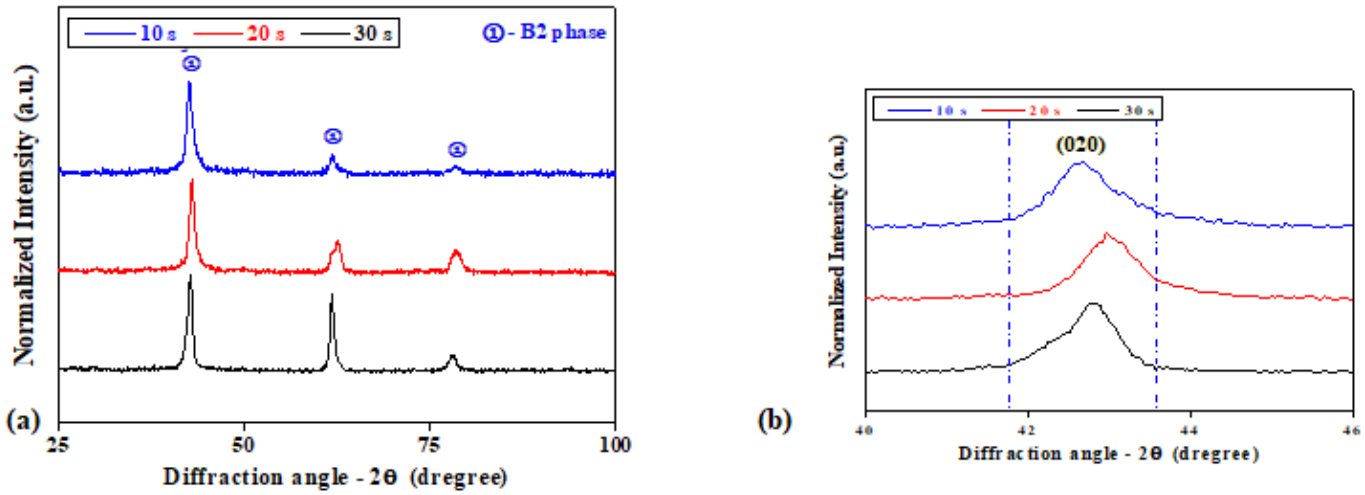

Fig. 3.18 X-ray diffraction patterns of the WAAM built NiTi walls as a function of (a) different interlayer delay periods and (b) the plot showing the peak shift observed for the highest intense peaks.

3.2.2.3 Phase transformation results

Fig. 3.19 (a-c) displays the effect of the interlayer delay on the trend of DSC curves. The reason for this behavior is due to the existence of high nickel in the matrix which prevents martensitic transformation. By increasing Interlayer delay, the intensity peaks of A→R transformation increased significantly compared to the lower interlayer delayer. The internal strain due to the formation of Ni_4Ti_3 precipitates and high nickel content of the matrix inhibited the formation of M phase. Phase transformation temperatures are changed by alternation of the stress levels.

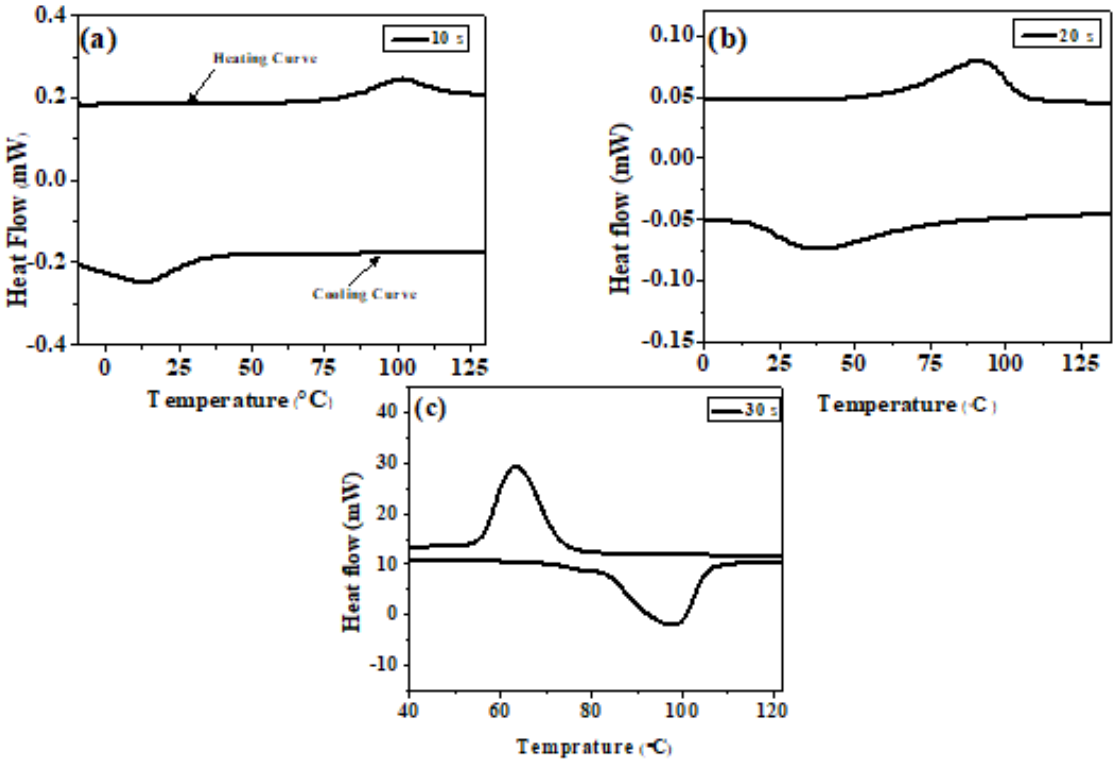

Fig. 3.19 DSC curves for (a) 10 s, (b) 20 s, and (c) 30 s

3.2.2.5 Mechanical properties

The microhardness distribution of NiTi samples generated under various interlayer delay periods is depicted in Fig.3.20 along the vertical centerline of the cross-section. Higher hardness is observed for the bottom layer, owing to higher cooling rates and finer grain structure as a result of increased heat flow to the substrate. Because of the comparatively small grains at the higher interlayer delay, the average hardness values vary when the interlayer delay is raised from 10 to 30 s. The interlayer delay causes hardness variation due to the development of distinct phases (Ni-rich phases). The hardness of WAAM-fabricated NiTi is largely regulated by solid solution and grain boundaries or dislocation distribution due to some segregated components interacting between grain boundaries and edge dislocations [126]. With a larger interlayer delay, the deposit cools faster, resulting in more grain boundaries and dislocations, leading to higher micro-hardness values [126]. The compression characteristics of walls deposited at various interlayer delays are shown in Fig. 3.21. Because of the collective effects of oxidation behavior and grain size, increasing interlayer delay results in a substantial increase in compressive strength. The

strength of 30 s samples is increased due to grain refinement, decreased porosity, and the formation of a Ni-rich phase [126-127].

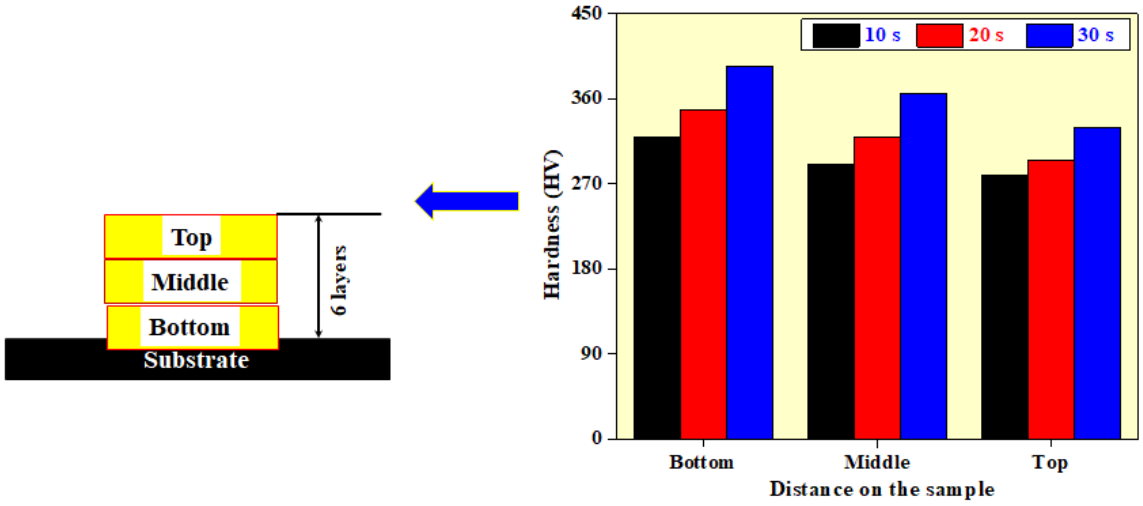

Fig. 3.20 (a) Vickers hardness measurements observed for the WAAM built NiTi samples observed as function of the sample position, and (b) Compression behaviour of the WAAM built NiTi walls as a function of interpass delay.

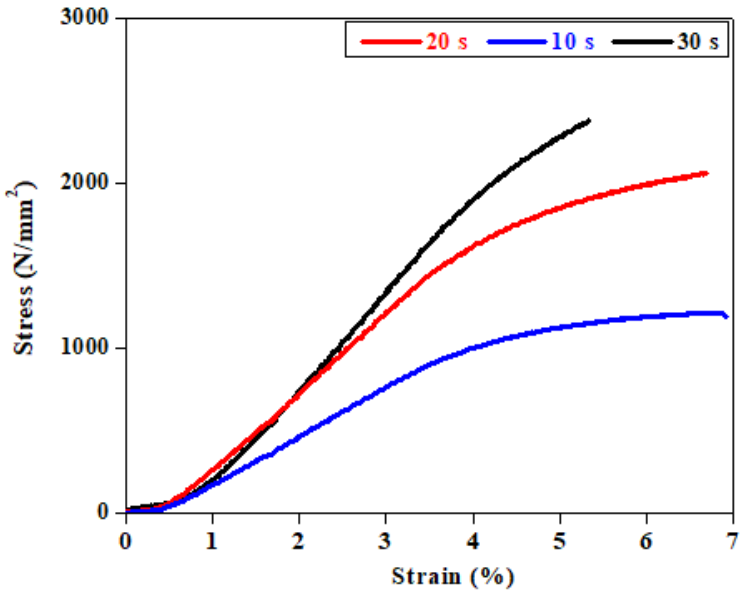

Fig.3.21 Compression behaviour of the WAAM built NiTi walls as a function of interpass delay.

3.2.2.6 Shape Recovery Studies

The effect of interpass delay on the shape recovery behavior of NiTi shape memory alloy fabricated through wire and arc additive manufacturing (WAAM) has been investigated. It has been observed that the interpass delay significantly affects the shape recovery behavior of NiTi alloys. Figure 3.22(a) shows that the maximum deflection observed for 30 s, 20 s, and 10 s delays were 3.2 mm, 2.2 mm, and 1.68 mm, respectively. If the inter pass delay is too short, the deposited layers may not have enough time to cool down to the ambient temperature before the next layer is deposited. This can result in a temperature gradient across the material, with the outer layers cooling more rapidly than the inner layers. This can lead to residual stresses in the material, which can affect its shape recovery. Residual stresses can arise due to differential cooling rates between the deposited layers, which can cause thermal expansion and contraction in the material. The magnitude and distribution of these residual stresses depend on the thermal history of the material, which is influenced by the inter pass delay. If the inter pass delay is too short, the temperature of the previously deposited layer may still be high when the next layer is added, leading to increased residual stresses in the material.On the other hand, if the inter pass delay is too long, the material may have cooled down completely, resulting in poor bonding between the layers. This can lead to reduced adhesion between the layers, which can affect the shape recoveryThis variation in deflection could be attributed to the differences in the stress pattern between samples prepared with different interpass delays, which can negatively impact the detwinning process. However, using different delay approaches, it is possible to eliminate the stress field and facilitate precipitate development, which can aid in the recovery of the observed shape.

Furthermore, it has been observed that for higher interlayer delays, the R phase and grain refinement will influence a rise in shape recovery behavior. The Ni-rich phase has a rhombohedral structure and is useful for altering the matrix Ni content, thereby improving shape memory properties by increasing the critical stress for slip [127-129]. Figure 3.22(b) shows that the bending angle change for temperature as a function of interlayer delay. Electrical actuation leads to free recovery (without load) and less heat loss as compared to increased recovery during hot plate actuation. When compared to near-equiatomic NiTi alloys, Ni-rich NiTi alloys with more than 50.5 at.% Ni exhibit a wider range of transformation temperatures and have higher

thermo-mechanical cycle stability. However, the formation of coherent and semi-coherent Ni4Ti3 during intermediate aging temperatures of 300 to 500°C can affect the shape memory properties [126-129].

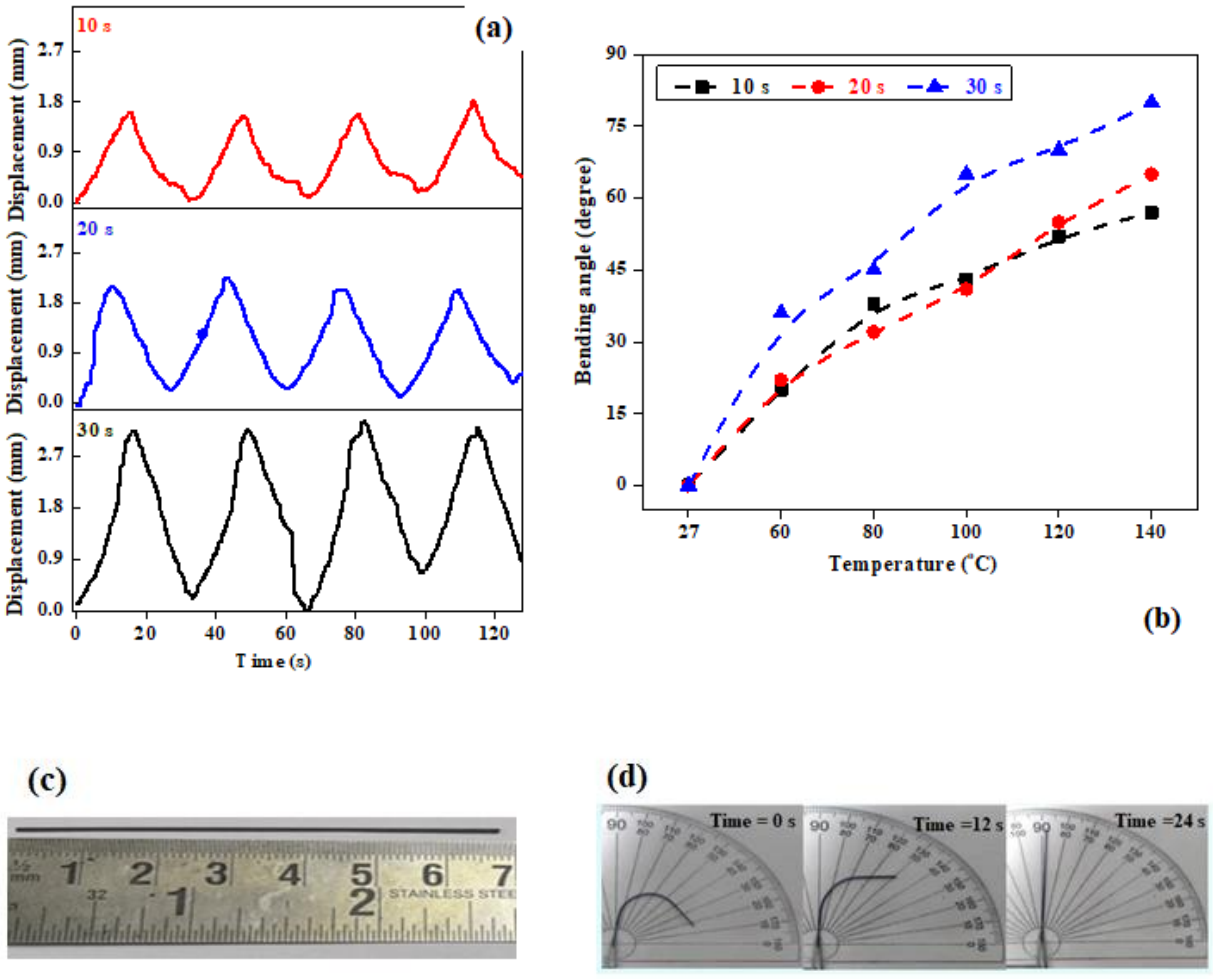

Fig. 3.22 (a) Time vs. Displacement graph for the WAAM built NiTi samples as a function of interpass delay, (b) Recovery angle vs. time graph. (c) image of the actuation sample, and (d) shape recovery during hot plate actuation, and their respective.

3.3 Influence of the Interpass Temperature

Shape memory alloy is a kind of alloy material with excellent mechanical properties such as shape memory effect and superelasticity. However, fabricating customized SMA based structures are crucial and challenging for specific device requirements using conventional manufacturing. The above issues can be addressed using advanced manufacturing techniques, like - Wire Arc

Additive Manufacturing (WAAM) technique. However, fabrication of the wall structures with controlled geometry using WAAM is technically challenging due to melt-pool instability, residual stress, and distortion during fabrication of shape memory alloy. A deposition parameter combination is found that optimizes the quality of single-track wall benchmark components made from NiTi. The aim of this study is to find the relationship between interlayer temperature and process duration and to determine the influence of the interlayer temperature on product structure and other properties.

More information regarding the system and the process can be found elsewhere (section 3.1.1). The WAAM deposition is carried out with different Interpass temperature 200° C, 400° C, and one sample without interpass temperature control for five subsequent layers. The density, geometry, microstructural characteristics, mechanical properties, and actuation behavior of the produced samples are thoroughly examined.

3.3.1 Result and discussion

3.3.1.1 Height and width measurement

After parameter optimization multi-layer samples has been deposited at the optimized parameter with interpass temperature control and in this experiment three samples has been prepared sample one is without intepass control , second one with 200 ° C and third one 400 ° C. For sample 2 and 3 preheating has been used to maintain the constant temperature thoughout all layers. The purpose of controlling preheating temperature and interpass temperature is to control the welding cooling rate while it has little influence on the time stay over homogenizing temperatures. Firstly, caused by the high deposition energy and temperature, the uneven temperature field on supporting substrate and built up layers would cause inevitable weld induced residual stress and distortions [53]. Raising interpass temperature would prolong the premature solidification and thus improve the wettability of molten metal. Cold cracking can lso be avoided with the help of unterpass temperature control. With interpass temperature control heat accumulation can also minimized, since an increased interpass temperature causes delayed solidification of the melt pool, resulting in a reduced deposit height and increased width. Fig.3.23 shows height and width and height of all three samples. Moreover, the increased interpass temperature can cause the deposited layer to have a lower viscosity, which can lead to a reduced

height. This can happen because the material has a lower resistance to flow when it is in a liquid state, and as a result, it can spread out more easily, reducing the height of the deposited layer. However, it should be noted that there is an optimum interpass temperature range for achieving the desired deposition geometry, as excessively high interpass temperatures can cause excessive distortion and porosity, while excessively low interpass temperatures can lead to incomplete fusion and reduced strength. The decrease in wall width with an increase in interlayer delay is mostly attributable to the decrease in the melt pool size and subsequent melt outward flow owing to a decrease in preheat temperature. The viscosity of the molten metal decreases as the deposition progresses from lower to higher layers owing to a rise in preheat temperature (according to the negative connection between temperature and material viscosity), causing an increase in the wall width at a higher layer. When too high an interpass temperature is used, the layer width will gradually increase. By setting a reasonable interpass temperature, layer width could be maintained similar because the excessive heat is extracted from molten pool to substrate while the temperature gradient and the cooling rate of the deposited part increased, resulting in improved surface quality and a reduction in total height difference As the interpass temperature is reduced, there is also an increased deposition defect in the near-substrate zone at bottom left (the side where the Fe wire is fed into the weld pool). The reason for this is thought to be the following: At lower interpass temperature, the molten pool during deposition of the first few layers is smaller, due to greater heat conduction into the substrate that is driven by the temperature difference between weld pool and substrate. When the interpass temperature increased from 200° C to 400° C, the wall height decreases by 20%. For instance, when the interpass temperature is increased from 200°C to WITC, the wall height reduces by 48%. With an increase in interpass temperature from 200 ° C to 400 ° C and higher temperature for without interpass temperature control sample, the reduction in wall width is observed to be 46% and 22 %, respectively.

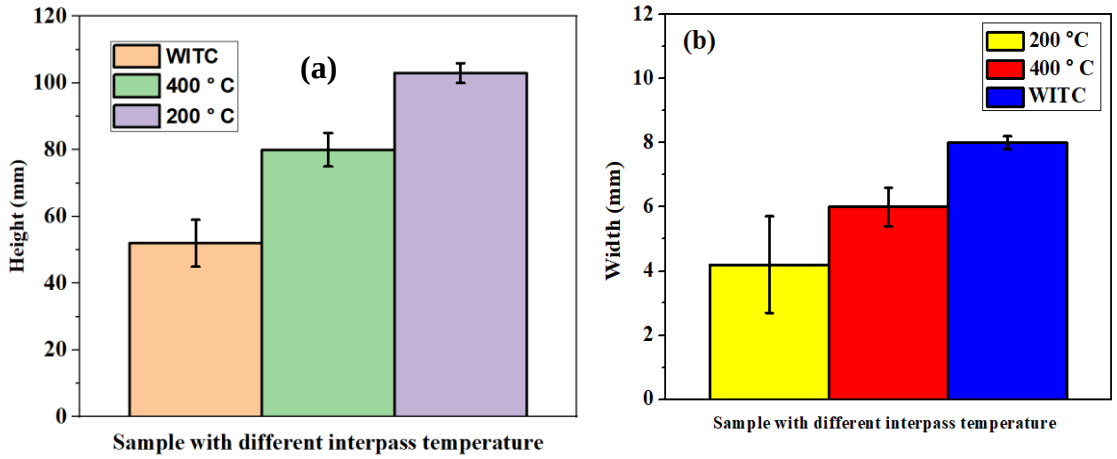

Fig. 3.23 (a) Height and (b) Width for different interpass temperature

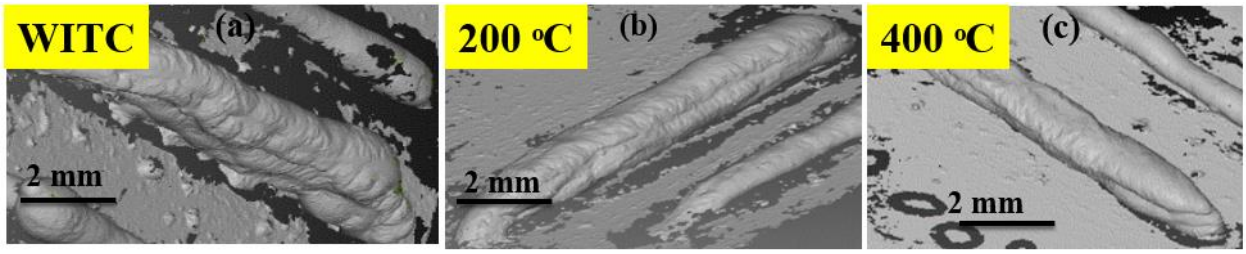

Fig.3.24 Laser scanning images of deposited walls with the interlayer delay periods of (a) WITC, (c) 200 C° and (d) 400° C

3.3.1.2 Density measurement and porosity analysis

The samples prepared with different interpass temperatures were studied for the distribution of pores with the help of computed tomography radiography (CT radiography) technique (Fig.3.25). A WAAM sample produced with lower interpass temperature revealed less porosity than the sample prepared with higher interpass temperature. Fig. 3.25 (a-c) presents tomogrphy image of the sample indicating the presence of porosity. The average size of the pores is in the range of 150 µm, 210 µm, and 30 µm for walls built with 400 °C, WITC, and 200°C interpass temperature, respectively.

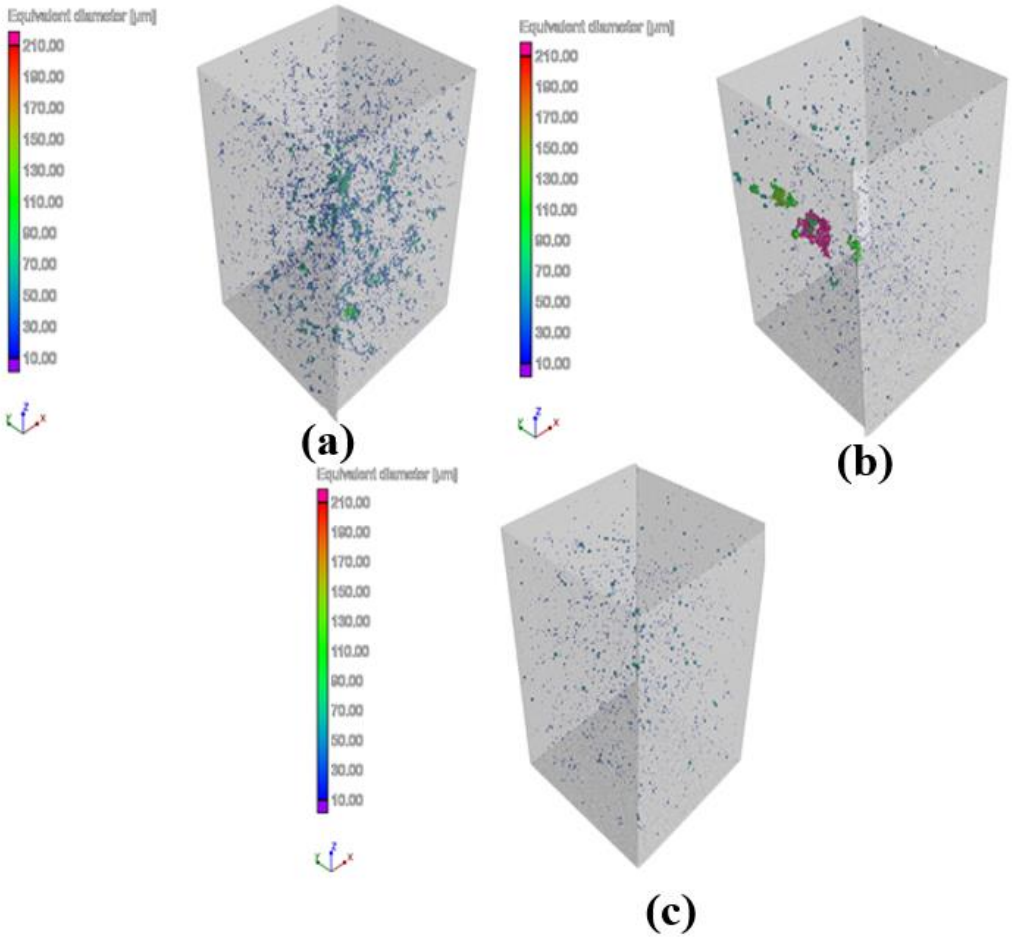

Fig. 3.25 Computer tomography (CT) scan images of the WAAM built NiTi walls structures as a function of Tempertaure (a)400 °C , (b) WITC and (c) 200 °C

The different solidification rates believed to have influence on the hydrogen evolution mechanism. Cyclic high temperature exposure of the sample for longer time may have supported coalescence of small pores in lower interpass temperature sample. Floatation of pores from layer-by-layer and longer exposure of liquid metal to the air due to slower solidification could be the probable reason for the presence of increased porosity at the top layer in higher interpass sample. The density of the wall structures is 94%, 97%, and 99.6 % for walls built with the interlayer delay of WITC sample, 400 °C, and 200°C, respectively. The reduction in the melt pool temperature suppresses the vaporization of the material, which leads to a reduction in the porosity

3.3.1.3 Morphology Analysis

The microstructural images for the NiTi walls made by WAAM are shown in Fig. 3.26 (a-c). The size of the grain and the density of the dentrites will alter as the interpass temperature rises. It demonstrates that walls constructed with a higher interlayer delay have finer grains when compared to samples with a lower interlayer delay [6, 26]. There are fewer dendrites and interdendritic structure at higher interpass temperatures (as shown in Fig. 3.26 a, c). The amount of Ni-rich phases will increase as the interpass temperature rises, but at a higher interpass temperature (400 ºC), Ti-rich phases in form of dendrites will also form (confirmed with EDS and XRD results) because Ti will play a larger role in phase formation at higher temperatures, even though Ti will also react with atmospheric oxygen to form oxides. SEM observation has been permformed for middle portion of the fabricated wall and mostly grains with few dendrite was formed all over the wall but amountof grains and dendrite varied.

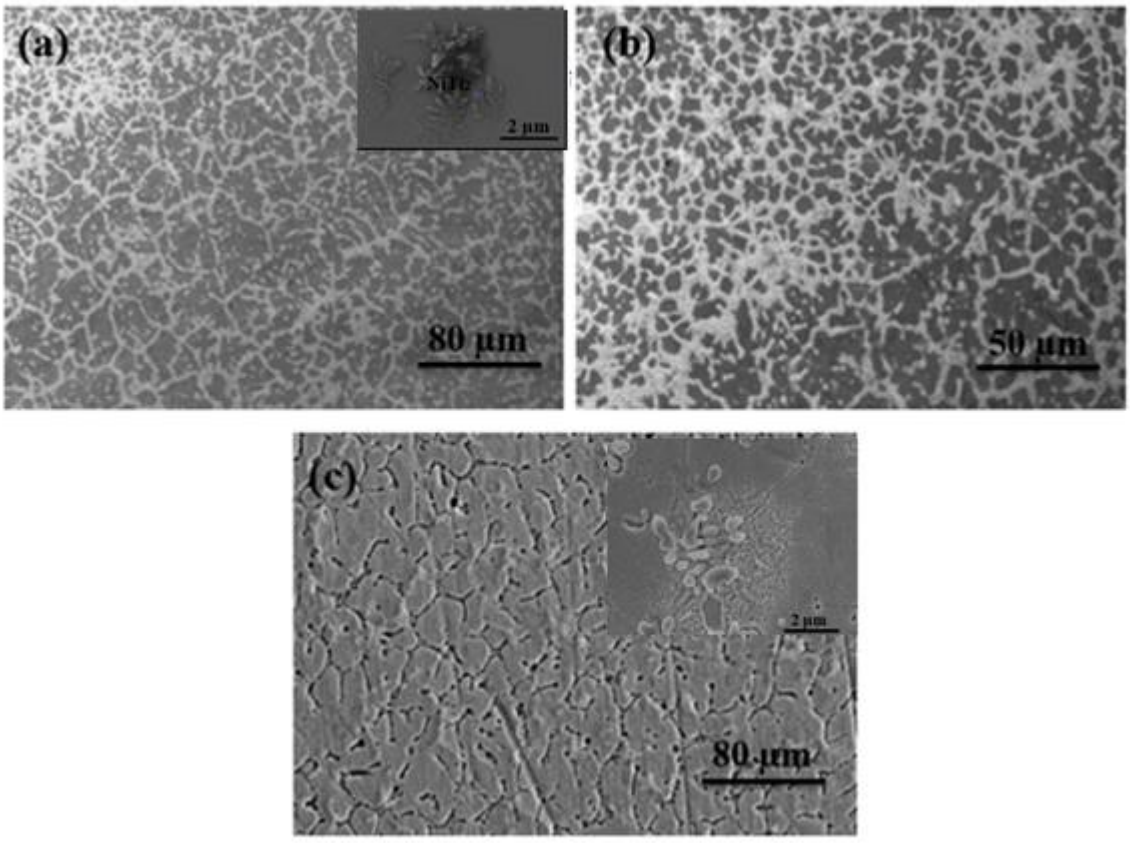

Fig.3.26 SEM image (a) WITC, (b) 200 °C and (c) 400 °C

3.3.1.4 XRD analysis

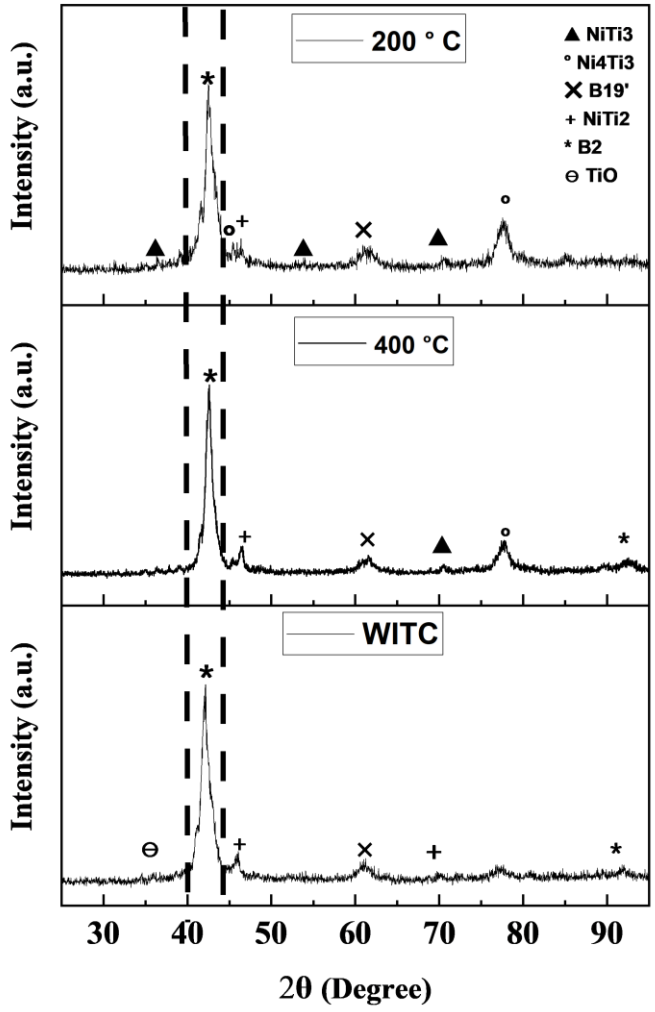

Fig .3.27 Xrd Analysis for different interpass temperature control sample

Fig. 3.27 shows the X-ray pattern obtained from the different interdelay sample. The highest peak observed at 43.1° and corresponds to the austenite B2 phase (high temperature state of NiTi phase). The other small peaks represents B19', $NiTi_3$, $NiTi_2$ and Ni_3Ti_4. A small amount of TiO has been also formed without interpass control sample because at higher temperatures titanium will react to atmospheric oxygen and form oxides. At higher temperature, Ti rich phase will form

due to high reactivity of Ti at higher temperature. The change in the temperature history during deposition has a major impact on phase evolution, resulting in a distinct anisotropic microstructure [124]. The two-way shape memory effect in NiTi is increased due to the presence of $NiTi_3$ and Ni_4Ti_3 which is shown by actuation results (will be discussed in section 3.3.6.1). The Ni_4Ti_3 precipitates, in general, lead to the R phase transformation (Rhombohedral which will enhance shape recovery behavior)[33-34] . The estimated value of crystallite size is 10±3 nm, 7±6 nm, and 5±4 nm for walls built without interpass control, 400 ° C, and 200° C, respectively. A shift in the peak position is also observed (refer to Fig. 3.27) with variation in the interpass temperature, which is primarily due to variations in the thermal strain as per the Braggs law [124-125].

3.3.1.5 Mechanical testing

The microhardness distribution of NiTi samples generated under various interlayer delay periods is depicted in Fig.3.28 along the vertical centerline of the cross-section. Higher hardness is observed for the bottom layer, owing to higher cooling rates and finer grain structure as a result of increased heat flow to the substrate. Because of the comparatively small grains at the lower interpass temperature, the average hardness values vary when the interpass temperature is raised from without interpass control sample to 400º C. The interpass temperature causes hardness variation due to the development of distinct phases (Ni-rich phases). The hardness of WAAM-fabricated NiTi is largely regulated by solid solution and grain boundaries or dislocation distribution due to some segregated components interacting between grain boundaries and edge dislocations [31]. Lower interpass temperature generates higher hardness because it cools faster than higher interpass temperature sample and resulting in more grain boundaries and dislocations [31]. Besides, since increasing Ni in NiTi composition results in increased hardness and brittleness in Vicker's hardness of Ni–Ti system intermetallic compounds decrease in the following order: Ni3Ti > B2 NiTi > B19' NiTi > NiTi2, and Ni3Ti has the largest elastic moduli and hardness. Fig.3.28 shows tensile graphs for different interpass sample. It has been observed that lower interpass temperature sample shows higher tensile strength due to Ni rich phase which

will increase ductility of WAAM deposited sample. Because of the collective effects of oxidation behavior and grain size, increasing interlayer delay results in a substantial increase in tensile strength (Fig.3.29). The strength of lower interpass temperature samples is increased due to grain refinement, decreased porosity and cracking susceptibility (due to cold cracking in without interpasss temperature sample) [114-118].

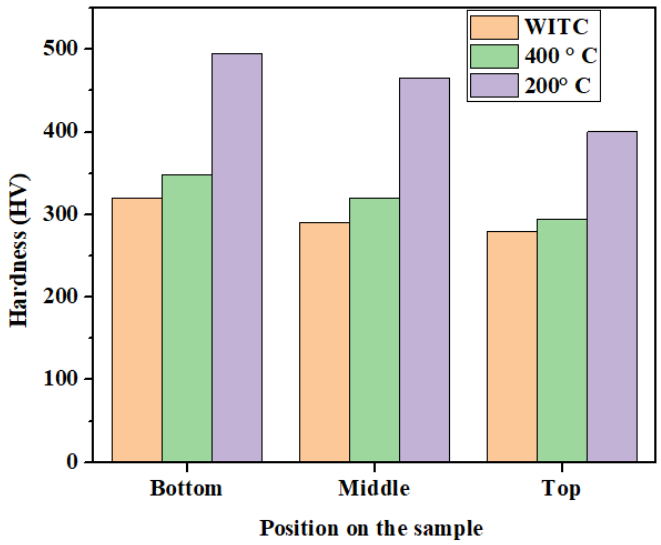

Fig.3.28 Hardness results for different interpass temperature

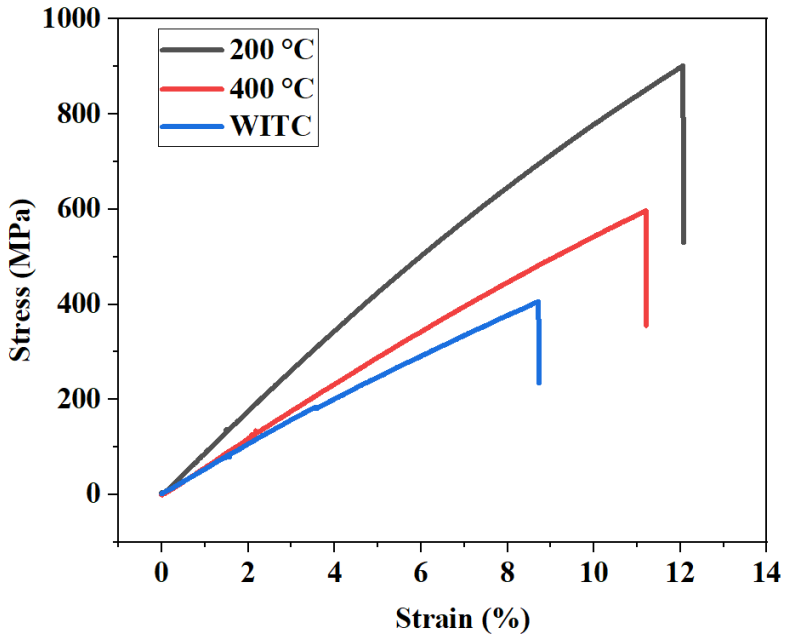

Fig.3.29 Tensile sample for different interpass temperature sample

3.3.1.6 Actuation studies

Electrical Actuation analysis has been conducted for the evaluation of thermal actuation as mentioned in Fig. 3.30. Same parameter and set up has been used which is mention in section 3.1.4.3. The martensite reorientation and plastic deformation in the NiTi WAAM sample occurs during preliminary deformation of the NiTi sample (bending around mandrel. Following cooling under this stress, the detwinned martensite form increased strain and relaxation of tension. A Martensite detwinning and plastic strain occurred in the samples after preliminary deformation to 35% in the martensite stage. The two-way shape memory effect (TWSME) is usually generated as plastic strain causes the formation of oriented internal stress. Such decrement in shape recovery may be attributed to the variation in the stress pattern between the samples made as a function of different interpass temperature. The resulting stress field may have a negative impact on the detwinning process [33-34].$NiTi_3$and Ni_4Ti_3 volume percentage was high in sample which has been fabricated at 200 °C and due to which it shows higher bending angle change. Along with Ni rich phases grain size variation and residual stress variation can also be the reason in higher bending angle change for lower interpass temperature [126-127].

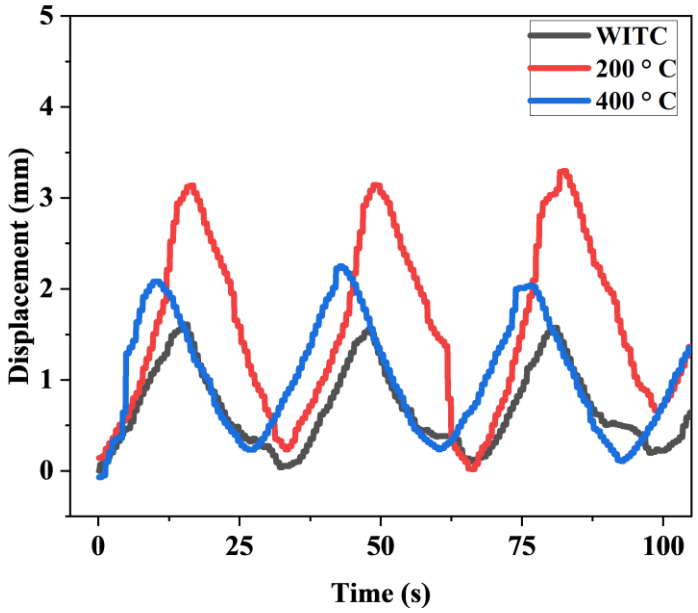

Fig.3.30 Actuation results for different interpass temperarure control sample

3.4 Porous Structure Fabrication

3.4.1 Porous Structure fabrication through WAAM

WAAM technology has a lower accuracy respect to the powder based techniques (±0.2 mm against ±0.04 mm) [4], and cannot be used to produce very complex parts (such as molds with internal cooling). However, it is suitable for the production of very large parts (up to meters) with medium complexity (e.g. stiffened aeronautical panels). The use of WAAM technology can allow for a huge reduction in Buy to Fly Ratio (BTF) making this technology very attractive for the aerospace industry [134-137]. The traditional approach for aerospace parts is to use machining operations that implies the use of a rough from which the most of the material must be removed. Especially when using high cost material, this could lead to large economic impact on the overall production [137-144]. But till now WAAM has been used to fabricate single track, and multi-layer sample of NiTi only which has been explained in Chapter 2.Present work focus on developing thin section first through a strategy in which first parameter has been optimized secondly different issues related to WAAM has been solved with the help of roughness reduction for better wettability of molten pool and also with the help of Interlayer delay, interpass temperature control etc. Fig.3.31 shows different attempts regarding complex porous structure fabrication in firstly failure samples has been given in which there is no process control strategy was used and it includes spatter, depression, insufficient wire deposition at start and end of closed section and bulges at the start and ending point. Due to high heat accumulation effect wrapping effect (delamination), fluid flow within the molten pool can cause the 'humping' and 'undercutting'. Ripples are also present throughout the tracks due to the oscillation frequency of the arc. Fig.3.31 shows challenging issues related to porous structure fabrication. Starting and and ending point of a close section like cavity and bulges.

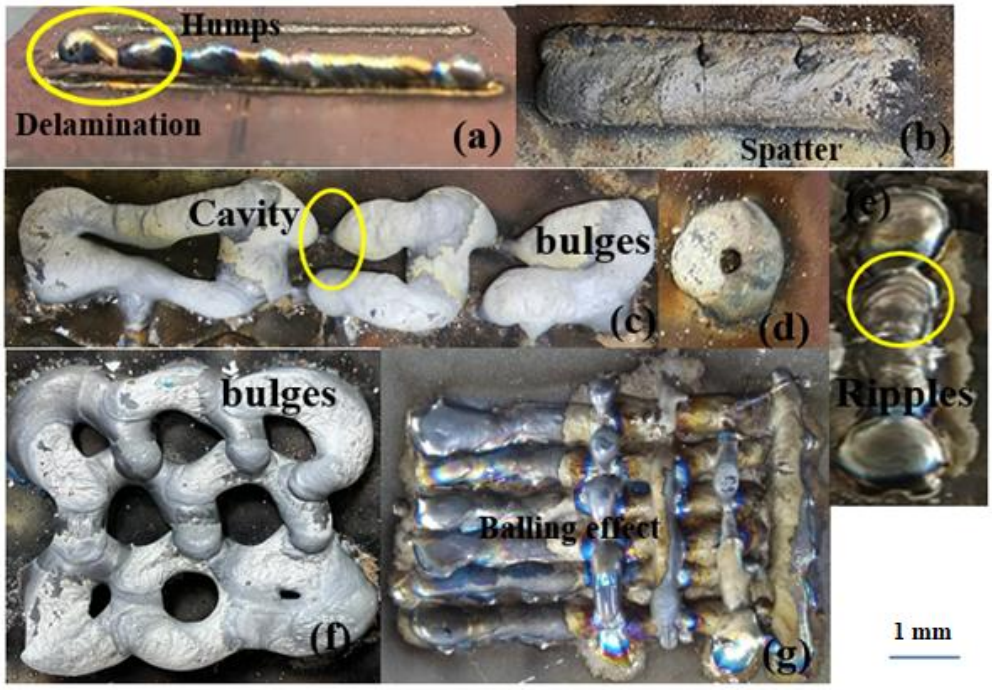

Fig 3.31 WAAM deposed sample which is showing (a) humps and delamination, (b) Spatter (c) unfilled cavity, (d) slumping (e) ripples, (f) bulges and (g) balling effect

With the use of roughness reduction of substrate can change wettability of molten pool. Preheating was also used for temperature gradient minimization that will be helpful in residual stress and width reduction, interpass temperature control has been also maintained by giving proper dwell of each cell as well as in between two subsequent layer. Details about interpass temperature and interlayer delay has been given in Table 6 .Each cell size, was also optimized and minimum width with uniformity and with minimum pore size has been also investigated during this research for the very first time for NiTi sample (Fig.3.32).Obtained measurement of all the obtained features of porous structure has been given in the following table. Three porous structure has been fabricated through WAAM. First one is Simple cubic Lattice and second one is honeycomb structure and minimum pore size was obtained around 2-3 mm and struct size was 2-2.5 mm and in initial trial so many issues occurs like maintain uniform width and pores was challenging. Bulges was observed at starting and end point which has been solved by varying wire feed rate and arc length variation at the start and end point of cell.

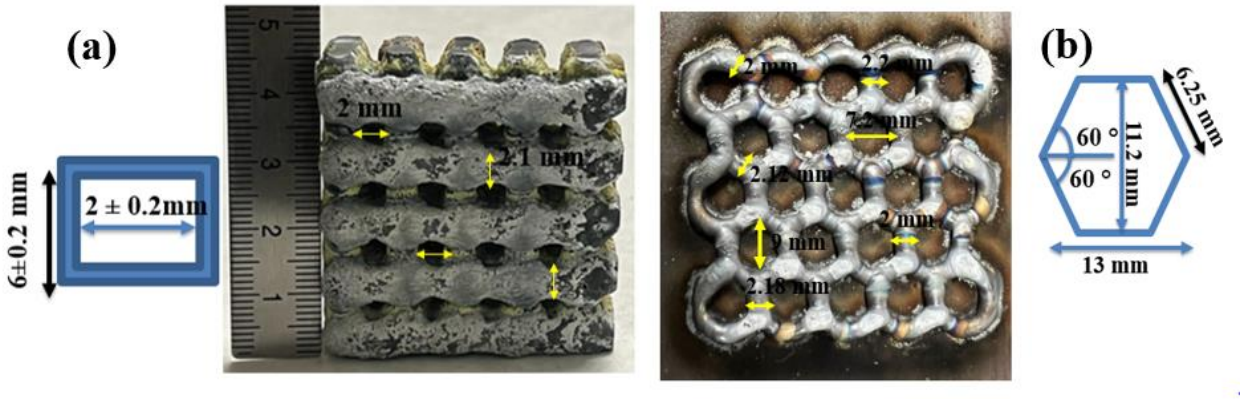

Fig 3.32 WAAM fabricated porous structure (a) Simple Cubic Structure (b) Honeycomb structure

Table 7 WAAM Parameter for porous structures

Layer	1	2	3	4	5
Wire-feedrate (mm/s)	5.5	5.5	5.5	5.5	5.5
Torch lift (mm)	2.3	2.1	1.8	1.5	1.2
Dwell time (s)	40	50	60	70	80
Arc on time during start and end point of a cell(s)	0.2	0.2	0.1	0.1	0.1
Gas flow rate (lpm)	21.37	21.37	21.37	21.37	21.37
Wire feed rate at start and end point of cell (mm/s)	5	5	5	5	5

Second one was honeycomb structure which is a lattice of hollow, thin-walled cells with relatively high compression and shear properties out-of-plane while boasting a low density. Composite honeycomb sandwich structure is widely used for aircraft structures such as control surfaces, radomes, engine cowls, and aircraft interior structure because of its lightweight and high strength characteristics. Low density cellular solids, particularly metallic ones, are widely used in engineering applications, since they can be designed to have high stiffness-to-mass ratios

and desirable energy absorption characteristics. Cellular structures made from shape memory alloys (SMA's) are especially interesting for their potential to deliver superelasticity and shape memory in a light-weight material [144].Other attempts to fabricate SMA honeycombs have been done by mechanical fasteners or gluing ,and a few modeling and design studies, focusing mostly on stiffness and Poisson ratio, have been performed [144-147].

3.4.2 Angular strut Deposition

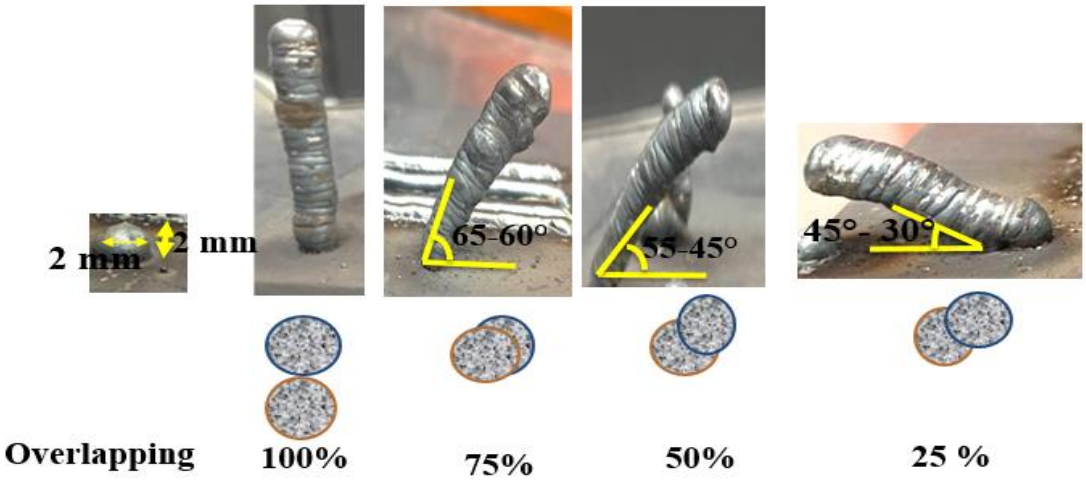

(a) **(b)** **(c)** **(d)** **(e)**

(f)

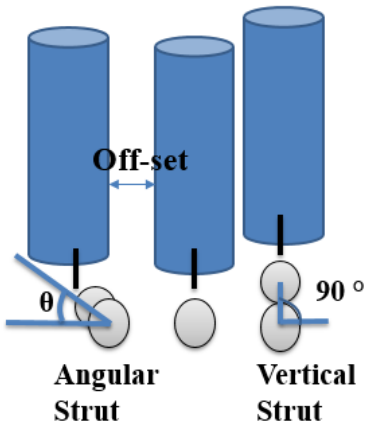

Fig. 3.33 Struts fabricated with different angles (a) 90º, (b) 60-65º, (c) 55-50º, and (d) 45-30º manufactured by WAAM and (b) schematic of angular struct fabrication

Table. 8 WAAM Parameters for angular strut fabrication

Sample	**1**	**2**	**3**	**4**
Wire feed rate (mm/s)	**5.5**	**5.5**	**5.5**	**5.5**
Torch lift (mm)	**2**	**1.1**	**0.5**	**0.35**
Torch off-set (mm)	**0**	**0.5**	**1**	**1.5**
Dwell time (s)	**70**	**50**	**40**	**30**
Angle(°)	**0**			
Gas flow rate (lpm)	**20**	**20**	**20**	**20**
Overlapping (%)	**100**	**75**	**50**	**25**

Fig. 3.33 shows the struts of lattice structure with different angles manufactured by WAAM. Table 10 summarizes the relationship between the lift and offset of the arc torch with the struts angle at a given WAAM parameter. From the data in the Table 8, it can be seen that the lift and offset of the arc torch are closely related to the struts angle. The struts angle could be controlled by adjusting the lift and offset of the arc torch. The relative error of the struts angle manufactured by WAAM did not exceed 5.0%. According to the process of the droplet transition and solidification, when each layer transfers a droplet, the one-layer forming process of the strut consists of four stages: (1) Droplet growth stage: the arc starts to burn the wire to form droplet, and droplet grows continuously. (2) Short circuit transition stage: the droplet is short-circuited with the strut, then the wire is mechanically retracted, and the droplet transfers to the top of the strut smoothly under the combined action of surface tension force and gravitation. (3) Spreading without arc stage: the arc is broken and extinguished, and the liquid deposited metal formed by the droplet spreads without arc. (4) Spreading with arc stage: when droplet transition to the next layer of the strut, the arc reignites and continuously burns to heat the deposited metal, the deposited metal melts and further spreads until the next droplet transits to it, and finally solidifies to form a layer of the strut .

3.5 Summary

1. Laser marking on the titanium substrate reduced the surface roughness, which increased the contact angle due to a change in surface energy. Laser marking during WAAM deposition lead to a maximum wall width reduction of 45 % as compared to walls built without laser marking. The actuation studies indicate an improvement in the shape recovery behaviour due to continuous laser treatment after each and every layer, which refined the grains and change in recovery stress.
2. Cyclic high temperature (lower interlayer delay) exposure of the sample for longer time may have supported coalescence of small pores in lower interlayer temperature sample (higher interdelay sample). Higher interlayer delay (30 s) helps additively built NiTi walls have a more appealing surface finish with less visible surface oxidation, better microstructure, improved hardness, and increased strength. Shape recovery increased with an increase in the interlayer delay due to variation in stress pattern and grain size reduction which have been observed from XRD and SEM results.
3. Porosity found after laser marking was lowest (0.0 6 %) in comparison to interlayer delay (0.45%)and interpass temperature (0.22%) contion condition.
4. Preheating will reduce cold crack probability. Temperature will cause change in viscosity that is reason behind higher width for without interpass temperature control sample. Ni rich phase has been found in lower interpass sample according to phase diagram which will enhance phase transformation temperature and shape recovery behavior.
5. Angular structuct fabrication opens the path way to fabricate different porous structure like triply periodic minimal surfaces (TPMS) through WAAM.
6. The actuation characteristics of WAAM structure are very helpful for tool clamping/holder. It helps to decrease the obstacles related to unnecessary run-out or eccentricity of the cutting tool, which reduces the tool breakage during high speed micro-cutting operations.

WAAM is suitable for the fabrication of porous structures of any metal, which overcomes the shortcomings of high requirement for fluidity or ductility of materials manufactured by traditional methods and high absorbance of materials manufactured . WAAM is also suitable for the fabrication of porous structures of any complex form. In addition, it also has the advantages of unlimited size in open forming environment, high efficiency and low cost. High heat

accumulation and lower cooling rate will affect the NiTi deposition but substrate roughness reduction, preheating, dwell time and interpass temperature control can help in resolving this issues. The struts with different angles and diameter form the lattice structures with different relative-density and construction, which form different mechanical properties of elastic modulus, compressive strength, heat insulation, and shock absorption, etc. Therefore, how to control the diameter and angle of the struts in the porous structure by WAAM should be a problem to be studied.

Chapter 4

NiTi integrated Bimetallic Structures fabrication through WAAM

4.1 Introduction and Manufacturing Challenges of bimetallic structure

Bimetallic components involve joining two different materials to obtain tailored properties at different locations of the same component. These components allow for the optimization of overall performance while avoiding the restrictions of each other [147-155].

Several research initiatives aimed at joining NiTi alloys have recently been carried out, with successful findings reported by several research groups [149 -154]. These properties attract their deployment in several sectors ranging from medical, aerospace, automotive, etc. The formation of brittle intermetallic phases causes the joint to become brittle, and the thermal expansion mismatch associated with dissimilar welding causes transverse cracks in the brittle weld metal, results in the loss of mechanical property. Casting, explosive welding, diffusion bonding, powder metallurgy, and other methods are used to fabricate bi-metallic structures [155-160].

There are several studies available that have investigated the interface characteristics of bimetallic walls made of different combinations of NiTi with other materials like Ti, SS, and Cu.

One study conducted by Wang et al. (2020) investigated the interface characteristics of NiTi-Ti bimetallic walls fabricated using laser melting deposition. They found that the compositional variations at the interface were minimal, and there was no detectable diffusion layer. The interface between the two materials was observed to be continuous and smooth.Another study by Zhang et al. (2018) investigated the interface characteristics of NiTi-SS bimetallic walls fabricated using explosive welding. They observed that there was a thin diffusion layer at the interface, and the compositional variations were also present. The interface was observed to be discontinuous, and there were some waviness and undulations present.

Similarly, a study by Lertthanasarn et al. (2017) investigated the interface characteristics of NiTi-Cu bimetallic walls fabricated using friction stir welding. They observed that there was a significant diffusion layer at the interface, and the compositional variations were also present. The interface was observed to be discontinuous, and there were some undulations present.

Overall, it can be concluded that the interface characteristics of bimetallic walls depend on several factors such as the fabrication process, the materials used, and the parameters used during the fabrication.

Complex-shaped NiTi and Ti/SS/Cu components are difficult to fabricate using conventional manufacturing processes such as turning, milling, forging, and casting, which limits the potential applications of these smart functional materials [160-167]. Fabrication of NiTi components by WAAM has been proven to be successful in manufacturing parts based on these materials with reduced overall costs and high deposition rates when compared to several frequently used fusion-based AM processes, such as Selective Laser Melting and Electron Beam Melting [162-164].

Till now there is no work on the fabrication of multi-layered Nitinol and Ti /SS/Cu bimetallic structures using WAAM. As a result, the current work employs WAAM to fabricate a defect-free bimetallic structure of Nitinol and Ti, as well as explain its microstructure, martensitic transition, mechanical properties, and actuation behaviour.

4.2 Experimental setup

Nitinol (Ni50.9Ti49.1) and Ti/SS316L/Cu with a wire diameter of 1.2 mm were used as feedstock materials in this investigation. A titanium block with 100 mm x 100 mm x 10 mm served as the substrate for NiTi-Ti joint and for other two mild steel of same size was used as a subsrate. WAAM system based on Gas Metal Arc Welding (GMAW) was used to manufacture bimetallic structures of Nitinol and Ti/SS/Cu (Fig. 1a). The process parameters were optimized for continuous and uniform deposition of Nitinol and Ti / Cu/ SS separately. The variation in width was caused by the temperature gradient encountered by each material along the thickness of the weld. However, they have different thermo-physical properties leading to different heat transfer rates in each material and due to which final structure of the wall will get affect.So for material parameters has been optimized to get same width and uniformity.

Table 8 shows the optimized parameter used for depositing bi-metallic wall structures. Prior to the deposition, the substrate was preheated to a temperature of 400°C to increase bonding between the two dissimilar materials. Other details about the WAAM system has been given in section 1.2.3.4.

Table 9 WAAM parameters used for bimetallic joints for NiTi –Ti/SS/Cu

Materials	Wire feed rate (m/min)	Argon gas flow rate (l/min)	Stand-off distance (mm)	Voltage (V)
Ti	5.8	15	15	16.5
NiTi	5	15	15	16.5
Cu	5	15	15	15
SS	5.5	15	15	16.5

4.3 Results and Discussion

4.3.1 SEM AND XRD Results

Fig. 4.1 (a-b) depicts a cross-section of the WAAM built bi-metallic structure, demonstrating that the structure is defect-free on macro-scale, with layer by layer morphology visible throughout the structure. Some of the previously deposited layers was found to be re-melted during multi-layer deposition, resulting in visibly apparent re-melted zones between the layers. Remelting the prior layers improved the bonding between the layers. Fig. 4.1 (d) show the compositional analysis carried out on the WAAM deposited bimetallic joint interface. Ti-rich zones can be seen from the elemental maps obtained along the bi-metallic joint. The deposition moves from 100% Ti at the Ti-rich bottom layers to a zone with a gradual reduction in Ti composition from Ti side to NiTi side. Further, the presence of oxygen is detected during the analysis, with a higher percentage at the Ti-rich zone, which indicates the formation of Ti oxides during the deposition in the Ti side [159].

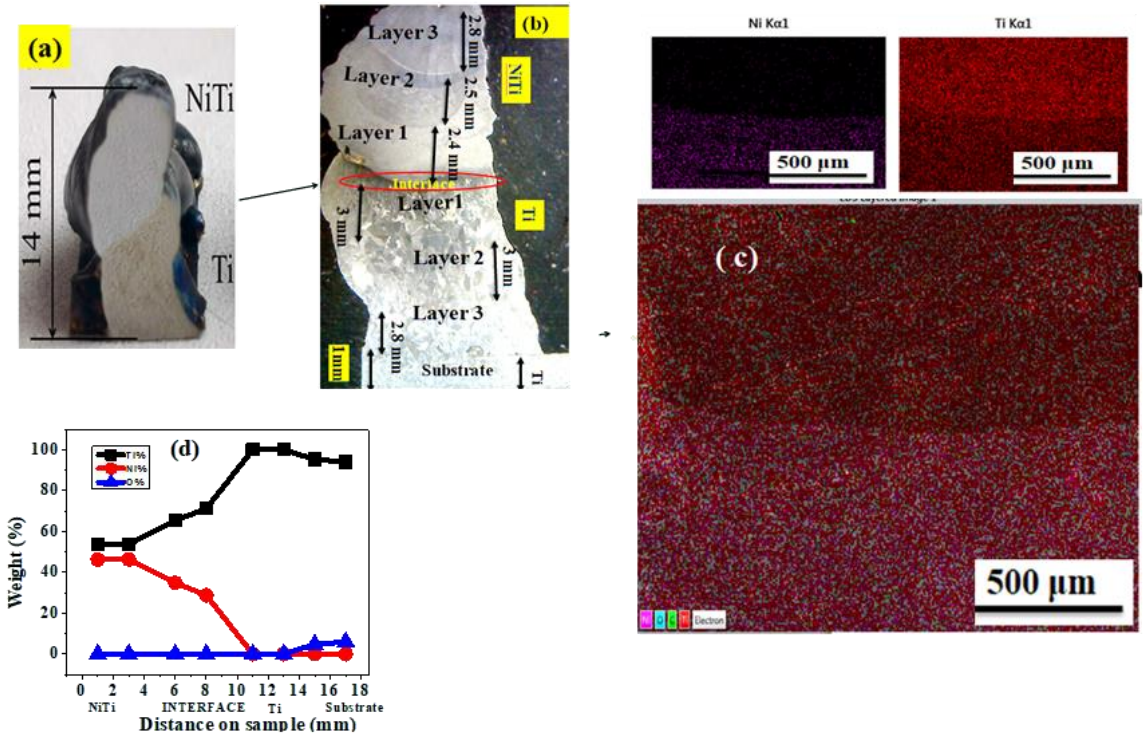

Fig. 4.1: Bi-metallic joint (a),(b) Macro-structure, (c) Elemental mapping, and (d) Compositional analysis

Fig. 4.2 presents the microstructure and X-ray diffraction pattern obtained at different locations of NiTi-Ti bimetallic structure. Dendrite structure was formed at the interface, which showed Ti-rich intermetallic compounds as confirmed by EDS results. Two intermediate zones near the joining direction were found on the NiTi side. The first zone was in with the Ti layer, and its width was about 100-150 µm. This zone was consisted of pure Ti (marked by "A"), Ti solid solution with Ti concentration of 90 at. % (marked by "B") and Ti_2Ni precipitates (marked by "C"). The second zone (Ref. Fig. 7.2 a) was consisted of the $NiTi_2$ phase and Ti-rich NiTi individual grains (marked by "D"). The grains of $Ni_{49.5}Ti_{50.5}$ (marked by "D") were surrounded by the $NiTi_2$ phase which was far away from the joint. The X-ray diffraction patterns (Fig. 4.2 b, c, and e) confirmed the structure of the NiTi/Ti composites in various locations. Furthermore, X-ray diffraction studies reveal that at room temperature, the NiTi phase is in the austenite state, which is consistent with the chemical composition of this phase. The Ti-rich NiTi phase demonstrates the martensitic transformation at high temperatures and should be in the martensite state at room temperature [164]. WAAM deposited Ti layers exhibited mainly serrated α phase

with limited amounts of intergranular β phase in some areas (Fig. 4.2 d). This microstructure is generally uniform, with a Widmanstätten α phase morphology and small layers of preserved β phase between the lath boundaries. This can be validated by the XRD pattern of Ti, which is usually a mixture of α titanium and β titanium with a hexagonal lattice structure (Fig. 4.2 e). Due to their strong affinity and the occurrence of chemical reactions inside the melt pool, Ti and Ni may easily produce $NiTi_2$ and Ni_3Ti intermetallic phases. The mechanical properties of the joint can be adversely affected by these brittle intermetallic phases. NiTi has a lower melting point than Ti, it participates more in joint formation, resulting in more intermetallic compounds being formed on the NiTi side.

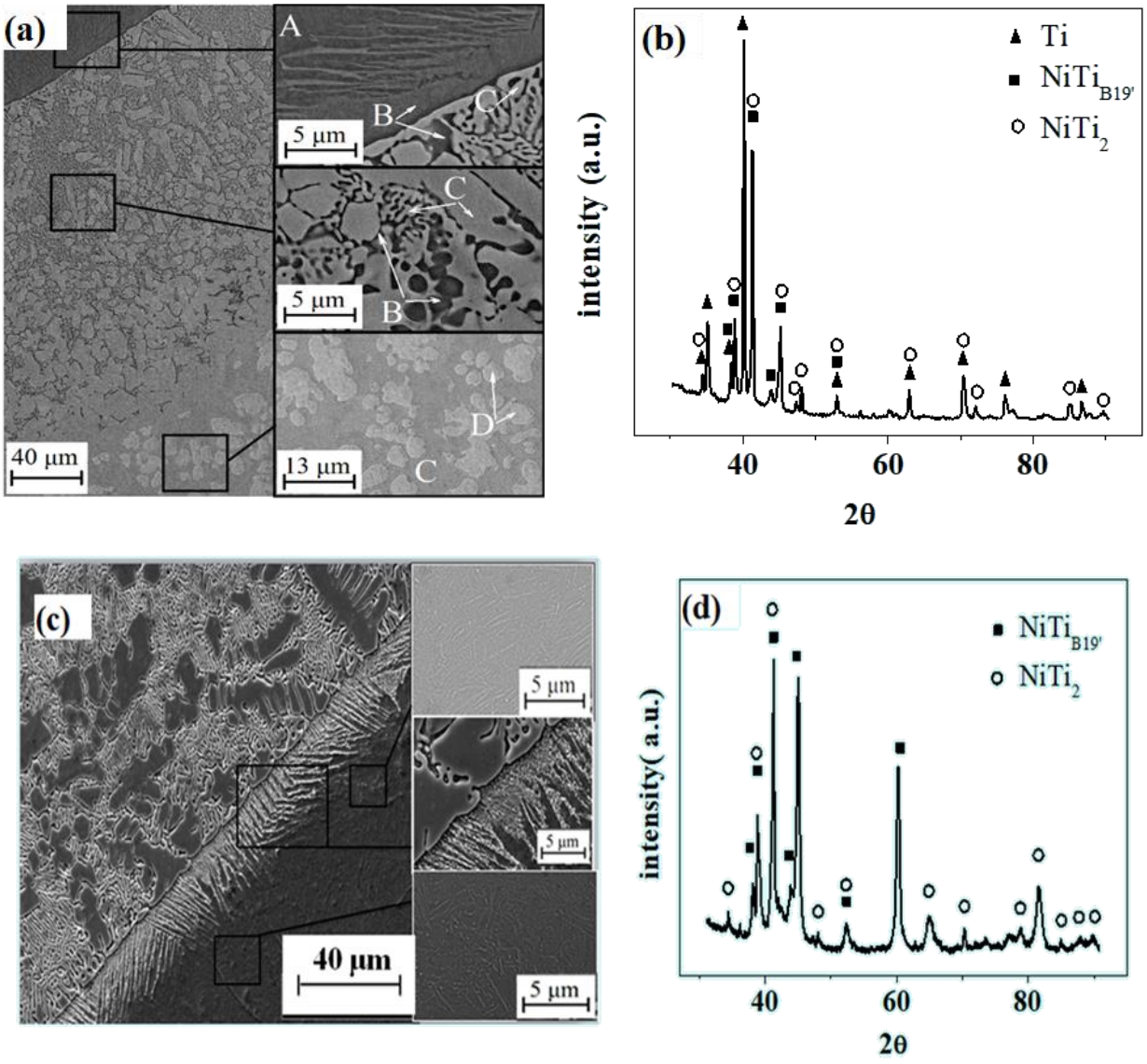

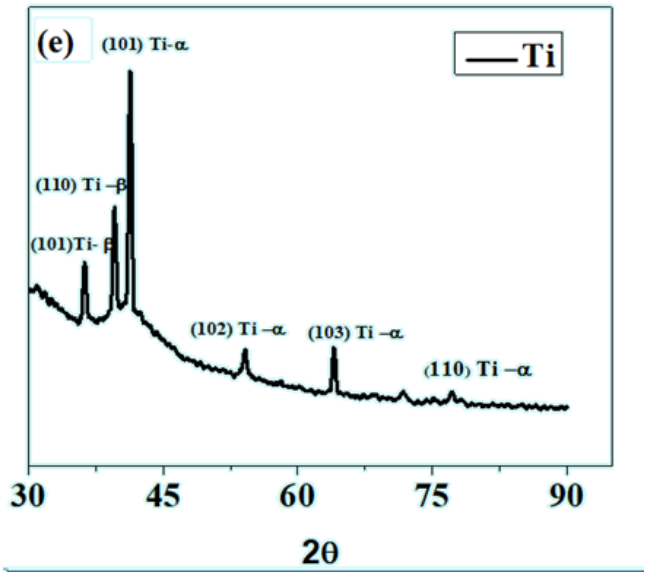

Fig. 4.2 SEM images (a, c) and X-ray patterns (b, d, and e) found in the vicinity of NiTi, joint, and Ti side

A defect-free bimetallic wall is observed at the macro-scale, with layer by layer morphology (typical for WAAM samples), which is visible throughout the structure (refer Fig. 4.3 (a) and (b)). It may be observed that the NiTi composition is built over the SS 316L. Fig. 4.3 (c) shows a smooth transition in the composition is evident, which is seen with the variation in Cr, Ti and Fe composition across the joint. A slight enrichment of Ni is seen in the NiTi region as compared to the SS 316L region and Cr and Fe are also observed along the NiTi zone. Thus, it may be inferred from the above that brittle intermetallics formation has taken place at the interface during the deposition, which may be primarily a diffusion controlled process driven by the high solidification rates observed during WAAM [169]. Ni enrichment along NiTi also indicates the formation of Ni_3Ti phase [170].

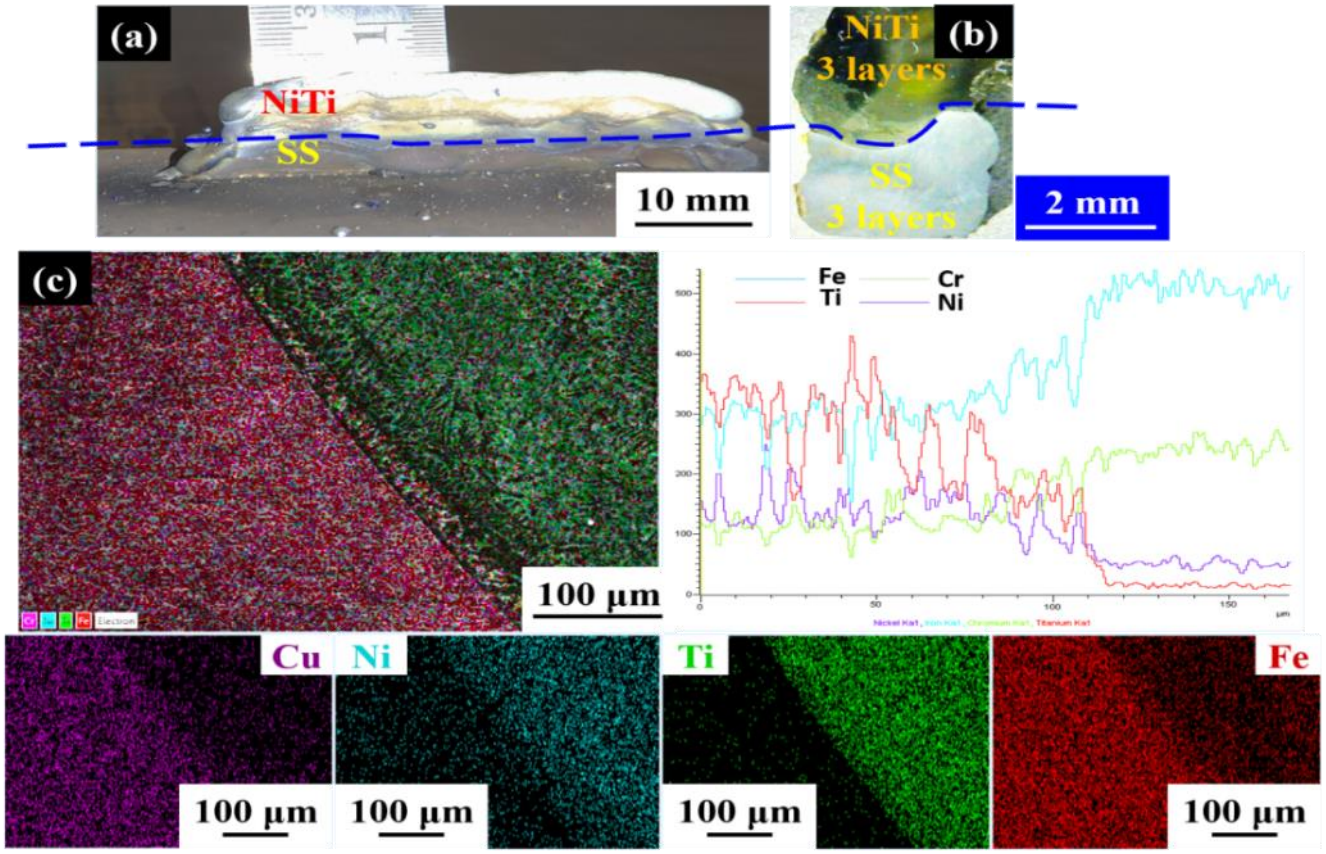

Fig. 4.3 WAAM fabricated bi-metallic wall (a) Photographic and (b) Cross-sectional view (c) EDX mapping

Fig. 4.4 (a) shows the SEM microstructure along the deposit centerline and bimetallic joint interface of the dissimilar NiTi–SS joint. The NiTi region primarily comprises of coarse and light grey dendrites (NiTi phase) that are evenly distributed on the dark grey matrix ($NiTi_2$ phase). Along the NiTi side, the top region revealed dendritic microstructure with a random orientation, while preferentially oriented growth is seen in the middle region. Generally, dendrite grow preferably along the maximal thermal gradient direction [170]. Along the SS side, (Fig. . 4.4 (a)), austenitic dendrites that are well-aligned vertically are seen with middle region having large columnar grains. The ferrite exhibits reticular morphology within the austenitic dendrite. The SEM image of the SS side indicates that the microstructure consists of austenite (γ), delta-ferrite (δ) and sigma (σ) phase. The δ and σ phase exhibit fine vermicular morphology within the γ matrix.

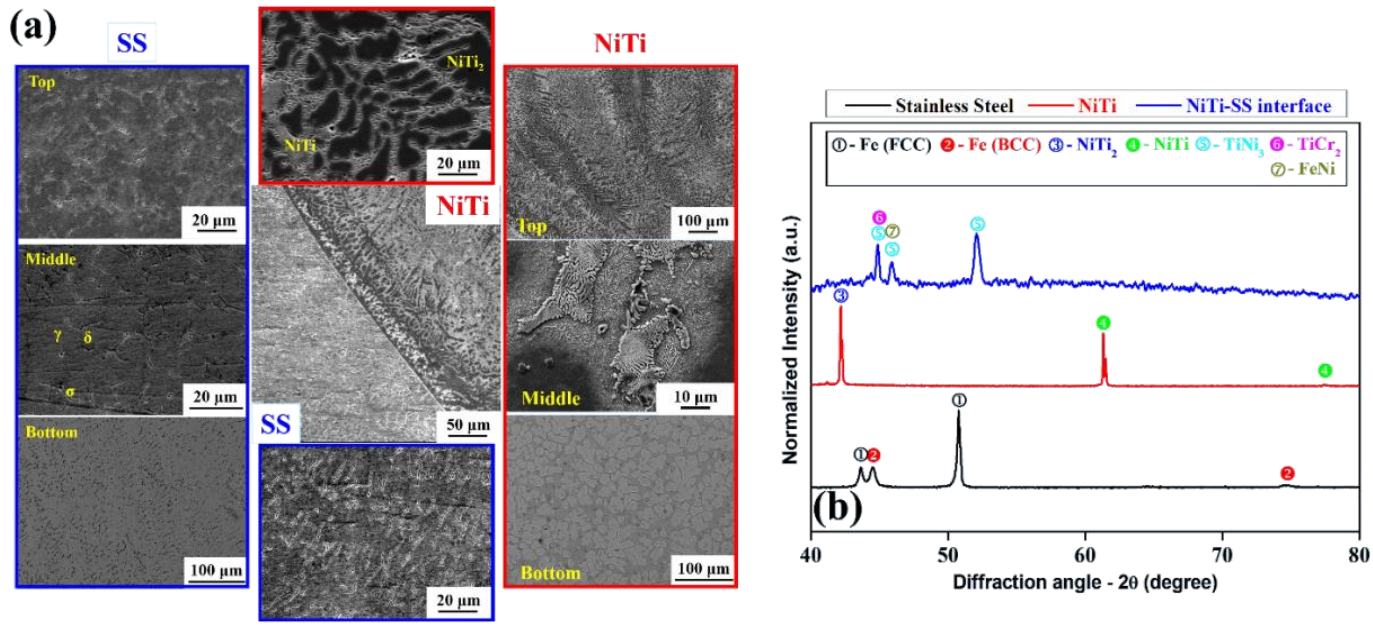

Fig. 4.4 (a) SEM microstrcutures at different regions (b) XRD patterns

Fig. 4.4 (b) shows the XRD patterns taken from the bi-metallic structure along the Ni-Ti, SS and NiTi–SS interface. The XRD pattern taken along the NiTi show the presence of two inermetallic phases namely, $NiTi_2$ and NiTi (B2) phase. On the other hand, the XRD pattern for SS shows that the presence of bimodal microstructure with both austenitic and ferritic phases coexisting at the same time. Such microstructure may be observed mainly due to non-equilibrium solidification during WAAM process. However, the NiTi–SS interface shows the presence of brittle intermetallic compounds such as $TiCr_2$, $TiNi_3$ and FeNi along with the γ-Fe and α-Fe parent phases and in line with the previously reported literatures [171-173].

Fig. 4.6 shows SEM images and X-ray results found in various sites of the NiTi/Cu composite (Fig 4.5). It is seen, that there is not strict joint line between Cu and NiTi and a wide mixed zone about 500 µm was found. This zone consisted of $Ti(Ni,Cu)_2$ phase (marked by "E") with inclusions of pure Cu (marked by "F"), $Ti_2(Ni,Cu)_3$ precipitates (marked by "G") and Ni-rich NiTi precipitates in NiTi(Cu) phase (marked by "H") (Fig. 4.6 a). The structure of the joint area was confirmed by X-ray patters (Fig. 4.6 b). On increase in the distance from the joint to NiTi side, amount of $Ti(Ni,Cu)_2$ and $Ti_2(Ni,Cu)_3$ precipitates decreases whereas, the volume fraction of NiTi(Cu) phase increases. Far from joint, the NiTi layers consisted of NiTi(Cu) phase and a small amount of $Ti_2(Ni,Cu)$ precipitates (marked by "I") on the boundary of the NiTi(Cu) grains

(Fig. 4.6 c). On an increase in the distance from the joint the Cu concentration in the NiTi phase decreases from 15 at. % (in the vicinity of joint) to 1 % in top NiTi layer. Despite the location, the Ni+Cu concentration in NiTi phase is higher than 50.0 at. %, moreover the Ni concentration in this phase was not homogeneous even in top layers and varied from 51 to 52 at. %. The X-ray result (Fig. 4.6 d) shows that NiTi phase at room temperature was in austenite structure that correlated to chemical composition of this phase detected by EDS [174].

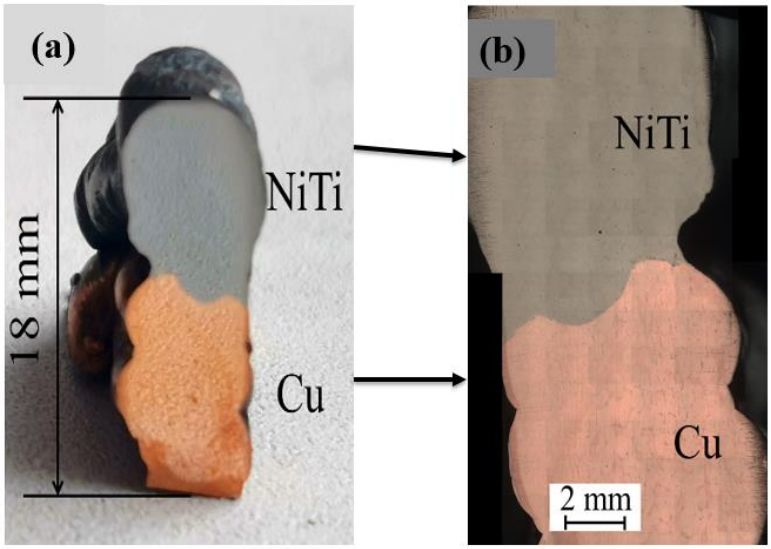

Fig. 4.5 Photos (a) and images obtained in optical microscope (b) of the NiTi/Cu bimetallic composites, produced by WAAM

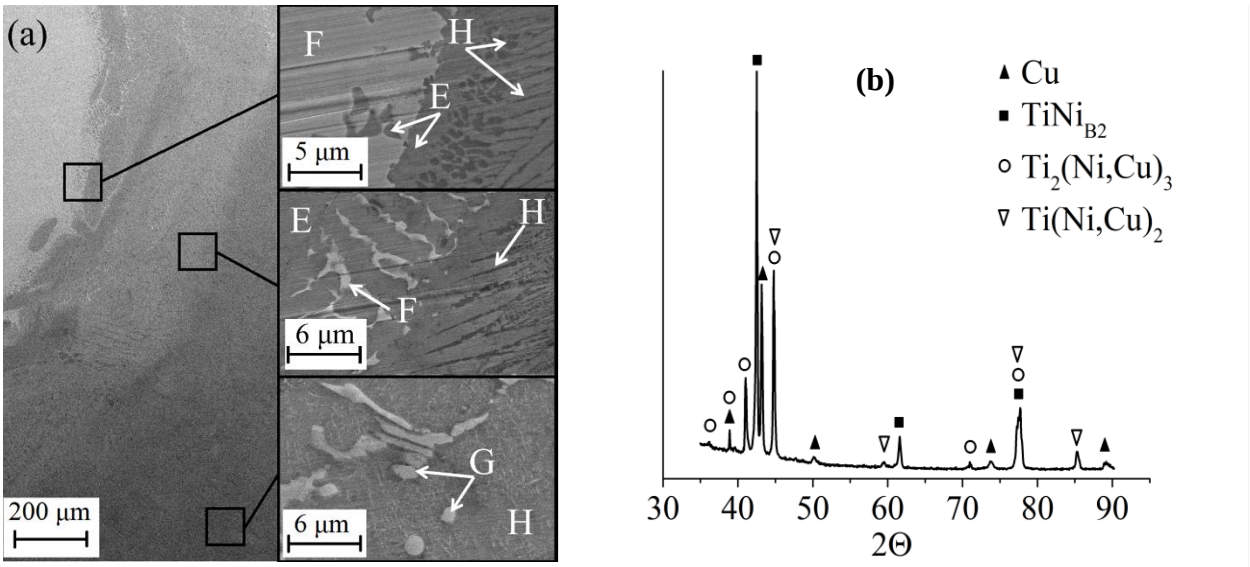

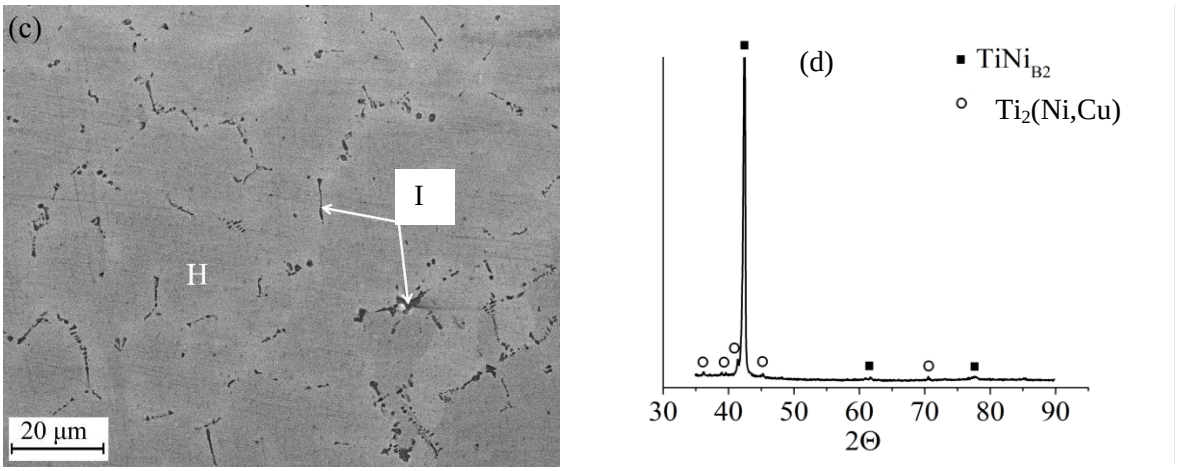

Fig 4.6 SEM images (a, c) and X-ray patterns (b, d) found in the vicinity of joint (a, b) or far from joint (c, d) in the NiTi layer of the NiTi/Cu bimetallic composite

4.3.2 Phase Transformation Behaviour

Fig 4.7 shows the calorimetric curves found on heating and cooling of NiTi-Ti composite. A heat release peak has been found on cooling and attributed to B2→B19′ transformation. The reverse B19′→B2 transformation causes the heat absorption peak when heated. On calorimetric cures for cooling and heating, certain low-intensity heat flow peaks may be seen (shown by circle in Fig. 4.7) which indicate the B2 ↔ B19' martensitic transformation occurs at various temperatures due to some deviation of the chemical composition of the NiTi phase. Transformation temperatures were determined according to ASTM F2004-05R10 as intersections of tangent lines, and transformation enthalpy was found as square under a peak (accuracy is ± 1 ^{o}C for transformation temperatures and ± 1 J/g for enthalpy). The transformation temperatures, as well as enthalpy did not depend on the location of the samples in the NiTi-Ti composite, except the sample cut from the joint area (Table 9). The transformation enthalpy at the joint area was found to be lower than in samples taken farther away from the joint because this sample had a pure Ti layer as well as the various phases mentioned above in the intermediate zone. Only the NiTi phase underwent the martensitic transformation and contributed to the transformation enthalpy at the same time.

Table 10. Temperatures and enthalpy of the martensitic transformation in the NiTi layers of NiTi-Ti bimetallic composites.

Material	Sample	Transformation	M_s, ^{o}C	M_f, ^{o}C	A_s, ^{o}C	A_f, ^{o}C	E_{fw},	E_{rev},

	location						J/g	J/g
NiTi-Ti	top	B2 ↔ B19’	80	37	70	109	29	28
	middle	B2 ↔ B19’	77	37	70	108	29	30
	joint	B2 ↔ B19’	71	37	70	102	15	14

In Table 2, M_s and M_f refer to start and finish temperatures of the forward transformation on cooling, A_s and A_f refer to start and finish temperatures of the reverse transformation on heating, E_{fw} and E_{rev} refer to enthalpies of the forward or reverse transformations

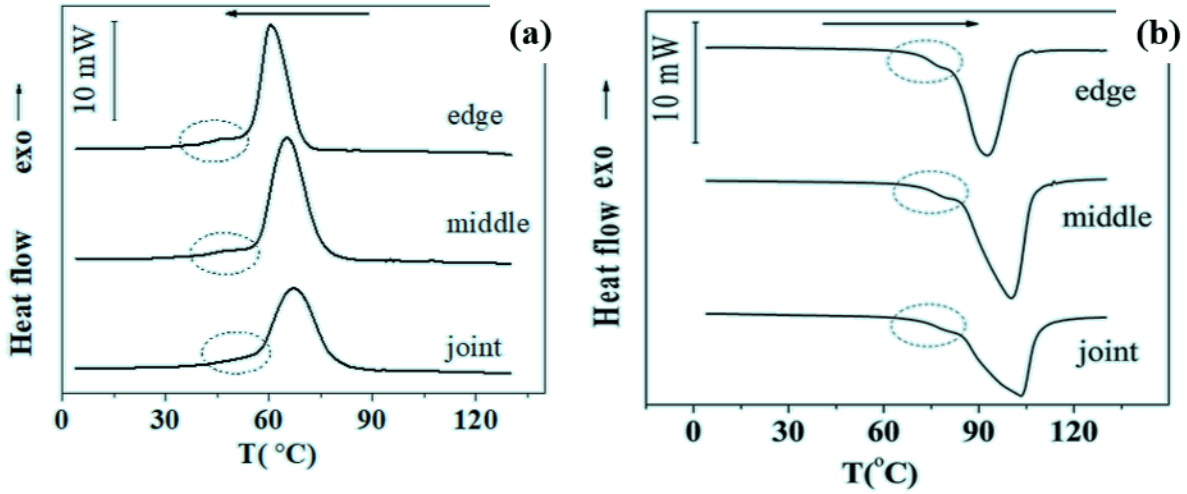

Fig. 4.7 Calorimetry curves obtained on cooling (a) and heating (b) of samples cut in various locations of the NiTi layers in NiTi-Ti- (a,b) bimetallic composites

The DSC traces along NiTi zone of the deposition exhibits the typical phase transformation (Fig. 4.8(a)), whereas the NiTi-SS zone does not exhibit any phase transformation (Fig. 4.8(b)). This may be due to the suppression of the first-order martensitic transformation or reverse transformation with the addition of Fe. Therefore, the second-order-like phase transformation from an incommensurate stage to a commensurate stage can possibly occur [26].

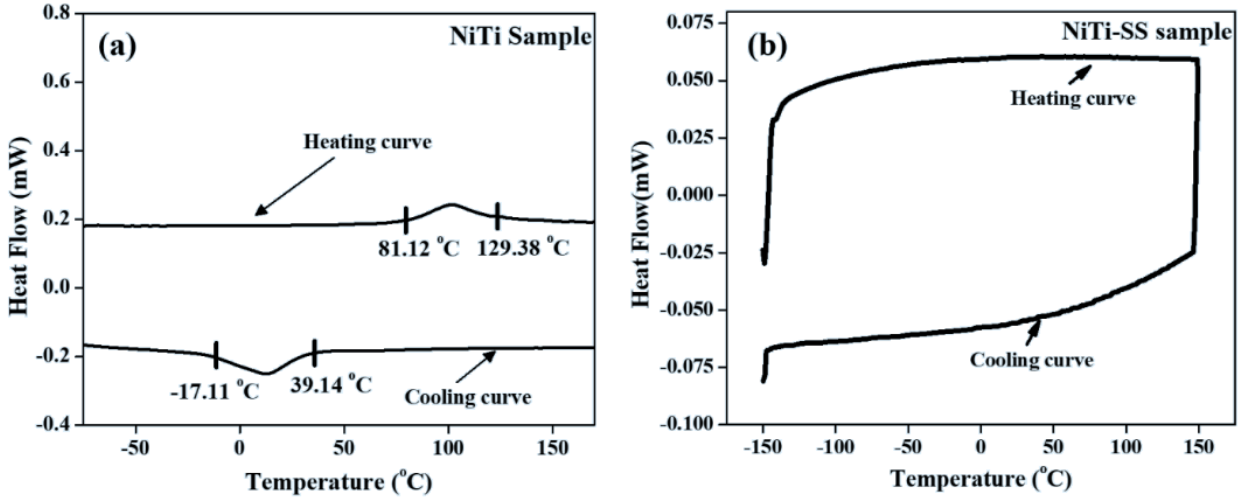

Fig. 4.8 DSC traces observed for the (a) NiTi and (b) NiTi-SS samples

Samples cut from the NiTi/Cu composite, demonstrated low-intensity broad peak of heat release on cooling and peak of heat absorption on heating (Fig.4.9). Transformations parameters hardly depended on location of the samples in the NiTi/Cu composite (Table 10) and were characterized by small enthalpy and hysteresis ($H=A_f - M_s$) that was correspond to the B2↔R transformations. According to SEM and X-ray analysis a large value of the NiTi layers were occupied by secondary phases ($Ti(Ni,Cu)_3$ and $Ti_2 (Ni,Cu)_3$), which did not undergo martensitic transformations that was why the volume fraction of the NiTi phase was small. This was one of the reasons for an observation of low-intensive calorimetric peak. The presence of a significant amount of Ni in the NiTi, which reduced the transformation enthalpy, was the other reason. Transformations temperature ranges (M_s-M_f and A_f-A_s) were very wide (~ 100 ^oC), that was due to inhomogeneity of chemical composition of the NiTi phase. As it was mentioned above, the Ni-rich NiTi phase with different Ni/Ti ratio were found in the NiTi layers. Because of this, different volume of NiTi phase underwent the martensitic transition at varying temperatures [174-181].

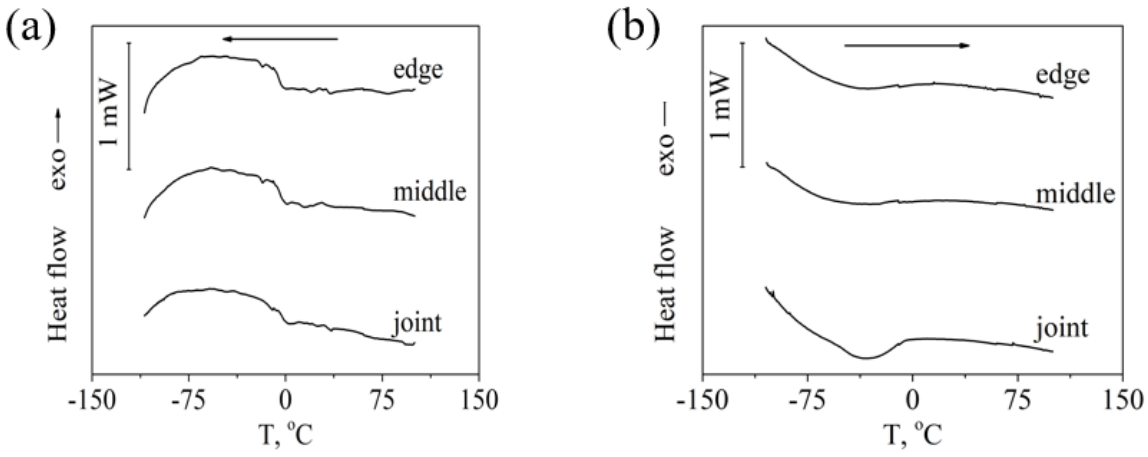

Fig. 4.9 Calorimetry curves obtained on cooling (a) and heating (b) of samples cut in various location of the NiTi layers in NiTi/Cu bimetallic composites

Table 11 Temperatures and enthalpy of the martensitic transformation in the NiTi layers of NiTI/Cu bimetallic composites. M_s and M_f – start and finish temperatures of the forward transformation on cooling, A_s and A_f – start and finish temperatures of the reverse transformation on heating, E_{fw} and E_{rev} – enthalpies of the forward or reverse transformations

Composite	Sample location	Transformation	M_s, °C	M_f, °C	A_s, °C	A_f, °C	E_{fw}, J/g	E_{rev}, J/g
NiTi/Cu	top	B2 ↔ R	1	<-110	-96	3	3	1
	middle	B2 ↔ R	3	<-110	-96	2	3	1
	joint	B2 ↔ R	-1	<-110	-87	-3	3	1

A low transformation enthalpy and a wide temperature range show that the samples are not able to demonstrate good functional properties. Thus, the martensitic transformation should be improved by heat treatment. To study the influence of the heat treatment on the martensitic transformation, the samples were annealed at 500 °C for 4 – 16 hours. Fig. 4.10 shows the calorimetric curves measured in the samples cut near the joint after different heat treatment. It is

seen that annealing for 4 hours at 500 ^{o}C leads to the observation of four peaks on cooling and three peaks on heating. Using the special procedure, it was found that on cooling the peak A was caused by the B2 $\rightarrow$ R transformation and peak C was corresponded to the R $\rightarrow$ B19' transformation. On heating this B19' phase transformed to B2 phase within peak F. The peaks B and G were due to the B2 $\leftrightarrow$ B19' transformations as well as peaks D and E were caused by the same B2 $\leftrightarrow$ B19' transformation. The observation of different sequences of the transformation was due to the NiTi layer near the joint had various distribution of the Ti and Ni concentration before annealing. This resulted in the annealing affected in various way the areas of the NiTi phase with different chemical compositions. In Fig. 4.10 it is seen that an increase in annealing duration increases the intensity and temperatures of all peaks. This was due to the Ni concentration in the NiTi phase decreases during annealing that increases the transformation temperatures and the volume fraction of the alloy undergoing the phase transformation. At the same time, the comparison of the calorimetric curves obtained after 12 and 16 hours does not show any distinctions in transformation enthalpy or temperatures.

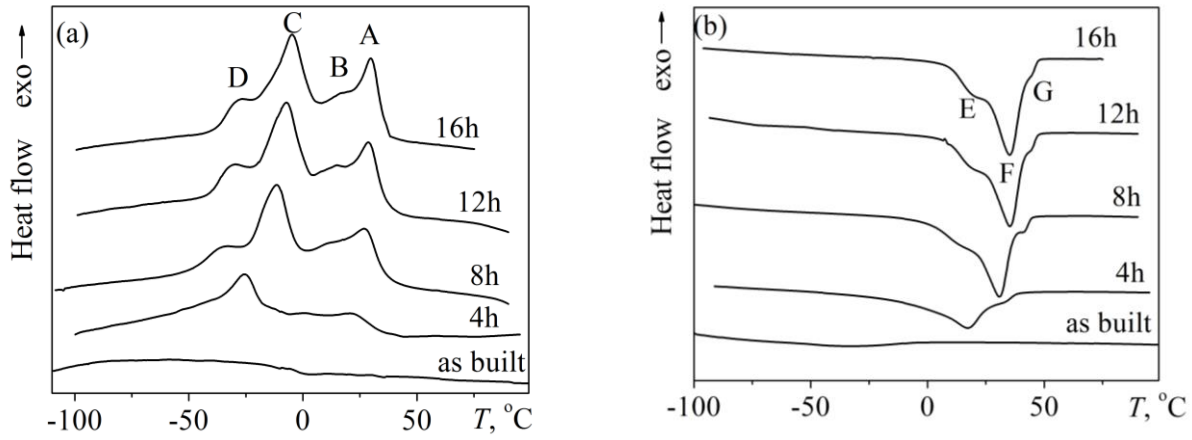

Fig. 4.10 Calorimetry curves obtained on cooling (a) and heating (b) of samples cut in the NiTi layers near the joint in NiTi/Cu bimetallic composite. Annealing duration is shown near the curves

Fig.4.11 shows the calorimetric curves measured in the samples cut from meddle and edge areas of the NiTi/Cu cross-section and annealed at 500 ^{o}C for different durations. It is seen that in both samples cut from the medium and edge (far from joint) of the NiTi layer, the B2 $\rightarrow$R$\rightarrow$B19'

transformation takes place on cooling (peaks A and C) and B19' → B2 transition occurs on heating (peak F). Moreover, it was found that the annealing affected more intensive in the middle areas because the intensity of the peak in the sample cut from middle of NiTi layer after annealing for 8 hours was larger than in the sample cut from the edge of the NiTi layer. It may be caused by the a large concentration of the Cu in the middle sample assisted in the precipitates formation during annealing that decreases the Ni concentration in the NiTi matrix and increased the volume fraction of the alloy undergoing the martensitic transformation. An increase in annealing duration to 12 hours increased the transformation enthalpy, whereas a rise in the annealing duration over 12 hours hardly influenced the transformation parameters (enthalpy and temperatures). Thus, it may be concluded that annealing at 500 ^{o}C for 12 hours is the optimal heat treatment that allows restoring the transformation in the NiTi/Cu composite.

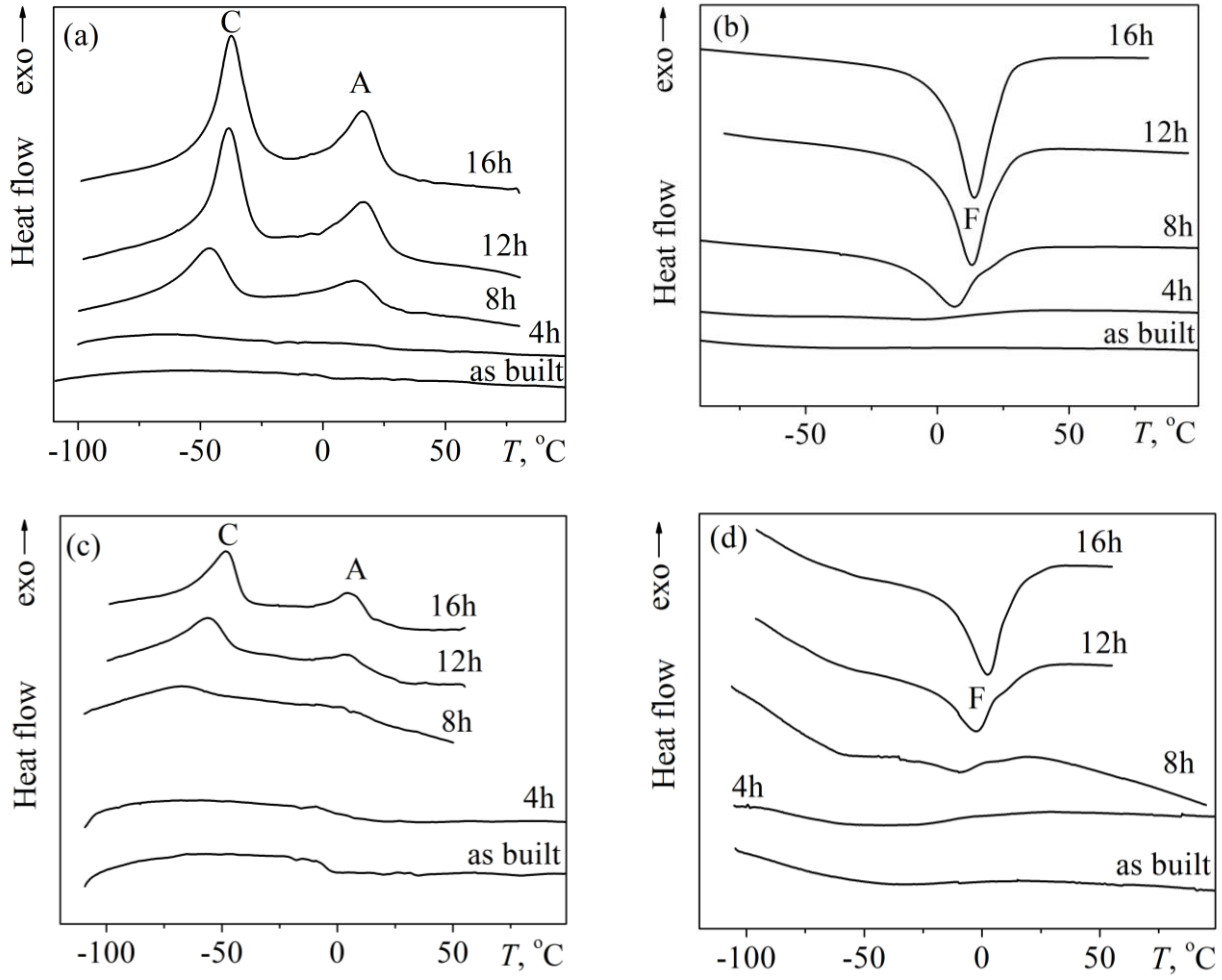

Fig. 4.11 Calorimetry curves obtained on cooling (a, c) and heating (b, d) of samples cut in

middle (a, b) or edge areas in the NiTi layers of the NiTi/Cu bimetallic composite. Annealing duration is shown near the curves.

4.3.3 Mechanical Propersties

4.12 (a) presents the variation in the micro-hardness in the NiTi-Ti sample, and it was observed that the micro-hardness of the NiTi zone varies from 250 – 400 HV. The micro-hardness values at the interface joint are more than that of base metals, indicating the formation of hard and brittle phases. The presence of $NiTi_2$ confirmed by XRD studies results in higher hardness of weld metal within the interface. The presence of impurities, particularly oxygen, has an effect on the hardness of Ti. Furthermore, because to the presence of distinct components along grain boundaries in microstructures, the hardness of WAAM generated Ti is primarily regulated by the solid solution and grain boundaries. [165]. Grain boundaries and dislocations are more abundant in alloys with a faster cooling cycle in the bottom region, leading to enhanced micro-hardness. In the composition range studied, the strength and hardness of binary Ti-O, Ti-N, and Ti-C alloys are linear functions of alloy concentration. The microstructure towards the top of the WAAM thin-wall components, on the other hand, includes a lot of martensite structure, which is often hard and more intense. The hardness of WAAM-built NiTi and Ti layers is greater than that of conventionally manufactured NiTi and Ti layers (296 HV for NiTi and 170 HV for Ti). In addition, the micro-hardness at the NiTi-Ti joint interface was also higher than the hardness obtained at the interface of NiTi and Ti (550 HV) obtained by laser welding [159]. Fig. 4.12 (b) shows the stress-strain curve of NiTi-Ti bimetallic under compressive loading. The compressive strength of WAAM deposited joint was found to 750 MPa. Dissimilar joints reveal lower horizontal stress plateaus than Nitinol's stress plateau. Because the two layers (TiNi and Ti) are linked in bimetallic composites, it is impossible to deform the TiNi layer independently. As a result, both layers deform concurrently during the preliminary compression. The formation of brittle phases, according to XRD data, may be responsible for the reduced compressive strength and elongation compared to base metals. On both sides, failure occurs through the fusion zone dendrites. In the Ti_2Ni granular regions, brittle transgranular cracking with a smooth, almost bright surface due to interdendritic precipitation of Ti_2Ni in the fusion zone, an intergranular failure occurs through the dendrites of the primary solidification phases beta-Ti and NiTi, resulting in a dimple fracture surface morphology Fig 4.12 c.

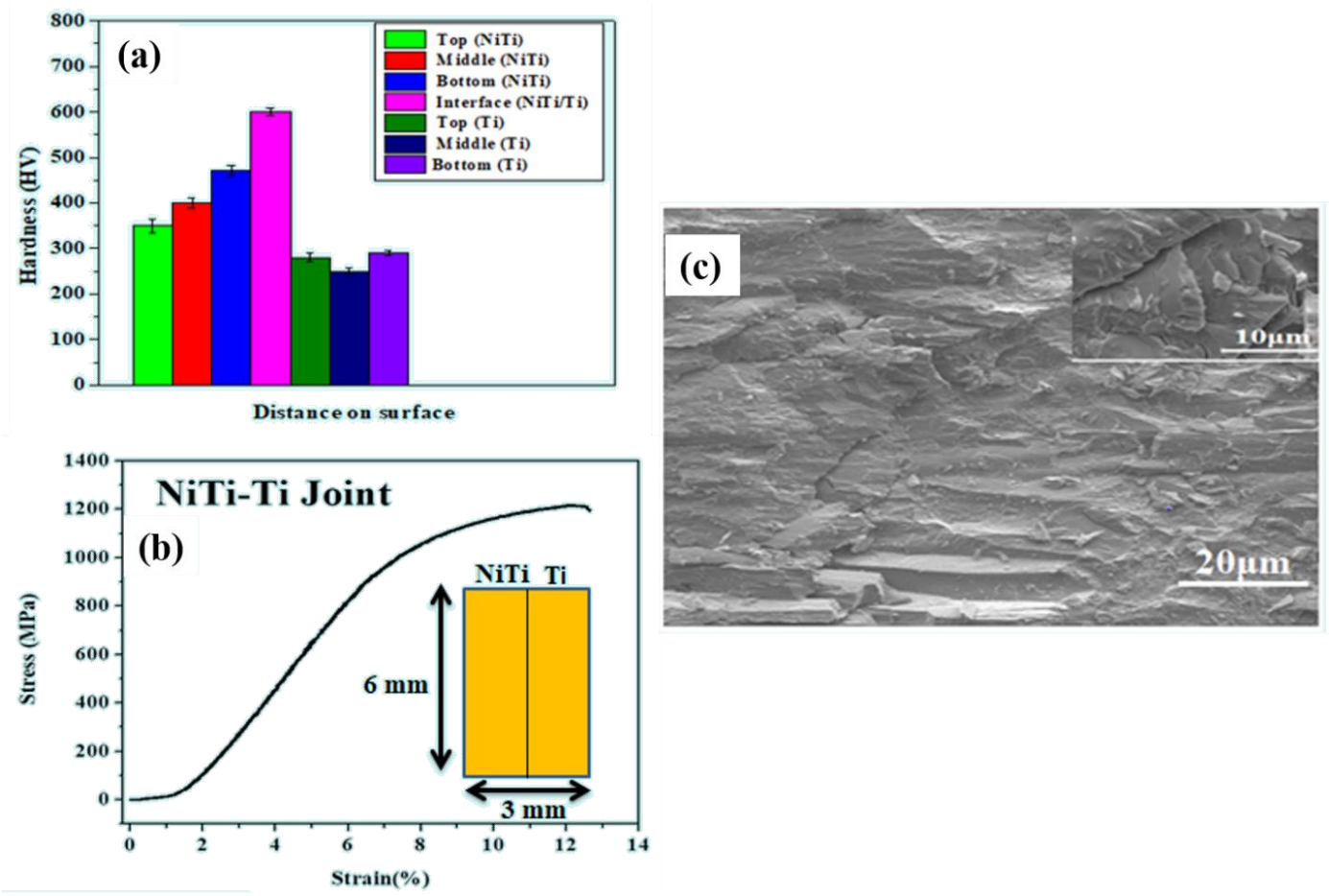

Fig. 4.12 Mechanical Behaviour of Bi-metallic joint (a) Micro-hardness (b) Compression strength (c) Fractography

The higher hardness (400 HV) is obtained at the interface primarily (refer Fig. 4**.1**3 (a)) due to the formation of the intermetallic phases, which is in agreement with published reports [172-173]. The ultimate strength of the joint under compression is 570 MPa (refer Fig. 4.13(b)) and the fracture of the joint takes place in the fusion zone on the NiTi alloy side, confirming it as the weakest zone. The fracture is transgranular, presenting a faceted texture, due to changes in orientation of the cleavage planes from one grain to another. EDS mapping presented in Fig. 4.13(c) confirms the presence of intermetallic compounds such as $TiCr_2$, and $TiNi_3$. A brittle fracture surface is observed, which can be attributed to the presence of the brittle intermetallic phases at the joint [172-173].

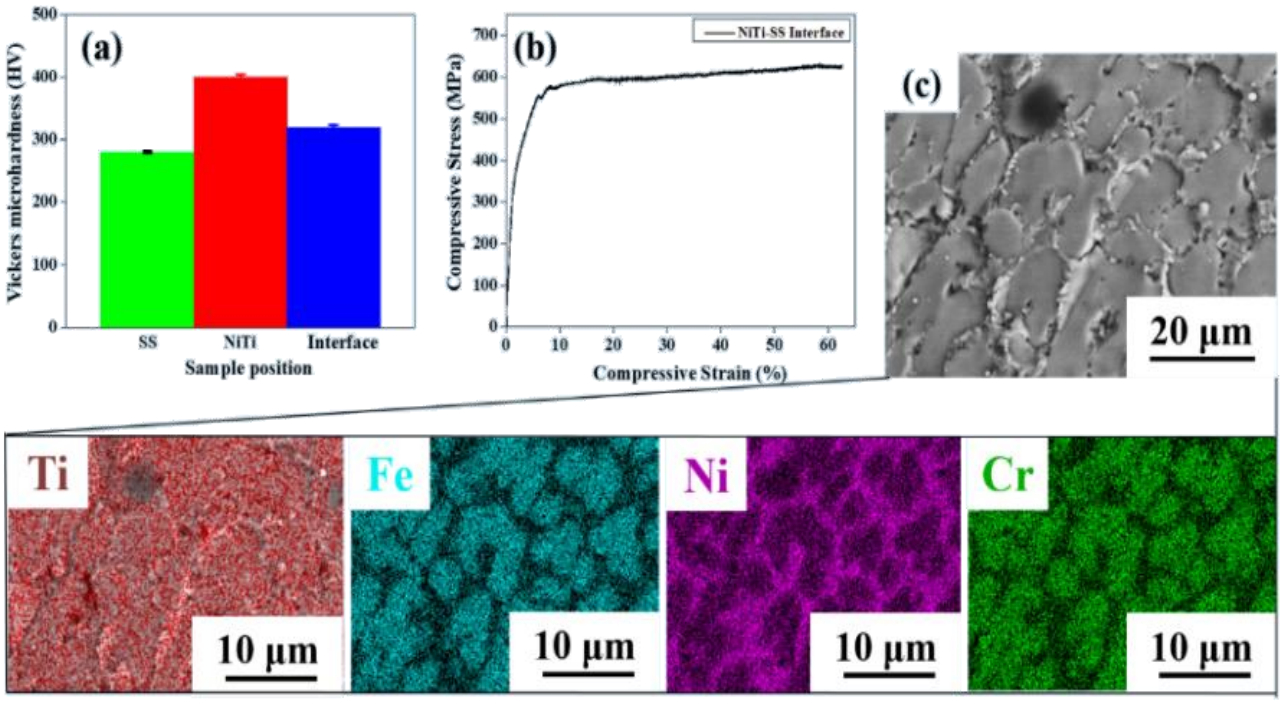

Fig. 4.13 Mechanical properties (a) Micro-hardness (b) Compression result, and (c) SEM fractography surface with elemental mapping

Fig. 4.14a displays the hardness test results for both bimetallic joint and base material, and the average micro-hardness value is higher for NiTiCu samples (485 HV). The hardness of the NiTi sample increased, and the most likely cause of this was the addition of copper which will cause precipitation in α-Ti [28]. The main factor contributing to the increase in micro-hardness brought by internal stress is the precipitate like $Ti(NiCu)_2$ that forms when Cu concentrations are higher [29]. The maximum hardness of the joints and embrittlement were caused by the mixing of Cu in the NiTi region. Higher micro-hardness values and their related engineering stress-strain curves for samples containing more than 10% Cu support the materials brittle nature, which is primarily caused by the development of Cu-based intermetallic compounds in fabricated joint [178-182]. However, the likelihood of excessively Ti-rich detrimental intermetallics forming was reduced due to the increased mixing and dissolution of Cu into the weld zone, which still permits the development of Cu-based intermetallics. Fig.4.14 (b), which shows the compressive result for the interface (NiTi-Cu) and NiTi. The compressive strength would decrease after Cu is added to NiTi due to the production of brittle intermetallics. The elasticity and ultimate strength were at their highest at the lowest percentage of Cu, and they steadily decreased as the Cu weight

percentage increased [180-181]. Fig. 4c shows fracture surface of the welded joints. In fusing zone, brittle-like failure features were seen. For NiTi-Cu weld, the fracture region features show smooth step patterns with cleavage-like structures (Fig.4.14c). This deterioration is an outcome of microstructural changes caused by the WAAM deposition process in the fusion zone, specifically due to Cu-based intermetallic compounds, which do not improve superelastic behaviour and are consequently associated with a decline in the mechanical properties of the constructed joints [180-181].

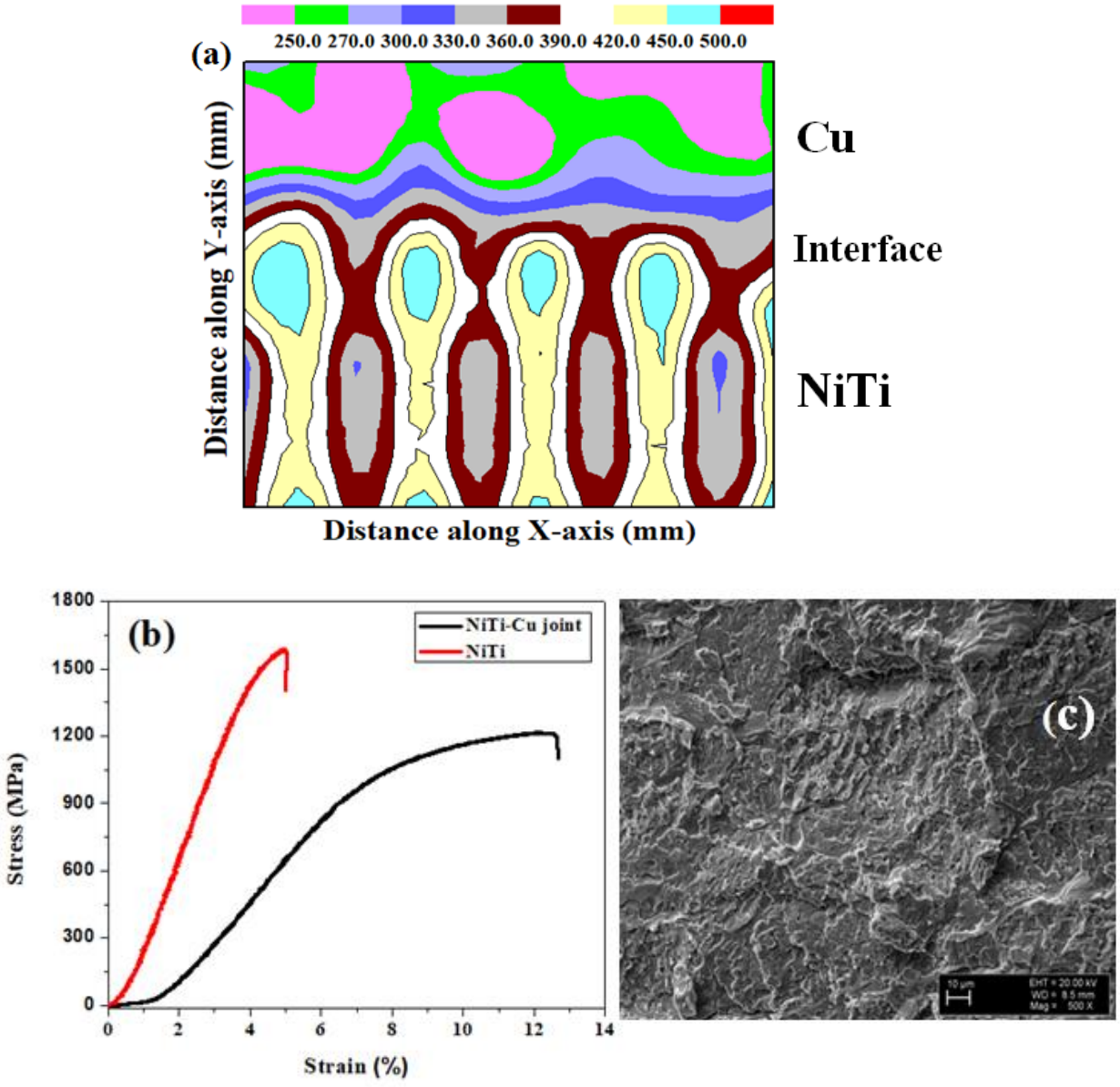

Fig.4.14 Mechanical Behaviour of Bi-metallic joint (a) Micro Hardness, (b) Compression strength (c) Fractography

4.3. 4 Actuation studies

Due to very low shape recovery observed in case of NiTi-SS it was not recorded and NiTi-Cu still need to examine for actuation studies in comng future.

In the ice bath, both materials were bent around a mandrel with a radius of 2 mm (in the martensite state). This results in a 25% bending deformation of the samples. After unloading, both samples were characterized by the same residual strain. Then, at room temperature, one side of the sample was fixed, and the other was connected to a load of 35 g (Fig.4.15). The Arduino relay circuit was used to control the heating and cooling of the samples for a 15-second duty cycle. The actuation response and dynamic displacement characteristics were investigated during the real-time experiment by applying a series of potentials with varying voltage and current with frequency to get their actuation response. A voltage of 5 V and a current of 4 Amp was used in the entire actuation study. Lab view was connected to the power supply. The samples were also heated on a hot plate to investigate the variation in bending angle due to heating.

The displacement vs. time curves obtained in real-time experiments is shown in Fig. 4.16(a), where zero displacements at t = 0 correspond to the location of the non-fixed pre-deformed sample at room temperature. From the figure, it can be seen that a displacement of 2.2 mm was found for the NiTi-Ti sample whereas a displacement of 1.5 mm was obtained for the NiTi sample. A Martensite detwinning and plastic strain occurred in the samples after preliminary deformation to 25% in the martensite stage. The two-way shape memory effect (TWSME) is usually generated as plastic strain causes the formation of oriented internal stress. During Joule heating, the strain recovers because of the reverse transformation from detwinned martensite to austenite (Fig. 4.16 a). Owing to the generation of the internal oriented stress during the previous deformation, strain rises during the forward change from austenite to detwinned martensite and during subsequent cooling. The load of 35 g that was applied to the sample was too small to affect the TWSME. Thus, the NiTi sample demonstrated the TWSME that is typical for the SMA. The strain variation in NiTi-Ti samples is typical for the NiTi-based bimetallic composited produced by explosion welding [166]. The martensite reorientation and plastic deformation in the NiTi layer occurs during preliminary deformation of the NiTi-Ti sample (bending around mandrel), whereas elastic and plastic deformation occurs in the Ti layer. On

subsequent heating, the strain recovery occurred in the NiTi layer, leading to the deformation of the Ti layer (as in counter body in actuators), and resulted in internal stress appearing in the NiTi-Ti sample. Following cooling under this stress, the detwinned martensite form increased strain and relaxation of tension. The stress generated during Ti layer deformation added up to the internal stress in the NiTi layer and turned more than the internal stress caused in the NiTi sample by plastic deformation. As a result, the strain variation in the NiTi-Ti sample during cooling and heating was found to be greater than in the NiTi sample. This is illustrated in Fig 4.16b, which shows the bending angle's relation to sample temperature. It can be seen in the Fig.4.16b that at all temperatures, the bending angle in the NiTi-Ti sample is 5 ^{o}C larger than in the NiTi sample, excluding a temperature of 140 ^{o}C at which this difference is 15 ^{o}C . The samples were subjected to a series of cycles in which they were heated by the current for a few seconds before being cooled to test the stability of the recoverable strain variation (Fig. 4.16). Both samples demonstrated the stable strain variation and the difference in strain between NiTi-Ti and NiTi samples kept during thermal cycling. Thus, this work results show that the NiTi-Ti bimetallic sample produced by WAAM demonstrates a good functional behaviour as observed in NiTi-based bimetallic composites fabricated by other techniques [167-168].

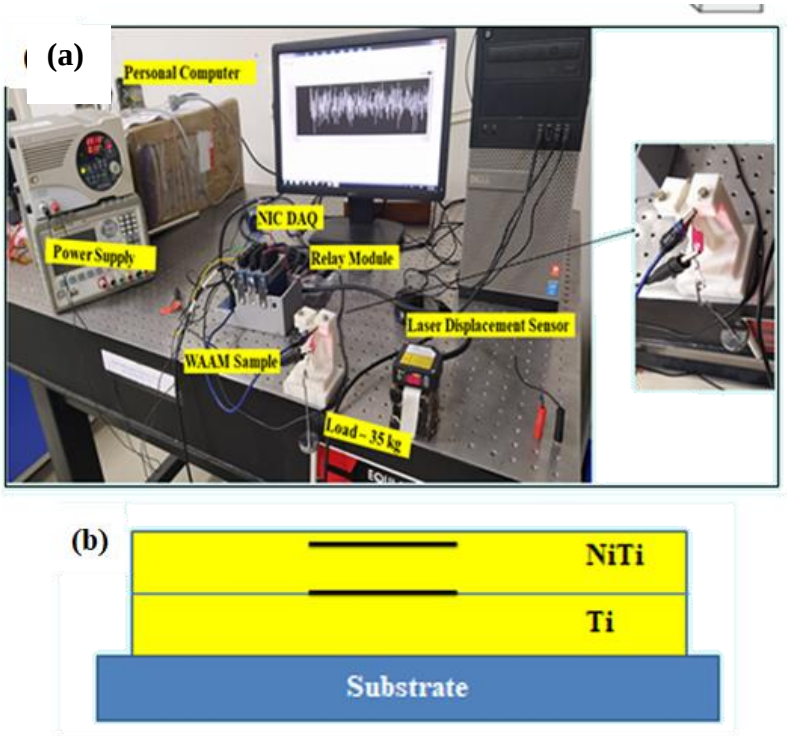

Fig 4.15 (a) Electrical actuation set-up and (b) Scheme of sample location

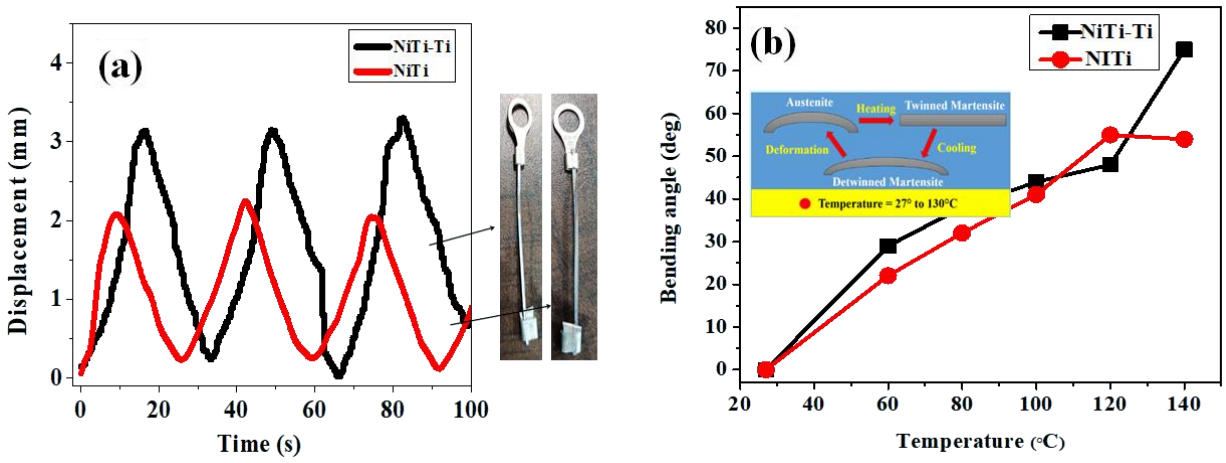

Fig. 4.16 Actuation studies of NiTi and NiTi-Ti joint (a) shape variation graph for electrical actuation (b) schematic for hot plate actuation and bending angle vs. temperature graph

Other two bimetallic samples (NiTi-SS and NiTi-Cu) did not show enough recovery to record due to various intermetallic phases formation which did not contributed in shape recovery behaviour.

4.4 Overall Comparison among bimetallic walls

Table 12 Comparaive studie among bimetallic walls fabricated through WAAM

Properties	NiTi-Cu	NiTi-SS	NiTi-Ti
Morphological Nature	Discontinuous with some waviness	Continuous with minimal waviness	Continuous with minimal waviness
Phase Transformation Properties	Austenite finish temperature: -3°C	Did not show any peak	Austenite finish temperature: 102°C
	Martensite finish	Did not show any	Martensite finish

	temperature: -110°C	peak	temperature: -37°C
Mechanical Properties	Ultimate compressive strength : 950 MPa	Ultimate compressive strength : 570 MPa	Ultimate compressive strength : 750 MPa
	Ductility: 4-6%	Ductility: 20-30%	Ductility: 6-8%
Hardness at Interface	HV 400	HV 485	HV 250-400
XRD Phase Results	Cu NiTi (B2) + $Ti_2(Ni,Cu)_3$+Ti $(Ni,Cu)_2$	$NiTi_3$+ $TiCr_2$+FeNi	NiTi (B2) + $NiTi_2$

Morphological nature: The morphology of the bimetallic walls can significantly impact their mechanical behavior. NiTi-Cu shows a discontinuous morphological nature with some waviness, which may result in stress concentrations and a decrease in mechanical properties. On the other hand, both NiTi-SS and NiTi-Ti exhibit a continuous nature with minimal waviness, which could lead to a more uniform stress distribution and a higher mechanical strength.

Phase transformation properties: The phase transformation properties of NiTi-Cu, NiTi-SS, and NiTi-Ti are crucial in determining their functional behavior, such as shape memory and superelasticity. NiTi-Cu has a lower austenite finish temperature (-3°C) and martensite finish temperature (-110°C) compared to NiTi-SS and NiTi-Ti. This means that NiTi-Cu can undergo the martensitic transformation at lower temperatures and can potentially have better shape memory properties. On the other hand, NiTi-SS and NiTi-Ti show higher austenite finish temperatures and martensite finish temperatures, indicating a better stability of the austenitic phase at higher temperatures. Please find the following explanation about comparative study among all bimetallic walls

Mechanical properties: The mechanical properties of the bimetallic walls, including ultimate compressive strength and ductility, are crucial in determining their load-bearing capacity and deformation behavior. NiTi-SS displays the highest ultimate compressive strength (570 MPa) among the three bimetallic walls, while NiTi-Cu shows the lowest ultimate compressive strength

(950 MPa). In terms of ductility, NiTi-SS shows the highest ductility (20-30%), while NiTi-Cu exhibits the lowest ductility (4-6%). These differences can be attributed to the microstructural features, including grain size, phase distribution, and interfacial morphology.

Hardness at interface: The hardness at the interface between the two materials is another critical property that affects the overall mechanical behavior of the bimetallic wall. NiTi-SS exhibits the highest hardness at the interface (HV 485), followed by NiTi-Cu (HV 400) and NiTi-Ti (HV 250-400). This difference in hardness can be attributed to the difference in interfacial morphology, interdiffusion, and precipitate formation.

XRD phase results: X-ray diffraction (XRD) analysis can provide valuable information about the phase composition and crystal structure of the materials. NiTi-Cu contains Cu NiTi (B2) + Ti2(Ni,Cu)3+Ti (Ni,Cu)2, NiTi-SS contains NiTi3+ TiCr2+FeNi, and NiTi-Ti contains NiTi (B2) + NiTi2. These differences in phase composition can influence the mechanical properties of the bimetallic walls, such as strength, ductility, and shape memory properties.

In summary, each of the three bimetallic walls has its unique characteristics, and the selection of one over the other would depend on the specific application requirements. For example, if the application requires a high ultimate compressive strength, then NiTi-SS would be the best choice. On the other hand, if the application requires a lower austenite finish temperature, then NiTi-Cu would be more suitable.

4.5 Summary

WAAM was used to produce a defect-free NiTi-Ti joint, and elemental mapping revealed the compositional transition from NiTi to Ti/SS/Cu

- According to X-ray diffraction studies, the NiTi phase was austenite at room temperature, and the martensitic transition was observable at high temperatures. Brittle intermetallic compounds formed at the interface resulted in increased hardness and brittle failure. NiTi-Ti sample demonstrated better shape recovery behaviour in comparison to NiTi sample due to the Ti layer inducing an additional stress.
- For NiTi-SS bimetallic structures, microstructural examinations showed that the solidification mode is primarily dendritic in both NiTi and SS sides. The presence of

brittle intermetallic compounds such as $TiCr_2$, FeNi, NiTi, $TiNi_3$ and Ti_2Ni are observed at the NiTi–SS joint interface. Higher hardness and brittle failure are observed at the interface due to the formation of brittle intermetallic compounds.

- Phase transformation temperature will also increase as a result of the addition of Cu to NiTi. Heat treatment will enhance the shape memory behavior for fabricated joint and for NiTi side which is shown by DSC result.

The work will be extended to the fabrication of large size walls to evaluate its mechanical properties to traction and analyze the effect of phases and deposition parameters on the properties. NiTi joints are widely-used implant materials to fabricate devices such as artificial bones and joints , guidewires , and stents . Investigation of the thermo-mechanical response and transformation properties for the NiTi/Cu joint under stress-loaded conditions still needs to be done. Pseudoelastic actuators can be connected to electromechanical systems using these joints. The ability to rapidly and easily connect electrically to a system would be beneficial for typical SMA actuators as well, particularly when non-standard geometries are used that preclude mechanical crimping.

Chapter 5

Fabrication of Copper Based Shape Memory Alloy (Elemental Powder) Through LPBF and Effect of HIP Temperature Increment On Microstructure and Mechanical Properties

5.1 Introduction

The Cu-based shape-memory alloy 82.95Cu-11.35Al-3.2Ni-3Mn (wt.%) was processed by Laser Powder Bed Fusion (LPBF) and the parameters were optimized to obtain compact, fully martensitic samples with a high relative density of up to 99%. In this study, elemental powder has been made through ball milling. The influence of the different power on the overall density, the defect distribution as well as the grain sizes was then analyzed. The processing technique has a strong influence on the degree of porosity and the distribution of the pores, the grain size as well as the grain morphology. In order to improve the density and mechanical properties of Cu alloys through the LPBF process, hot isostatic pressing (HIP) was utilized in this study. Cu-14Al-4Ni-3Mn SMA was fabricated through LPBF process and was chatacterized using Scanning electron microscopy (SEM), Differential scanning calorimetry, X-ray diffraction (XRD). Tensile strength and micro hardness tests were used to evaluate the mechanical behavior of produced parts.In this study denser, uniform without defect sample has been formed with elemental powder which shows maximum hardness of 590 HV, phase transformation temperature (A_s-160 and M_s-120) and tensile strength of 1550 MPa which is higher than other conventionally manufactured samples. After LPBF, HIP has also shown improvement in density and mechanical properties with respect to differen temperatures.

In this study, selective laser melting is used to process the shape-memory alloy 81.95Cu-11.35Al-3.2Ni-3Mn (wt.%) the first aim of this work is to systematically optimize the processing parameters of mechanical alloying for the production of homogenous CuAlNiMn powder. Microstructural and structural properties of LPBF fabricated parts have been studied with the help of SEM and XRD. In addition, mechanical properties have been also investigated using hardness and tensile test. HIP has been conducted for enhancement of density and mechanical properties of the LPBF fabricated sample.

5 .2 Experimental methodology

5.2.1 Mechanical Alloying (MA) for CuAlNiMn elemental powder

In the MA process, a QM-1F high-energy planetary ball mill with four stainless steel vials was used. Each vial contained hardened steel balls of different sizes (6, 10 and 20 mm in diameter). In this process, the ball-to-powder weight ratio (BPR) as 15:1 was utilized. The specification of elemental powders and the initial mixture were shown in Table 13. The mixture was then mechanically milled for 24 h at a speed of 40 rpm.

Table 13. Table showing the elemental powder used for the fabrication of Cu-based shape memory alloys using the selective laser melting process along with their size, purity, and concentration.

Elements	Size (mesh)	Purity (%)	Concentration (wt.%)
Copper (Cu)	200	99.99	81.95
Aluminium (Al)	200	99.99	11.85
Nickel (Ni)	200	99.99	3.2
Manganese (Mn)	200	99.99	3

5.2.2 Powder Properties

The particle size distribution (PSD) is a very important parameter to characterize the powder and its suitability affects the LPBF process (Fig.10.1a). As shown by Spierings et al. [182], for Fe and Ni powders, the PSD significantly affects both the surface quality and the mechanical properties of LPBF components. Regarding the approach of blending four elemental powders and generating a homogeneously distributed alloy, the PSD of all materials is of decisive importance. It should be noted that it is beneficial if the PSD of the two alloying components is similar to each other. Besides the aforementioned impact of the PSD on surface quality and mechanical part properties, it also significantly affects the flowability of a powder, which is an indicator for the application of a homogeneous powder layer [183]. The average size of the spherical powder particles was 40 ± 4 μm (Elemental powder). Furthermore, a large number of

satellite particles are observed in the prepared powder due to uneven particle size of all the elemental powders such as Cu, Al, Ni and Mn. Some of the satellite particles resulted from impingement between small and large particles. Other satellite particles are attributed to the strong inter-particle attractions (such as van der Waals force [183]) between fine powders that lead to a strong tendency towards cohesion and agglomeration [184]. Both of these two conditions could naturally lead to the agglomeration of powder and the formation of large powder clusters [185] as shown in Fig 5.1(b). The powder cohesion and agglomeration increase the equivalent powder size and constitute a large proportion of non-spherical particles in the powder feedstock. Therefore, it is easy to form irregularly shaped powder clusters and the inter-particle gap could hardly be filled during the LPBF process.

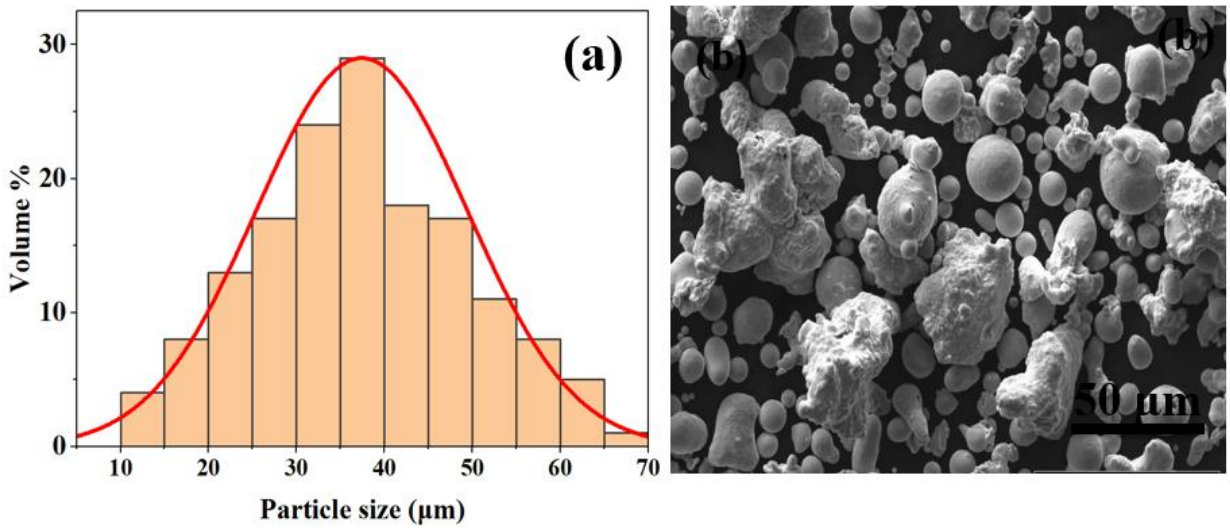

Fig.5.1 (a) Particle size distribution and (b) SEM results for powder

5.2.3 XRF Analysis

To detect the chemical composition of the powder mixture, X-ray fluorescence (XRF) analysis was conducted on the elemental powder mixture. The XRF analysis was performed using a RAM-30 μm analytical microprobe microscope at a voltage of 30 kV and a current of 1000 μA. The energy resolution is ~130 eV for Mn-Kα line. The source of the X-ray radiation was an X-ray tube with a Mo anode. Accordingly, the energy for the Kα-series X-ray radiation (with wavelength λ = 0.07107 nm) is equivalent to 2.8×10^{-15} J or 17.5 keV. The elemental powder

samples were prepared in a press mold at a pressure of 15 MPa. The Cu, Al, Mn, and Ni concentrations in the samples were calculated using the software “exact expert” developed by the “Scientific Instruments” JSC by the fundamental parameter’s method. Before the XRF analysis, the background spectrum was recorded to exclude the intensities of the elements fixed by the detector from the focusing system of the device. According to XRF results, the composition measured from the elemental powder mixture was tabulated in Table 14.

Table 2. XRF analysis measurement showing the concentration of the elements in the elemental mixture.

Table 14 XRF results for chemical composition

Elements	**Weight (%)**
Cu	81.95
Al	11.35
Ni	3.2
Mn	3

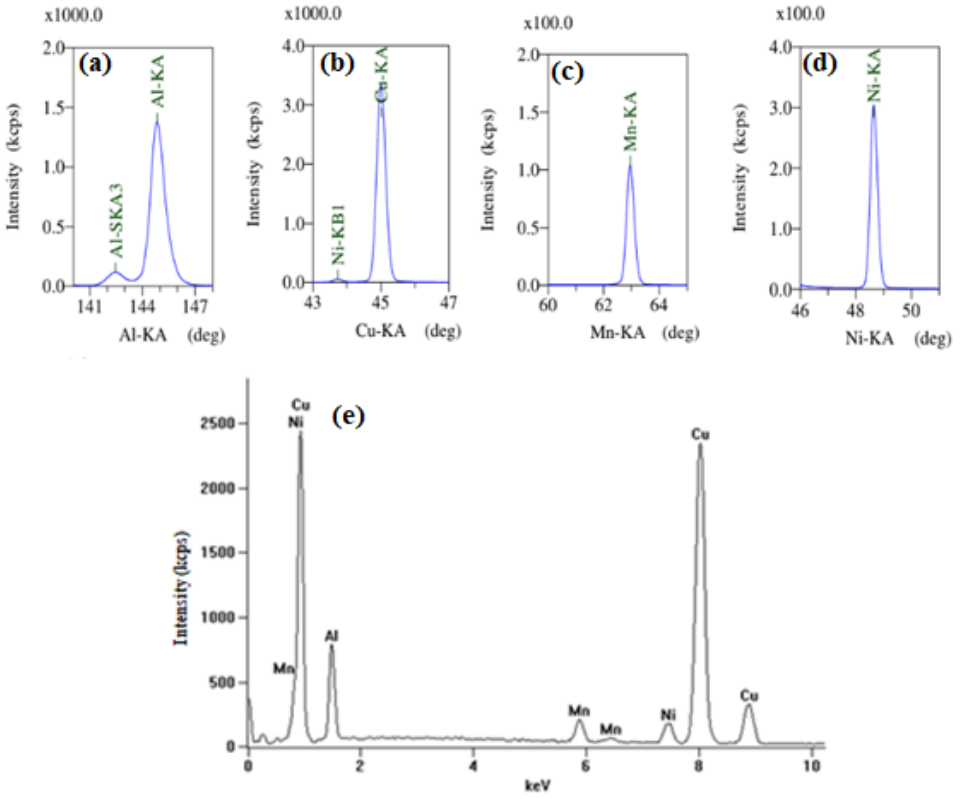

Fig.5.2XRF spectrum for (a) Al , (b) Cu, (c) Mn ,(d) Ni and (e) CuAlNiMn powder

5.2.4 XRD results

In order to identify phases in the powder, X-ray diffraction (XRD) analysis was carried out (Fig.5.3). X-ray diffraction (XRD) measurements of the powder were performed on a Rigaku UltimaIV diffractometer with monochromatic Cu Kα radiation (λ = 1.5406 Å). The intensities of diffraction peaks of Mn, Al and Ni are lower than that of Cu diffraction peaks because of their small amount in the overall composition. It is caused by the decrease of crystallite size and the increase of micro-strain due to high stresses involved during milling balls impacts [184]. Plastic deformation and interdiffusion of elements control the formation of phase [183-185], the mixing of elements is accelerated by diffusion of Al, Ni and Mn along dislocations of Cu solid solution [186].

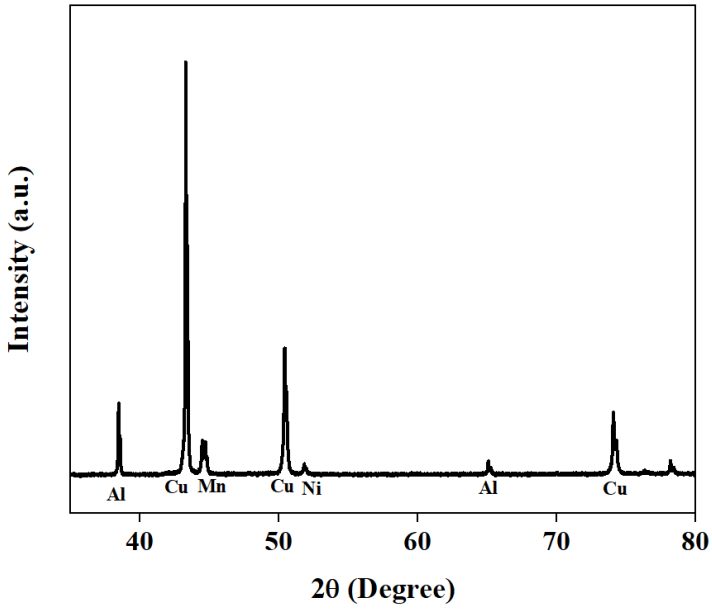

Fig. 5.3 X-Ray Diffraction graph for CuAlNiMn powder

5.3 Experimental Setup

Shape memory alloyed samples were fabricated with a Concept Laser m1- machine equipped with a Nd:YAG laser with 1064 nm wavelength and a maximum power of 700 W. CuAlNiMn cylindrical samples of 3 mm diameter with a length of 12 mm were fabricated, the following parameters were utilized: laser power: 300,350,400 W, scanning speed: 100 mm/s, layer thickness: 25 µm, hatch spacing: 120 µm, hatch overlap:30%, and a straight line hatch with a rotation of 90° between layers. The samples were made at room temperature, with a high purity argon gas circulated within the processing chamber to avoid any possible oxygen contamination throughout the operation. In order to establish the optimum parameters for bulk samples, which allow the production of dense samples, the laser power and the scanning speeds, were systematically varied. Combinations of laser power between 300, 350 and 400 W and scanning speeds 100, 200 and 300 mm/s were chosen at fixed track overlaps of 30%. LPBF system image has been already explained in section 1.2.3.1.

5.4 Results and discussion

5.4.1 Parameter optimization

The unevenness of the powder layer deposited on the build area can affect the size of the melt pool by changing the local heat absorption [184]. At locations where an abnormally large particle resides the laser fails to fully melt the particle and therefore leaves behind lack-of-fusion pores. The satellite and agglomeration of powder lead to the formation of the large powder cluster and poor powder flowability and subsequently forms the inter-particle gap left in the powder bed. In the LPBF process, these powder characteristics can cause uneven recoating and rough surface, which continued to accumulate, eventually forming internal defects such as lack-of-fusion or unfilled irregular shaped defects in parts. LPBF process for copper based alloy (up to 79% Cu content) is much more difficult than that for Fe and Ti alloys because of the higher reflectivity [186], as well as the higher thermal conductivity of the solidified metal material [187]. Since metals with high reflectivity and high thermal conductivity require more laser energy for melting, higher laser power and smaller laser-focused spots will be applied in order to increase laser energy density [185].

In this work, based on previously report power and scanning speed has been varied and optimized in the preliminary set of experiment later on based on the following microscopic results constant optimized speed has been used and power has been varied. Because due to high scanning speed delamination happened and also powder flowability was not good due to which getting uniform layer thickness at higher scanning speed that's why 100 mm/s speed has been chosen among all speeds. Based on a previously reported, power was kept in between 300 W to 400 W and scanning speed has been kept in between 100 to 300 mm/s [187]. However, further enhancements of the laser power at the maximum relative density result in excessive laser energy, which then results in a fall in the relative density. This is because of the following two reasons: (1) excessive laser energy input leads to thermal microcracks and micropores which are caused by residual stresses and thermal shrinkage [188]; (2) excessive laser energy input creates a thicker layer of semi-molten powder around the sample [188]. The thermal expansion caused by grain coarsening reduces the relative density of the Cu alloy [187]. Fig.5.5 shows optical microscopy images of fabricated sample in which cracks, pores and other defects is present which is due to the lower power and higher scanning speed leading to a decrease in molten pool size thereby boosting the formation of defects due to the incomplete bonding and un-melted powder [189-190]. At the maximum relative density, the laser provides enough power for full powder melting and metallurgical bonding with the elimination of keyhole pores [190].

Generally, this can be attributed from Fig.5.5, the incomplete melting of the powders owing to insufficient laser energy density input, which can increase the uneven viscosity of the liquid pool [191]. However, when the laser energy density is too high, it gives rise to microcracks and pores. The microcracks and pores formed at such low scanning speed and high laser power are believed to be the thermal cracks caused by thermal shrinkage. During the LPBF densification process, once the powder material becomes fully molten, shrinkage occurs rapidly. Higher speed is also not suitable because delamination or wrapping effect occurs due to poor bonding in between substrate and sample due to less energy obtained because of high reflectivity. Balling effect and delamination have been also observed during deposition due to lower energy input (as shown in Fig.5.4 a) but for higher power also reflectivity issues occur in the system and even it destroyed the laser mirror during deposition. From Fig.5.5, it has been observed that the best combination of power and speed is 350 w and 100 mm/sec respectively (Fig. 5 b). Based on our observation speed for all sample fabrication for further investigation was kept at 100 mm/s and power has been varied in between 300 to 400W.

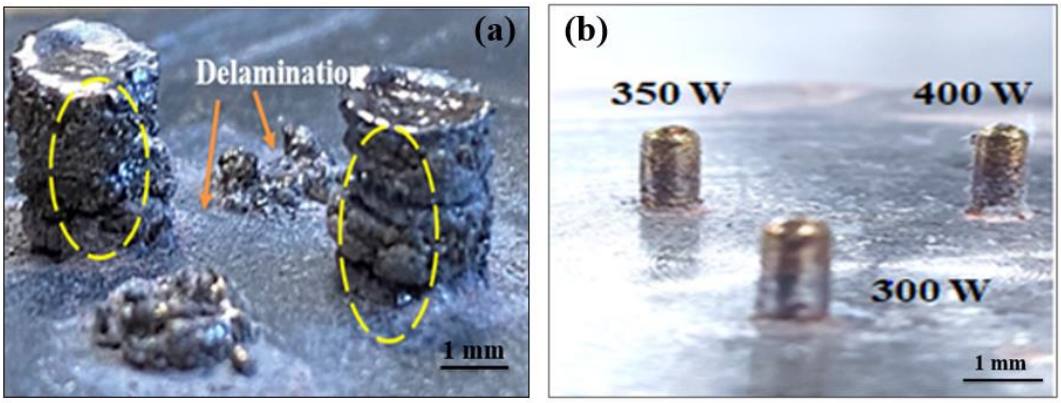

Fig. 5.4 (a)Deposited sample which shows balling and delamination and (b) sample deposited with different power

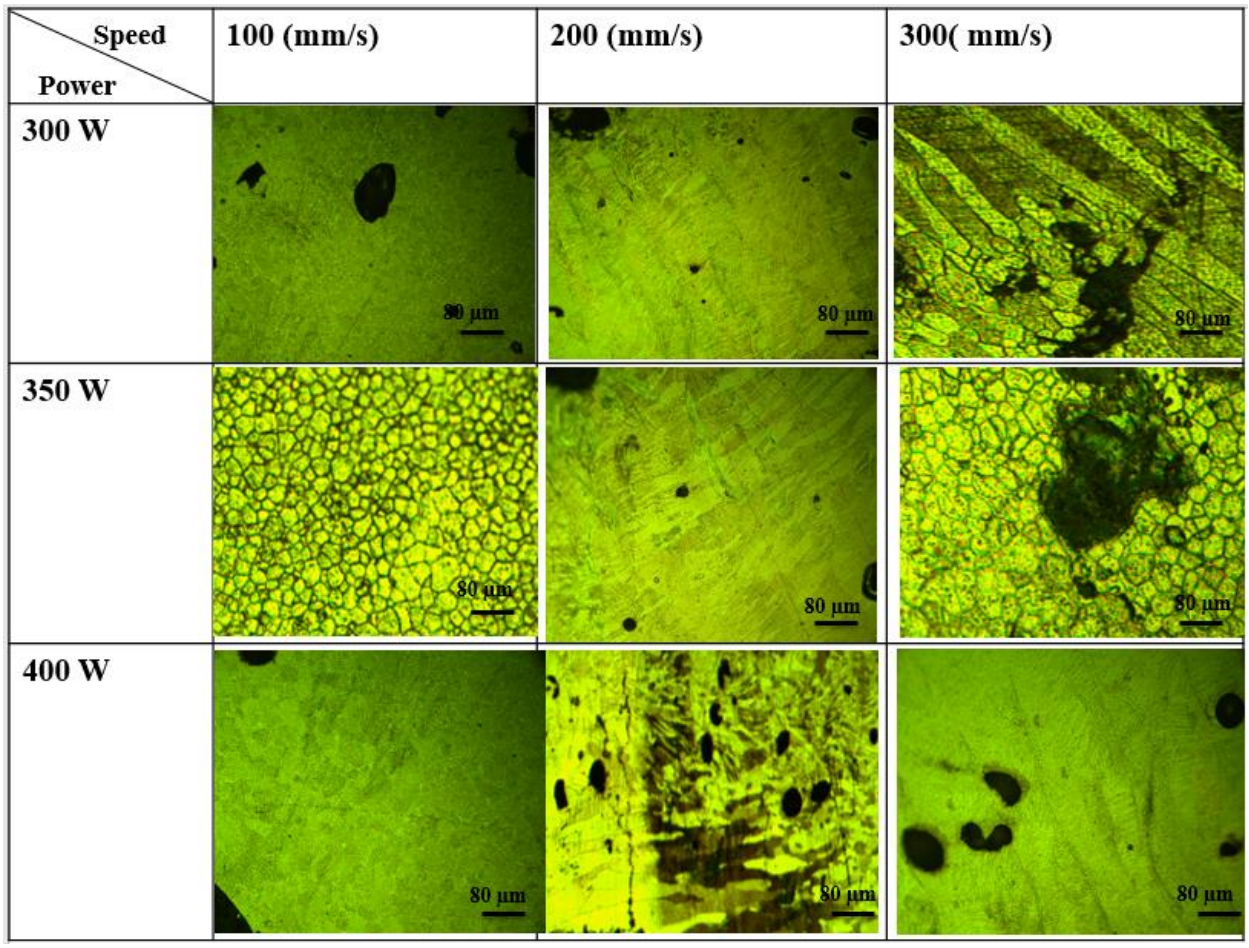

Fig. 5. 5 Sample fabricated at different speed and at different power

5.4.2. Density Measurement

Table 15 shows the results of X-ray Microscope/nano CT and relative densities of 82 % (processed with 300 W) and 99 % (350 W) for CuAlNiMn and 92 % (400 W) was found. The average size of the pores is shown in Table 15 for 300 W, 350 Wand 400 W, respectively. Porosity varies with laser power because of incomplete melting of powder at lower energy which will result in discontinuous molten pool. This makes it difficult to fully melt the powders between the adjacent tracks to form an effective overlap, resulting in the formation of incomplete fusion defects like pores and shrinkage porosity as shown in Fig.5.6. On the other hand, the molten pool becomes large if energy input is high, which causes powder denudation around the molten pool. The denudation process results in insufficient molten metal to fill the gap between

the adjacent tracks which leads to large pore formation. According to CT sample which has been fabricated at 350 W shows higher density in comparison to other two samples.

The achievable density increases with the increase of laser power as more energy are absorbed by the powder to facilitate full melting. However, at some point this energy begins to cause balling thereby reducing the relative density as shown in Fig.5.4 a. According to CT results with laser power increase, the porosity is reduced. However, higher energy inputs slightly decrease density (92 % to 82 %) since higher power will cause material vaporization and even attendant keyhole effect, when the vapor bubbles are trapped in the melt pools, then the defects will generate in solidified melt pools. Pore size was more for samples 300 W and 400 W in comparison to 350 W sample. Aspect ratio shows the 300 W sample shows larger pores in comparison to other two sample which is basically keyhole pores that formed due to the instability of the keyhole, which depends on the applied power [192]. The amount of lack of fusion was high for 300 W sample because of lower power and shrinkage porosity has been also found in 400 W sample which has been already explained in previous section (process parameter optimization) due to higher energy input.

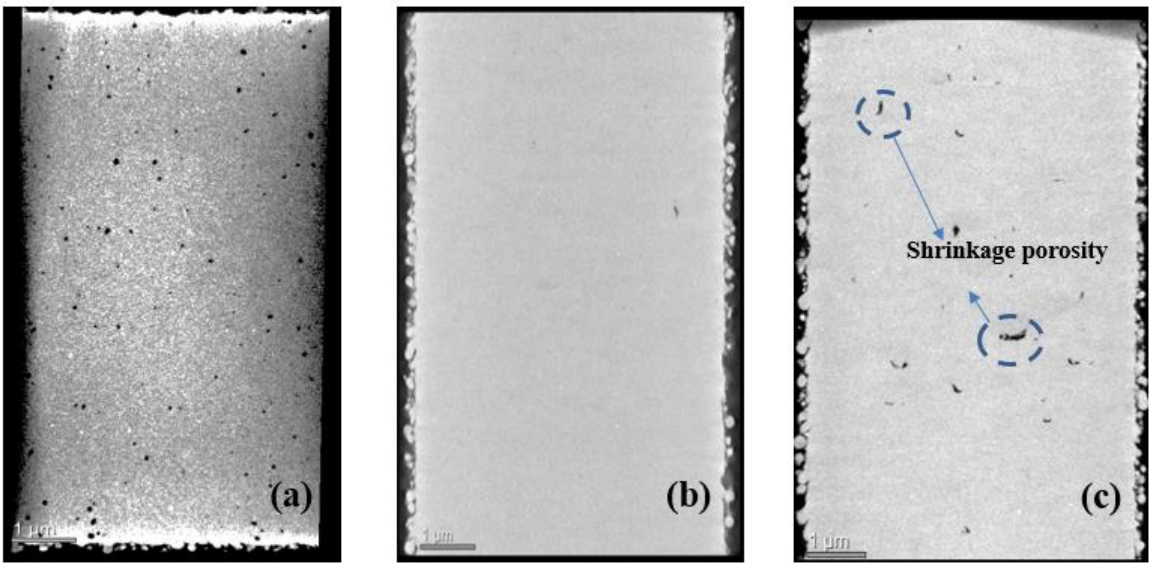

Fig.5.6 CT results for (a) 300 W , 100 mm/s, (b) 350 W, 100 mm/s and , (c) 400 W, 100 mm/s sample

Table.15 CT results for different power sample

Power	Scanning Speed (mm/s)	Pore size (μm)	Porosity %	Aspect ratio
300 W	100	12.53- 721.49	0.49	0.90
350 W	100	15.82-105.58	0.07	1
400 W	100	12.48-344.41	0.21	1

5.4.3 Microstructure Analysis

Fig.5. 7 shows SEM results of LPBF fabricated CuAlNiMn samples as a function of varying laser power. The low-magnification microstructure in Fig. 5. 7 shows the presence of columnar grains. However, at higher magnification, the presence of fine cellular microstructure can be observed for all three samples built using different laser powers. Some micropores are also observed in these three samples considered. Due to the presence of a high-temperature gradient and extremely high cooling rates observed during solidification for LPBF [193], the size of the cells is restricted to ~ 1.8 μm (350 W), 2.2 μm (300 W), and 3.2μm (400 W). These fine cellular structures are typical microstructures for the LPBF-processed samples, due to constitutional supercooling together with a high-velocity solidification [53-54]. For the sample fabricated with a lower energy density, irregularly shaped pores along with unmelted powder particles are observed, leading to lacking fusion pores. Reports have shown that a high laser energy input can lead to coarsening of the grains [193-195]. The grain size gets reduced by 36% and 24%, respectively for the LPBF samples fabricated with laser power of 300 W and 350 W as compared to the samples fabricated at the laser power of 400 W. This is because the cooling rate reduces with increasing the laser power (increasing energy density) leading to the formation of coarse grains. When a high laser power is employed, the cooling rate during LPBF is decreased, hence leading to an increase in both the cell and grain sizes [195]. In the present case, both columnar

and cellular structures are observed at different length scales as shown in Fig. 7. In addition, pores are also observed in these samples at both micron and sub-micron scales.

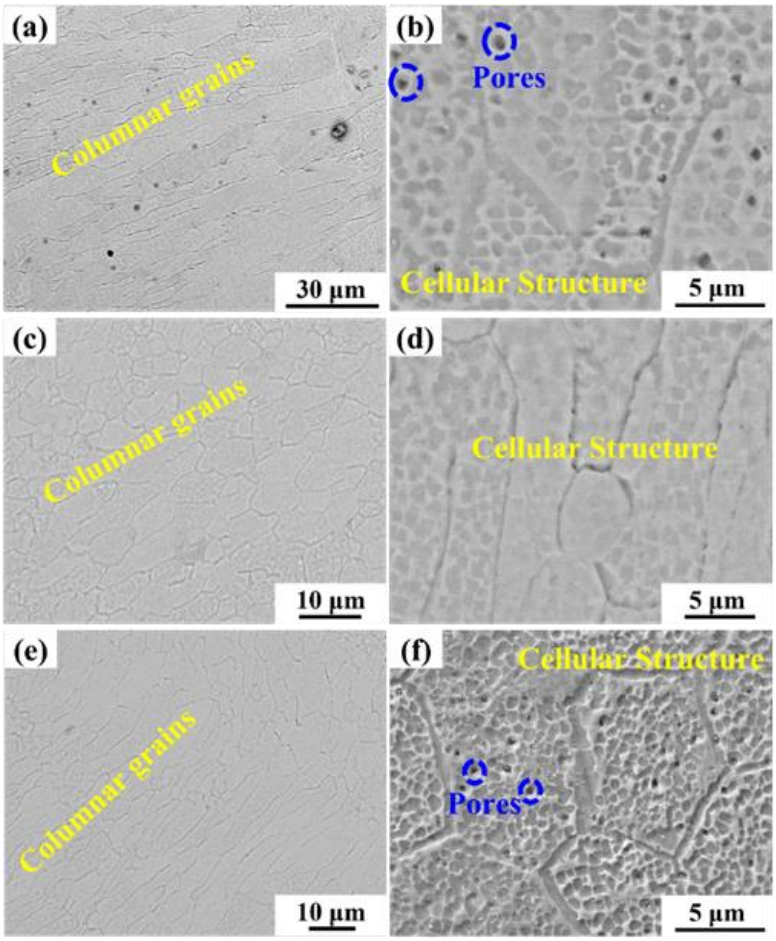

Fig.5.7 Scanning electron microscopy images of the selective laser melted Cu-based shape memory alloy fabricated as a function of varying laser power. (a) 300 W, (b) 350 W, and (c) 400 W

5.4.4 XRD analysis

Fig. 5.8 shows the XRD graph indicating the formation of monoclinic β' martensite (a = 0.443 nm, b = 0.530 nm, c = 1.278 nm and β = 95.8°, with space group P21/m) for all the samples [19]. For the sample fabricated using laser power of 350 W, Ni and Mn rich phases are formed, which is good for shape recovery as well for mechanical properties. The estimated value

of crystallite size is 15± 4 nm, 11 ±6 nm, and 7±2 nm for samples built with laser power of 400 W, 350 W, and 300 W, respectively. The crystallite size reduces with an increase in laser power, which is evident from the broadening of the peak. As can be seen, peak shift has been observed among all the samples which is primarily due to variations in the thermal strain as per the Braggs law [55-56]. But for higher laser power (400 W), the thermal shrinkage tends to generate and cause higher residual stress [57] due to high-temperature gradient, which is consistent with the result of XRD analysis.

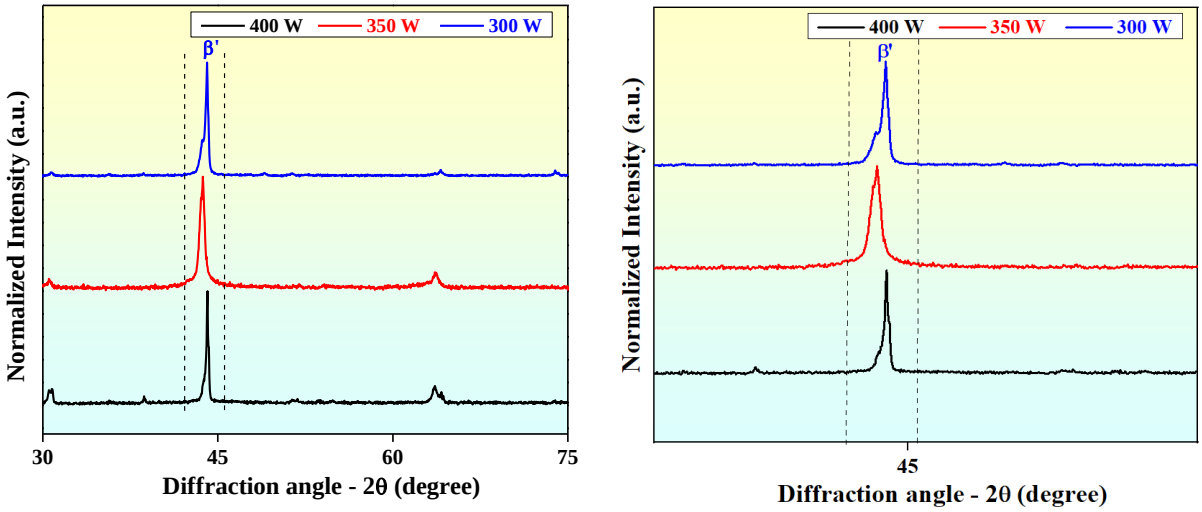

Fig.5. 8 XRD patterns for the LPBF fabricated CuAlNiMn SMA samples as a function of varying laser power.

5.4.5 Phase Transformation behavior

Fig.5.9 shows the DSC results for all the samples which have been fabricated at different laser power. According to DSC results, with increase of laser power, phase transformation will get enhanced because of grain size change and phases formed which involves Ni rich phases. The transformation peak will become sharp with respect to power change and also transformation temperature will get change. Phase transformation temperatures are changed by alternation of the stress levels [199].

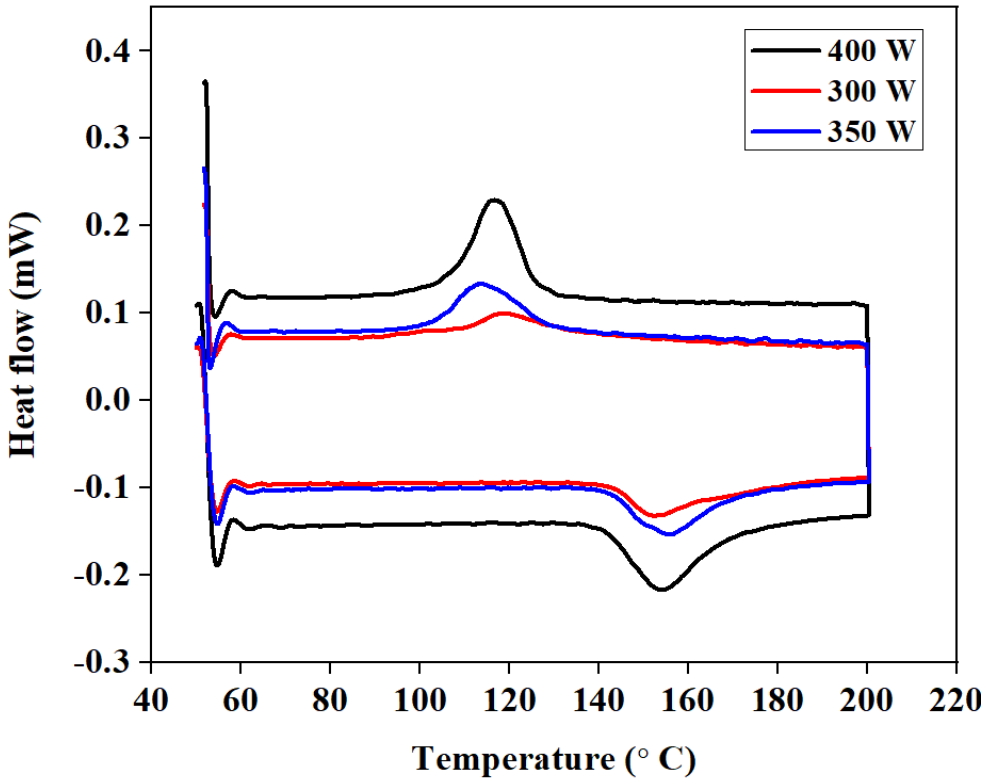

Fig. 5.9 DSC results of CuAlNiMn bulk samples at different laser power.

5.4.6 Hardness result

Fig.5.10 shows microhardness results of fabricated samples with changing laser power at different locations in sample (top, middle and bottom). The average microhardness values obtained from the LPBF specimens fabricated at a laser power of 350 W were found to be higher than those encountered in the other two specimens. When a higher laser power is used, the cooling rate decreases. Hence, the cell and grain size are increased resulting in lower hardness for samples built with laser power of 400 W. The coarsened microstructure reduced the hardness as per Hall–Petch relationship [198]. The preliminary microstructure analysis showed that although the lower laser power boosts the formation of submicron-sized grains, the macroscopic pore defects have a greater impact on hardness (ref Fig. 5.11). The implication is that the sample may collapse significantly when exposed to the stress and this is due to the lower densification at low laser energy density (ref. Fig. 5.11). The highest hardness values could be attributed to the

higher applied laser power, which enabled the efficient melt and fusion of CuAlNiMn powder particles. Considering the location of microhardness test, the bottom part shows better results due to higher heat dissipation to the substrate [198].

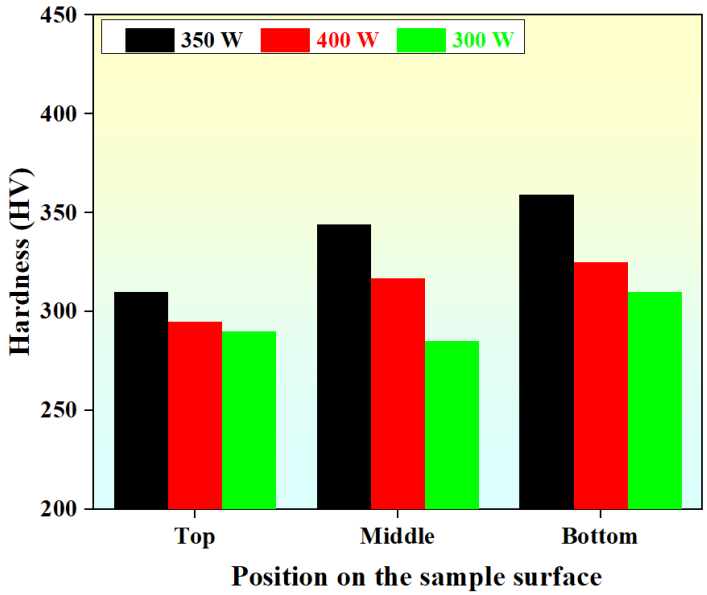

Fig. 5.10 Average microhardness plot for the LPBF built Cu-based SMA as a function of varying laser power taken at different locations.

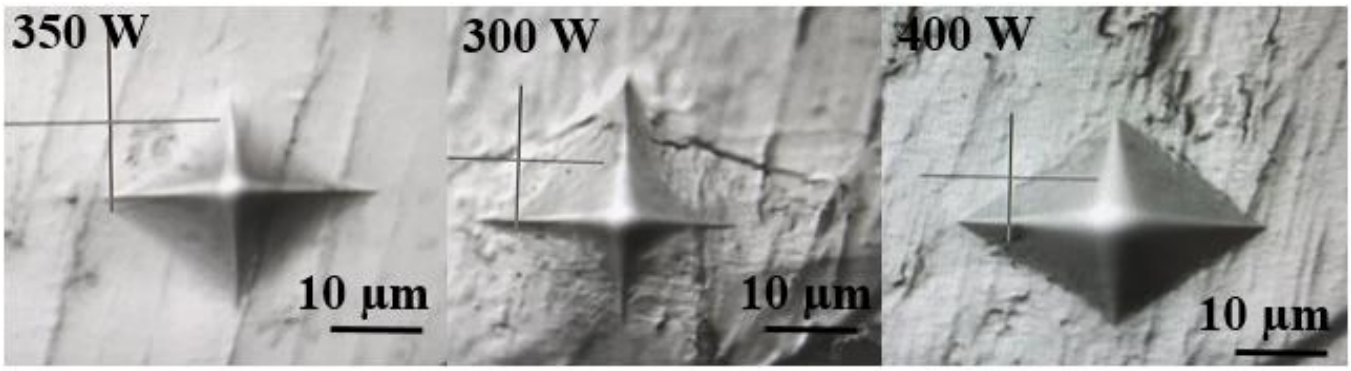

Fig. 5.11 Indentation image (a)350 W, (b) 300 W ,and (c)400 W

5.4.7 Tensile result

Stress-strain curves obtained from the tensile tests are displayed in Fig. 5.12. As can be seen, a high laser power resulted in strong metallurgical bonding of the LPBF alloy and high tensile strength. Maximum tensile strength of 380 MPa, 1550 MPa, and 1250 MPa is observed at laser power of 300 W, 350W and 400 W, respectively. The deformability in tension is slightly increased from 2.6± 0.9% (300 W) to 4.8 ± 0.6% (350 W) most likely due to the increased porosity. Lower laser power results in the agglomeration and these agglomerations resulted in discontinuous melting channels on the alloy surface, thereby forming a large number of micron-sized holes. These pores greatly reduce the density and tensile strength of the LPBF alloy. According to Hall-Petch relationship [198-199], in a certain range, the smaller the grain size results in higher yield strength, which makes the properties of LPBF fabricated alloy better than that of casting alloy [198-199]. This results in higher strength values for samples built using a laser power of 350 W. In general, it was observed that increased laser energy density leads to a softening behavior of the powder particles due to the extensive thermal energy. This results in an increase of the elastic modulus leading to higher strength for samples built with a laser power of 350W as compared to samples built with a laser power of 300 W [200].

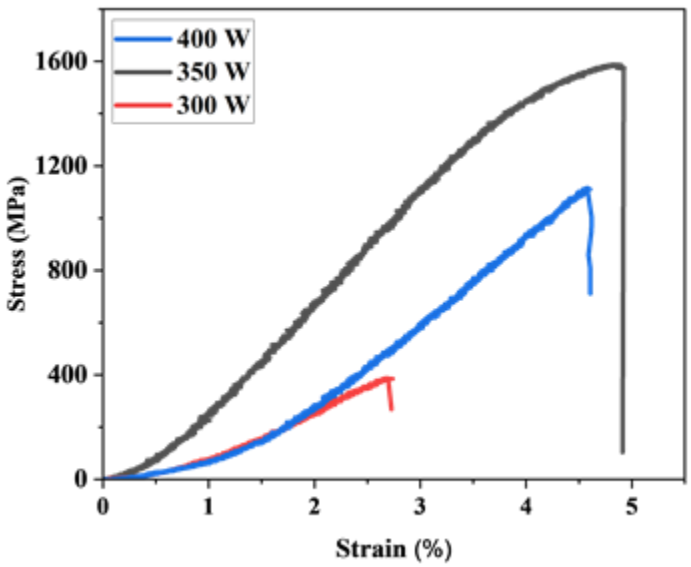

Fig.5.12 Tensile results for LPBF fabricated CuAlNiMn sample with changing laser power.

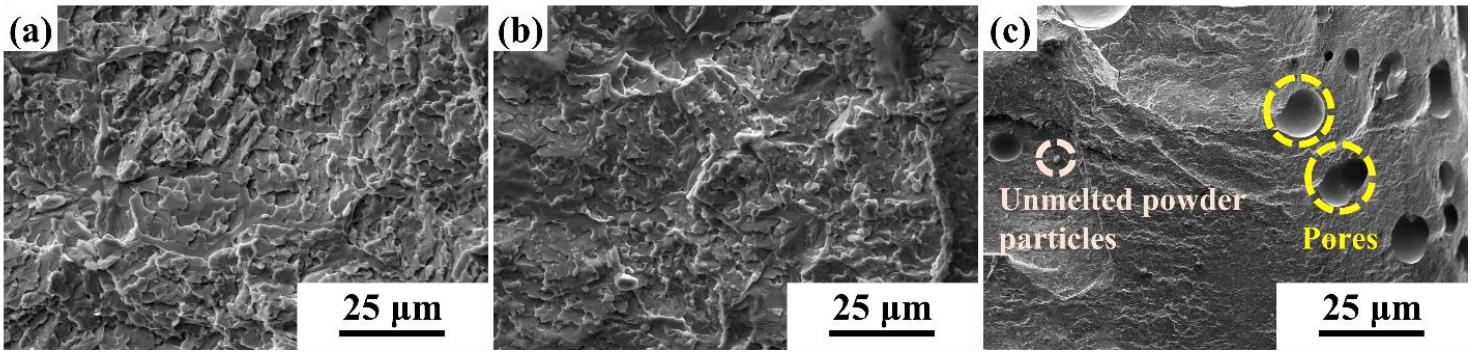

Fig. 5.13 Fractography of LPBF fabricated sample (a) 400 W, (b) 350 W and (c) 300 W

A fractographic analysis was carried out to unravel the possible fracture mechanisms. The results are depicted in Fig. 5.13, which shows images of the fractured surfaces of the different specimens. The images obtained exemplify that the samples present brittle fractures with the presence of cleavage surfaces. All samples display characteristics of brittle fracture, with the presence of porosity and cleavage surfaces. For Fig. 5.13(a) (b), the cleavage can be observed, and the intergranular characteristics are more accentuated for the 400 W sample due to the higher heat input and unmelted powder particles were present for 300 W due to lower laser power. Fig. 5.13 (a) shows a continuous porosity in the centre of the fracture surface, which was probably responsible for fracture initiation. Similar defects are observed on the whole fracture surface, which confirms the theory of crack propagation by linking defects. Fracture surfaces were observed with SEM and cleavage facets, cleavage steps, unmelted powder particles and pores were seen

5.5 HIP treatment

Sample 3 which has been fabricated at lower power (300 W) was used for these studies because of its low density in comparison to other samples. The HIP was done in a container-less fashion, as the fabricated parts were observed to not have any significant surface connected porosity that could affect the process. HIP process were conducted at temperature of 950° C, 1150 ,1250°C and pressure of 206.84 MPa (30,000 psi), for 2 hours in an Argon atmosphere . The temperature could then be raised to a slightly higher value as well, and an initial trial had been conducted at a

HIP temperature of 975°C held for four hours. However, this caused issues with remaining porosity. Hence, the temperature in the successful trial reported here was optimized from 950°C to 1250°C, with the hold time reduced to two hours to minimize grain growth.

5.5.1 Microstructure, Hardness and Tensile result after HIP

The results presented below show a general trend of an overall improvement in porosity as seen from porosity results Fig. 5.14. There is a visible consistency in the range of porosity in HIPed samples, irrespective of initial LPBF fabricated porosity with respect to temperature increment (Table.16). Densification of the Cu alloy increases as the HIP temperature increases above 900°C. The material porosity was only 1.5% before HIP and changed to 0.7% after HIP. When the HIP temperature was higher than the melting point of these eutectics, there would be a localized incipient melting phenomenon at the grain boundaries, ultimately leading to a reduction in the mechanical properties [20] from the aspect ratio it was visible that for higher temperature pores was not spherical and for 950 ° C it was spherical and tiny and also pore size diameter is also low for 950 °C sample which shows better mechanical properties and density.

Table.16 CT results for different temperature sample

Temperature (° C)	Pore size (μm)	Porosity %
1250	12.53- 621.49	0.51
1150	15.82-405.58	0.13
950	12.48-108.41	0.01

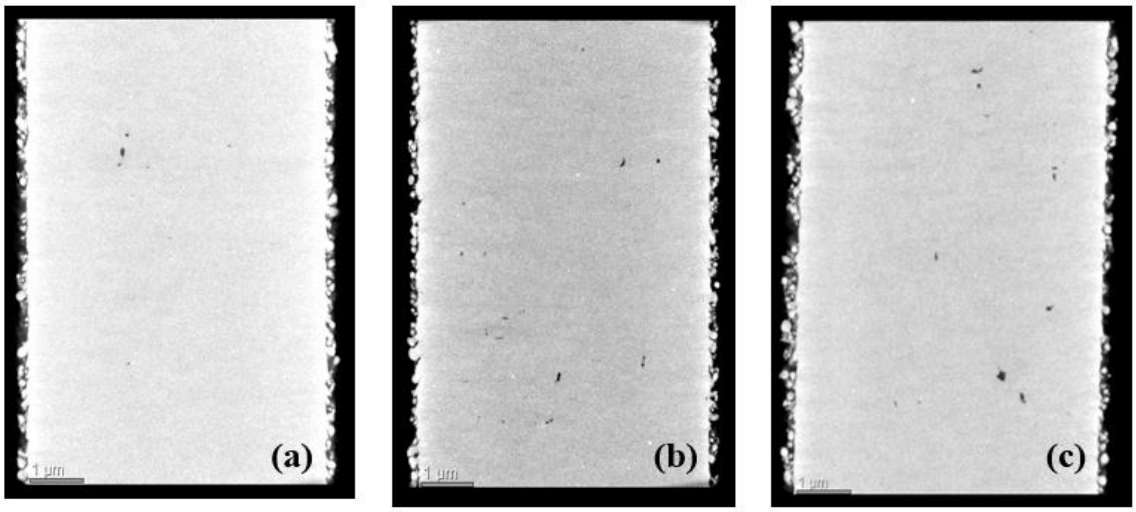

Fig. 5.14 CT result for different temperature sample (a) 950° C, (b) 1100° C and (c) 1250 ° C

Fig.5.15 shows SEM micrographs of LPBF fabricated samples after HIP process. The shrinkage porosity which is visible in without HIP treated sample (Fig. 5.15) is completely closed when HIP temperature is above 900 °C. The microstructure of Cu alloy after HIP becomes uniform; however, the thickness of the lamellae becomes thicker as HIP temperature increases. Grain size for 950°C is 30±7 µm and for 1100°C is 48±10 µm and for 1250°C is 79± 5 µm Grains size will increase as temperature increases, so the HIP temperature should be as low as possible in the premise of ensuring that the shrinkage is closed and for better mechanical property. HIPing under relatively high temperature make the grains coarsen which is shown in fig and thereby decreases the strength of the final article according to the Hall-Petch relation which is visible in SEM result.

Fig 5.16 (a) shows the hardness results after HIP which shows higher hardness in comparison to without HIP sample due to improved density and grain refinement because of the sample which has been HIPed at 950 °C shows higher hardness in comparison to other sample. Fig.5.16 (b) shows tensile results after HIP which also confirms higher tensile strength in comparison to without HIP sample. The higher strength for the alloy HIPed at a relatively lower temperature is ascribed to the finer grains and less influence of softening annealing. This increase in tensile strength is also largely attributed to the more ductile microstructure that is formed after HIP and

is influenced by the relief of residual stress and/or by a decrease in material porosity which is also associated with HIP treatments (Table 19) [20,30]. Grain growth, which can lead to a reduction in yield strength and toughness, is greater at higher temperatures [24]. One can find that due to the extremely fine microstructure of LPBF parts, an HIP treatment above the solubility temperature of CuAlNiMn lead to microstructural coarsening because of the dissolving of grain boundaries. This results in reduced strength, although the density is significantly lower [197-200].

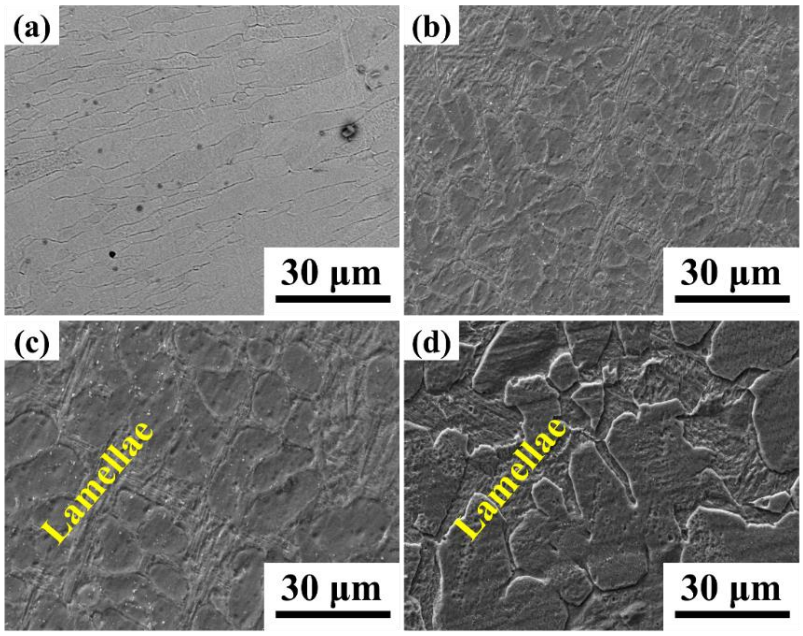

Fig. 5.15 SEM Images for (a) without HIP, (b, c and d) after HIP (950 °C, 1100 °C and 1250 °C)

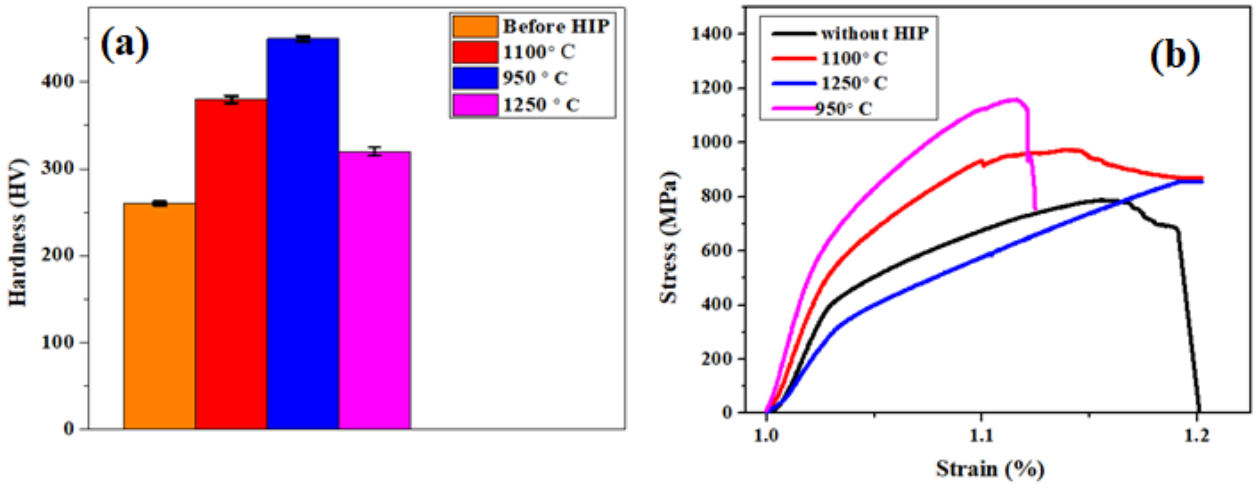

Fig.5.16 (a) Hardness result after HIP and (b) tensile result after HIP

5.6 Summary

In this study, the shape-memory alloy 81.95Cu-11.35 Al-3.2Ni-3Mn (wt.%) was processed by selective laser melting and Elemental powder has been prepared through ball milling.Power has been optimized between 300 W-400 W and it has been observed that lower power will leave a lack of fusion pores along with unmelted powder in the cavity and higher power will also increase and the grain size as well as thermal shrinkage. So the optimized power 350 W shows higher density and there are no obvious voids, inclusions and un-melted particles. Sample deposited at 350 W has shown higher density without any defect.

Ni rich phases formed in sample which has been fabricated at 350 W and residual stress was also less. Hardness and strength were also high for 350 W sample due to good metallic bonding, finer grain and higher density. After LPBF process HIP has been used and temperature has been optimized for higher density

The pores completely disappear when HIP temperature is at or higher than 950 °C. However, grains keep on growing as HIP temperature increases. Considering the effect of HIP temperature on the densification and microstructure, 950 °C is an appropriate HIP temperature for CuAlNiMn alloy in this case. This research will open the path of fabricating SMA based smart structures like tool clamping SMA ring which will act as a passive damper that takes up the heat and actuates itself thereby reduces vibrations and provide dampening effect in high speed

machining in real time applications. This research can be helpful reducing the cost which is high in case of powder based system because of prealloyed powder in comparison to wire based additive manufacturing system. Along with cost, properties enhancement experiments can also be performed easily which depends on composition percentage of different elements

Chapter 6

Conclusion and Future scope

6.1 Conclusion

In this study, a NiTi-based porous structure was successfully deposited using the WAAM process, which is challenging due to the high instability of the melt pool, heat accumulation, distortion, and higher residual stress resulting in humping, depressions, ripples, and hairline cracks. A systematic approach was used to control these issues, and the following findings were concluded:

- Parameters affecting NiTi deposition were optimized to get uniform and thinner section through WAAM.
- Laser marking on the titanium substrate reduced surface roughness and increased contact angle due to a change in surface energy. Laser marking during WAAM deposition led to a maximum wall width reduction of 45%, and laser marking after each layer helped with mechanical properties and shape recovery behavior studies due to grain refinement and Ni-rich phase formation.
- Interlayer delay was varied and optimized for NiTi fabrication through WAAM, and it was observed that with an increase in interlayer delay from 10 to 30 seconds, the density of WAAM constructed wall constructions increased. Higher interlayer delay (30 s) helped additively built NiTi walls have a more appealing surface finish with less visible surface oxidation, better microstructure, improved hardness, and increased strength. Shape recovery increased with an increase in interlayer delay due to variations in stress pattern and grain size reduction, which were observed from XRD and SEM results.
- Interpass temperature was also controlled and optimized for NiTi, and 200°C was found to be the optimal parameter. Temperature caused a change in viscosity, which was a reason behind the higher width without interpass temperature control samples. Ni-rich phase was found in lower interpass samples according to the phase diagram, which enhanced phase transformation temperature and shape recovery behavior. Hardness and strength also increased due to finer grain formation for lower interpass temperatures.

- NiTi-based porous structures were successfully fabricated through WAAM with the help of all process conditions and parameter optimization.

In addition, bimetallic structures were successfully fabricated through WAAM for the first time by joining NiTi with stainless steel, titanium, and copper. The following important findings were observed:

- The change from NiTi to Ti's composition for bimetallic joint was shown through elemental mapping. X-ray diffraction studies revealed that the NiTi phase was austenite at room temperature and martensitic at high temperatures. An increase in hardness and brittle failure was caused by brittle intermetallic compounds that were generated at the interface. Because the Ti layer introduces additional stress, NiTi-Ti samples showed superior shape recovery behavior than NiTi samples.
- The bimetallic NiTi-SS structure demonstrated that both the NiTi and SS sides' primary solidification mode is dendritic. At the NiTi-SS joint interface, brittle intermetallic compounds such as TiCr2, FeNi, NiTi, TiNi3, and Ti2Ni were found. Brittle intermetallic compounds occur at the contact, resulting in higher hardness and brittle failure.
- Phase transformation temperature also increased as a result of the addition of Cu to NiTi. Heat treatment enhanced the shape memory behavior for the fabricated joint and for the NiTi side, as shown by DSC results.

In addition to the above, power-based LPBF was used for Cu-based shape memory integrated structures. The shape-memory alloy 81.95Cu-11.85 Al-3.2Ni-3Mn (wt.%) was processed by selective laser melting, and elemental powder was prepared through ball milling. Process parameters were also optimized. 350 W and 100 mm/s were the optimized parameters, which showed higher hardness, density, and strength compared to other samples. Lower power left lack of fusion pores along with unmelted powder in the cavity, and higher power increased grain size.

6.2 Future scope

- In terms of a geometrical point of view: External cooling effect and cooling rate variation should investigate for shape memory alloy fabrication through WAAM.
- Porous structure has been successfully fabricated in this work but in future their mechanical properties and thermo-mechanical behavior should be investigated.

- Triply periodic minimal surfaces (TPMS) structures with angular struct should be fabricated in future. These porous structures best mimic the nature of bone as they are continuous through space, are periodic in three different directions, demonstrate bone-like mass transport properties, and partition the space into two sub-spaces by a nonintersecting two-sided surface
- Dissimilar joining of Nickel-titanium (NiTi) alloy with other metallic alloys can be used to widen the applications of NiTi for developing artificial bones and joints, guidewires, and stents. So in coming future, bimetallic strucure shoud be fabricated and their functioning can be studied for various engineering applications
- Actuation studies should be performed for CuAlNiMn samples for their use in vibration dampers in real time applications

6.3 Proposed Application

Investigation and modeling of different relationships among monitored parameters like, vibration, temperature, cutting force, vibration with tool degradation, SMA damping ,and product quality:

The vibrations generated during machining operation which may be due to use of worn-out tool or tool-workpiece interface result in degradation in the quality of part produced. To test the feasibility of fabricated part along with its outcome on tool and workpiece, we will employ this ring on turning operation. Single point cutting tool will be used for further investigations. This experiment aims at testing and validated proposed methodology as a vibration damper.

An experimental setup consisting of turning operation with and without proposed SMA ring will be developed. Existing turning machines will be used for the same. The following two types of the test will be done:

(1) Cutting tool life test of multiple samples without SMA ring

(2) Cutting tool life test of multiple samples with SMA ring

These tests will be conducted at multiple sets of operating conditions like, speed feed, depth of cut, coolant, workpiece and tool material combinations, etc.

The following data will be monitored:

- Vibration
- Temperature
- Cutting force
- Tool wear after some cuts
- Surface roughness after some cuts

As the machining starts, vibration or heat generation can be felt in the workpiece. SMA ring fitted over workpiece actuates itself and dissipates the heat. An infrared sensor will be used for sensing this temperature change. By reading the infrared light coming off an object, this sensor can sense between -95 and 720ºf (-70 to 382.2°C). This principle will be used during machining in which temperature change will showcase the actuation of shape memory alloy. We will make wireless communication between circuit and our Smartphone or PC.

A dynamometer will be mounted between tool and workpiece table to measure the cutting forces in three orthogonal directions. Also to calculate the vibration in turning operation, accelerometer is mounted on the workpiece.

All the data from various sensors will be acquired by Data Acquisition system and the reading will be in terms of voltage. This data will then be used to detect tool degradation and quality of process involved. Prognostics models will be developed to relate tool degradation with online monitored parameters, product quality and SMA actuation or damping effect. The relationship will be useful in providing real-time inputs for tool replacement, and dynamic process control.

The quality of machined surface will be investigated with a surface finish measuring instrument. A microscopy system will be utilized to quantify the degradation of cutting tool.

Advantageous characteristics of a real time monitoring include:

i) Live monitoring of SMA damping as the temperature detects reaches transformation temperature
ii) Intelligence in machining
iii) Dynamic process control

iv) Prognostics of cutting tool

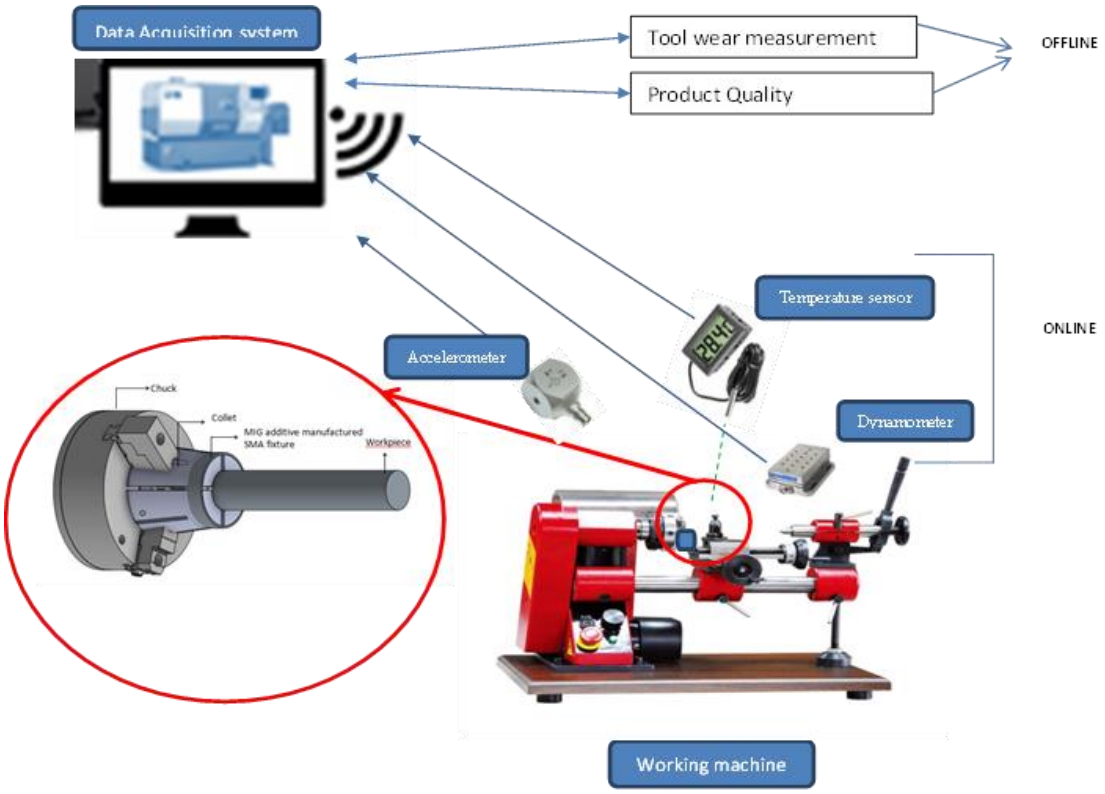

Figure 6.1: Intelligent Planning of proposed system

Chapter 7

References

[1] L. Petrini, F. Migliavacca, Biomedical Applications of Shape Memory Alloys, J. Metall. 2011 (2011) 1–15. https://doi.org/10.1155/2011/501483.

[2] M. Brojan, D. Bombač, F. Kosel, T. Videnič, Shape memory alloys in medicine Material, RMZMater.Geoenvironment.,55(2008)173–189.

[3] C. K Otsuka, C.M Wayman, Shape Memory Materials, 1998.

[4] J. Ma, I. Karaman, R.D. Noebe, High temperature shape memory alloys, 55 (2010) 257–315. https://doi.org/10.1179/095066010X12646898728363.

[5] D.A. Miller, D.C. Lagoudas, Thermomechanical characterization of NiTiCu and NiTi SMA actuators: Influence of plastic strains, Smart Mater. Struct. 9 (2000) 640–652. https://doi.org/10.1088/0964-1726/9/5/308.

[6] Nematzadeh, F., Sadrnezhaad, S. K., Kokabi, A. H., Razani, M., & Mohagheghi, A. H. (2014). Effect of material properties on the mechanical performance of nitinol esophageal stent: Finite element analysis. In Materials Science Forum (Vol. 773, pp. 9-17). Trans Tech Publications Ltd.

[7] Lagoudas, D. C. (Ed.). (2008). Shape memory alloys: modeling and engineering applications. Springer Science & Business Media.

[8] H. Ma, C. Cho, Feasibility study on a superelastic SMA damper with re-centring capability, Mater. Sci. Eng. A. 473 (2008) 290–296. doi:10.1016/j.msea.2007.04.073.

[9] Alaneme, K. K., & Okotete, E. A. (2016). Reconciling viability and cost-effective shape memory alloy options–A review of copper and iron based shape memory metallic systems. Engineering Science and Technology, an International Journal, 19(3), 1582-1592.

[10] S. Lee, Seung-Kook Ro, Jong-Kweon Park, 2016, Performance evaluation of a shape memory alloy tool holderfor high-speed machining, Int J Adv Manuf Technol, 84, 717– 725

[11] L. Petrini and F. Migliavacca, “Biomedical Applications of Shape Memory Alloys,” J. Metall., vol. 2011, no. Figure 1, pp. 1–15, 2011, doi: 10.1155/2011/501483.

[12] V. Gopal, “Design Engineering of Nitinol based Medical Devices,” pp. 1–16, 2009, [Online]. Available: http://www.hcltech.com/white-papers/medical-devices/design-engineering-nitinol based-medical-devices.

[13] N. B. Morgan, “Medical shape memory alloy applications - The market and its products,” Mater. Sci. Eng. A, vol. 378, no. 1-2 SPEC. ISS., pp. 16–23, 2004, doi: 10.1016/j.msea.2003.10.326.

[14 N. B. Morgan, “Medical shape memory alloy applications - The market and its products,” Mater. Sci. Eng. A, vol. 378, no. 1-2 SPEC. ISS., pp. 16–23, 2004, doi: 10.1016/j.msea.2003.10.326.

[15] D. J. Hartl and D. C. Lagoudas, “Aerospace applications of shape memory alloys,” Proc. Inst. Mech. Eng. Part G J. Aerosp. Eng., vol. 221, no. 4, pp. 535–552, 2007, doi: 10.1243/09544100JAERO211.

[16] D. Quan and X. Hai, “Shape Memory Alloy in Various Aviation Field,” Procedia Eng., vol. 99, pp. 1241–1246, 2015, doi: 10.1016/j.proeng.2014.12.654

[17] M. Bashir, C. F. Lee, and P. Rajendran, “Shape memory materials and their applications in aircraft morphing: An introspective study,” ARPN J. Eng. Appl. Sci., vol. 12, no. 19, pp. 5434–5446, 2017

[18] N. Gangil, A. N. Siddiquee, and S. Maheshwari, “Towards applications, processing and advancements in shape memory alloy and its composites,” J. Manuf. Process., vol. 59, no. September, pp. 205–222, 2020, doi: 10.1016/j.jmapro.2020.09.048.

[19] E. T. F. Chau, C. M. Friend, D. M. Allen, J. Hora, and J. R. Webster, “A technical and economic appraisal of shape memory alloys for aerospace applications,” vol. 440, pp. 589–592, 2006, doi: 10.1016/j.msea.2006.02.201

{20] K. Weinert and V. Petzoldt, "Machining of NiTi based shape memory alloys," Materials Science and Engineering: A, vol. 378, pp. 180-184, 2004.

[21] Elahinia M. Shape memory alloy actuators: design, fabrication, and experimental evaluation. Hoboken, New Jersey: John Wiley and Sons; 2015.

[22] Elahinia M et al. Manufacturing and processing of NiTi implants: a review. Prog Mater Sci 2012;57(5):911–46.

[23] Zeng, Z., Cong, B. Q., Oliveira, J. P., Ke, W. C., Schell, N., Peng, B., ... & Ao, S. S. (2020). Wire and arc additive manufacturing of a Ni-rich NiTi shape memory alloy: Microstructure and mechanical properties. Additive Manufacturing, 32, 101051.

[24] Wang, J., Pan, Z., Yang, G., Han, J., Chen, X., & Li, H. (2019). Location dependence of microstructure, phase transformation temperature and mechanical properties on Ni-rich NiTi alloy fabricated by wire arc additive manufacturing. Materials Science and Engineering: A, 749, 218-222.

[25] Biffi, C. A., Fiocchi, J., Valenza, F., Bassani, P., & Tuissi, A. (2020). Selective laser melting of NiTi shape memory alloy: Processability, microstructure, and superelasticity. Shape Memory and Superelasticity, 6(3), 342-353.

[26] Saedi, S., Moghaddam, N. S., Amerinatanzi, A., Elahinia, M., & Karaca, H. E. (2018). On the effects of selective laser melting process parameters on microstructure and thermomechanical response of Ni-rich NiTi. Acta Materialia, 144, 552-560.

[27] Zhao, C., Liang, H., Luo, S., Yang, J., & Wang, Z. (2020). The effect of energy input on reaction, phase transition and shape memory effect of NiTi alloy by selective laser melting. Journal of Alloys and Compounds, 817, 153288.

[28] Baran, A., & Polanski, M. (2018). Microstructure and properties of LENS (laser engineered net shaping) manufactured Ni-Ti shape memory alloy. Journal of Alloys and Compounds, 750, 863-870.

[29] Hamilton, R. F., Bimber, B. A., & Palmer, T. A. (2018). Correlating microstructure and superelasticity of directed energy deposition additive manufactured Ni-rich NiTi alloys. Journal of Alloys and Compounds, 739, 712-722.

[30] Tan, C., Li, S., Essa, K., Jamshidi, P., Zhou, K., Ma, W., & Attallah, M. M. (2019). Laser Powder Bed Fusion of Ti-rich TiNi lattice structures: Process optimisation, geometrical integrity, and phase transformations. International Journal of Machine Tools and Manufacture, 141, 19-29.

[31] Hamilton, R. F., Bimber, B. A., Andani, M. T., & Elahinia, M. (2017). Multi-scale shape memory effect recovery in NiTi alloys additive manufactured by selective laser melting and laser directed energy deposition. Journal of Materials Processing Technology, 250, 55-64.

[32] Farhang, B., Ravichander, B. B., Venturi, F., Amerinatanzi, A., & Moghaddam, N. S. (2020). Study on variations of microstructure and metallurgical properties in various heat-affected zones of SLM fabricated Nickel–Titanium alloy. Materials Science and Engineering: A, 774, 138919.

[33] Moghaddam, N. S., Saghaian, S. E., Amerinatanzi, A., Ibrahim, H., Li, P., Toker, G. P., ... & Elahinia, M. (2018). Anisotropic tensile and actuation properties of NiTi fabricated with selective laser melting. Materials Science and Engineering: A, 724, 220-230.

[34] Lu, B., Cui, X., Feng, X., Dong, M., Li, Y., Cai, Z., & Jin, G. (2018). Direct rapid prototyping of shape memory alloy with linear superelasticity via plasma arc deposition. Vacuum, 157, 65-68.

[35] Lee, J., & Shin, Y. C. (2019). Effects of composition and post heat treatment on shape memory characteristics and mechanical properties for laser direct deposited nitinol. Lasers in Manufacturing and Materials Processing, 6(1), 41-58.

[36] Mentz, J., Bram, M., Buchkremer, H. P., & Stoever, D. (2006). Improvement of mechanical properties of powder metallurgical NiTi shape memory alloys. Advanced engineering materials, 8(4), 247-252.

[37] Herderick, E. (2011, October). Additive manufacturing of metals: A review. In Mater. Sci. Technol. Conf. Exhib (Vol. 2, No. 2011, pp. 1413-1425).

[38] Elahinia, M. H., Hashemi, M., Tabesh, M., & Bhaduri, S. B. (2012). Manufacturing and processing of NiTi implants: A review. Progress in materials science, 57(5), 911-946.

[39] Karamooz-Ravari, M. R., Andani, M. T., Kadkhodaei, M., Saedi, S., Karaca, H., & Elahinia, M. (2018). Modeling the cyclic shape memory and superelasticity of selective laser melting fabricated NiTi. International Journal of Mechanical Sciences, 138, 54-61.

[40] Bhavar, V., Kattire, P., Patil, V., Khot, S., Gujar, K., & Singh, R. (2017). A review on powder bed fusion technology of metal additive manufacturing. Additive manufacturing handbook, 251-253.

[41] Frazier, W. E. (2014). Metal additive manufacturing: a review. Journal of Materials Engineering and performance, 23(6), 1917-1928.

[42] Xiong, J., Li, Y., Li, R., & Yin, Z. (2018). Influences of process parameters on surface roughness of multi-layer single-pass thin-walled parts in GMAW-based additive manufacturing. Journal of Materials Processing Technology, 252, 128-136.

[43] Herzog, D., Seyda, V., Wycisk, E., & Emmelmann, C. (2016). Additive manufacturing of metals. Acta Materialia, 117, 371-392.

[44] Qi, Z., Cong, B., Qi, B., Sun, H., Zhao, G., & Ding, J. (2018). Microstructure and mechanical properties of double-wire+ arc additively manufactured Al-Cu-Mg alloys. Journal of Materials Processing Technology, 255, 347-353.

[45] Martina, F., Mehnen, J., Williams, S. W., Colegrove, P., & Wang, F. (2012). Investigation of the benefits of plasma deposition for the additive layer manufacture of Ti–6Al–4V. Journal of Materials Processing Technology, 212(6), 1377-1386.

[46] Zeng, Z., Cong, B. Q., Oliveira, J. P., Ke, W. C., Schell, N., Peng, B., ... & Ao, S. S. (2020). Wire and arc additive manufacturing of a Ni-rich NiTi shape memory alloy: Microstructure and mechanical properties. Additive Manufacturing, 32, 101051.

[47] Wang, J., Pan, Z., Yang, G., Han, J., Chen, X., & Li, H. (2019). Location dependence of microstructure, phase transformation temperature and mechanical properties on Ni-rich NiTi alloy fabricated by wire arc additive manufacturing. Materials Science and Engineering: A, 749, 218-222.

[48] Khorasani, A. M., Goldberg, M., Doeven, E. H., &Littlefair, G. (2015). Titanium in biomedical applications—properties and fabrication: a review. Journal of Biomaterials and Tissue Engineering, 5(8), 593-619

[49] Singh, S., Subramaniam, K., Chittora, N., Brolin, A., &Palani, I. A. (2020). Studies on development of NiTi-integrated optical fiber sensor and its life cycle behavior. Journal of Intelligent Material Systems and Structures, 31(6), 869-881.

[50] B. Dong, Z. Pan, C. Shen, Y. Ma, H. Li, Fabrication of copper-rich Cu-Al alloy using the wire-arc additive manufacturing process, Metall. Mater. Trans. B 48B (2017) 3143e3151.

[51] C. Shen, Z. Pan, Y. Ma, D. Cuiuri, H. Li, Fabrication of iron-rich FeAl intermetallics using the wire-arc additive manufacturing process, Addit. Manuf.7 (2015) 20-26.

[52] C. Shen, M. Reid, K.D. Liss, Z. Pan, Y. Ma, D. Cuiuri, S. van Duin, H. Li, Neutron diffraction residual stress determinations in Fe3Al based iron aluminide components fabricated using wire-arc additive manufacturing (WAAM), Addit. Manuf. 29 (2019) 100774.

[53] B. Wu, Z. Pan, D. Ding, D. Cuiuri, H. Li, Effects of heat accumulation on microstructure and mechanical properties of Ti6Al4V alloy deposited by wire arc additive manufacturing,Addit.Manuf.23(2018)151-160,

[54] Brandl, E., Schoberth, A., & Leyens, C. (2012). Morphology, microstructure, and hardness of titanium (Ti-6Al-4V) blocks deposited by wire-feed additive layer manufacturing (ALM). Materials Science and Engineering: A, 532, 295-307.

[55] J. Wang, X. Lin, J. Wang, H. Yang, Y. Zhou, C. Wang, Q. Li, W. Huang, Grain morphology evolution and texture characterization of wire and arc additive manufactured Ti-6Al-4V, J. Alloys Compd. 768 (2018) 97-113.

[56] J. Wang, Z. Pan, G. Yang, J. Han, X. Chen, H. Li, Location dependence of microstructure, phase transformation temperature and mechanical properties on Ni-rich NiTi alloy fabricated by wire arc additive manufacturing, Mater. Sci. Eng., A 749 (2019) 218-222.

[57] Z. Zeng, B.Q. Cong, J.P. Oliveira, W. C Ke, N. Schell, B. Peng, Z.W. Qi, F.G. Ge, W. Zhang, S.S. Ao, Wire and arc additive manufacturing of a Ni-rich NiTi shape memory alloy: microstructure and mechanical properties, Addit. Manuf. (2020).

[58] Knezović, N., &Topić, A. (2018, June). Wire and arc additive manufacturing (WAAM)–A new advance in manufacturing. In International Conference "New Technologies, Development and Application" (pp. 65-71). Springer, Cham.

[59] Ou, W., Wei, Y., Liu, R., Zhao, W., & Cai, J. (2020). Determination of the control points for circle and triangle route in wire arc additive manufacturing (WAAM). Journal of Manufacturing Processes, 53, 84-98.

[60] Venturini, G., Montevecchi, F., Scippa, A., & Campatelli, G. (2016). Optimization of WAAM deposition patterns for T-crossing features. Procedia CIRP, 55, 95-100.

[61] Liu, L., Huang, R., Song, G., &Hao, X. (2008). Behavior and Spectrum Analysis of Welding Arc in Low-Power YAG-Laser–MAG Hybrid-Welding Process. IEEE Transactions on plasma science, 36(4), 1937-1943.

[62] Yang, D., He, C., Zhang, G. 2016. Forming characteristics of thin-wall steel parts by double electrode GMAW based additive manufacturing. Journal of Materials Processing Technology, 227, 153-160.

[63] Näsström, J., Brueckner, F., & Kaplan, A. F. (2019). Laser enhancement of wire arc additive manufacturing. Journal of Laser Applications, 31(2), 022307.

[64] Zhang, and S. S. A & Ao, S. S. 2020. Wire and arc additive manufacturing of a Ni-rich NiTi shape memory alloy: microstructure and mechanical properties. Additive Manufacturing, 32,101051.

[65] C. Haberland, H. Meier, J. Frenzel, On the properties of Ni-rich NiTi shape memory parts produced by selective laser melting, in: Proceedings of the ASME 2012 Conference on Smart Materials, Adaptive Structures and Intelligent Systems SMASIS 2012, September 19-21, 2012, Stone Mountain, Georgia, USA, 2012, pp. 1-8.

[66] B. Dong, Z. Pan, C. Shen, Y. Ma, H. Li, Fabrication of copper-rich Cu-Al alloy using the wire-arc additive manufacturing process, Metall. Mater. Trans. B 48B (2017) 3143-3151.

[67] Wang J, Lin X, Wang J et al. Grain morphology evolution and texture characterization of wire and arc additive manufactured Ti-6Al-4V. J. Alloys Compd.2018;, 768 : 97-113.

[68] Zhou X, Zhang H, Wang, G, et al. Three-dimensional numerical simulation of arc and metal transport in arc welding based additive manufacturing. International Int. J. Heat Mass Transf.2016; 103: 521-5.

[69] Zhao H, Zhang G, Yin Z, et al. 3D dynamic analysis of thermal behavior during single-pass multi-layer weld-based rapid prototyping. J. Mater. Process. Technol 2011; , 211(3):488-495.

[70] Antonysamy A A, Microstructure, texture and mechanical property evolution during additive manufacturing of Ti6Al4V alloy for aerospace applications.University of Manchester (United Kingdom);2012 .

[71] Singh, S., Jinoop, A. N., Tarun Kumar G. T. A, et al. Effect of Interlayer Delay on the Microstructure and Mechanical Properties of Wire Arc Additive Manufactured Wall Structures.J. Mater. 2021; 14(15): 4187

[72] Geng H, Li J , Xiong J, et. al Optimisation of interpass temperature and heat input for wire and arc additive manufacturing 5A06 aluminium alloy, Sci. Technol. Weld. Join. 2017; 22:472–483.

[73] Davis A E, Kennedy J R, Ding J, et al. The effect of processing parameters on rapid-heating β recrystallization in inter-pass deformed Ti-6Al-4V wire-arc additive manufacturing, Mater. Charact. 2020;163 :110-298.

[74] Denlinger E R, Heigel J C, Michaleris, P, et al. ,Effect of inter-layer dwell time on distortion and residual stress in additive manufacturing of titanium and nickel alloys. J. Mater. Process. Technol 2015; 215:123-131.

[75]K. Otsuka, C.M.E. Wayman, Shape Memory Materials, Cambridge University Press, Cambridge,1998.

[76] Lojen, G., Gojić, M., & Anžel, I. (2013). Continuously cast Cu–Al–Ni shape memory alloy–Properties in as-cast condition. Journal of Alloys and Compounds, 580, 497-505.

[78] J.H. Zhu, The Effect of Rapid Solidification on Martensitic Transformation in a Copper-based Shape Memory Alloy (Ph.D dissertation), Department of Materials engineering, University of Wollongong,Wollongong,1994.

[79] K. Otsuka, X. Ren, Recent developments in the research of shape memory al- loys, Intermetallics 7(5) (1999)511–528.

[80] M. Colić, R. Rudolf, D. Stamenković, I. Anzel, D. Vucević, M. Jenko, V. Lazić, G. Lojen, Relationship between microstructure , cytotoxicity and corrosion properties of a Cu–Al–Ni shapememoryalloy,ActaBiomater.6(1)(2010) 308–317.

[81] M. Gojić, L.Vrsalović, S.Kožuh, A.Kneissl,I.Anžel, S.Gudić, B.Kosec, M. Kliškić, Electrochemical and microstructural study of Cu–Al–Ni shape memory alloy,J.Alloy.Compd.509(41)(2011)9782–9790.

[82] E.M. Mazzer, C.S.Kiminami,C.Bolfarini,R.D.Cava,W.J.Botta,P.Gargarella, Thermodynamic analysis of the effect of annealing on the thermalstability of a Cu–Al–Ni–Mn shapememoryalloy,Thermochim.Acta608(2015)1–6.

[83] Y.Sutou, T.Omori, J.J.Wang, R.Kainuma, K.Ishida, Characteristics of Cu–Al– Mn-based shape memory alloys and their applications, Mater.Sci. Eng.:A378 (1–2) (2004)278–282.

[84] J. Dutkiewicz, T. Czeppe, J. Morgiel, Effect of titanium on structure and Martensic transformation in rapidly solidified Cu–Al–Ni–Mn–Ti alloys, Mater.Sci. Eng.: A273–275(0)(1999)703–707.

[85] D.A. Porter, Phases Transformations in Metals and Alloys, Chapman &Hall, London 1991, pp.249–251.

[86] Silva, M. R., Gargarella, P., Gustmann, T., Botta Filho, W. J., Kiminami, C. S., Eckert, J., & Bolfarini, C. (2016). Laser surface remelting of a Cu-Al-Ni-Mn shape memory alloy. Materials Science and Engineering: A, 661, 61-67.

[87] De Damborenea, J. (1998). Surface modification of metals by high power lasers. Surface and Coatings Technology, 100, 377-382.

[88] da Silva, M. R., Gargarella, P., Gustmann, T., Botta Filho, W. J., Kiminami, C. S., Eckert, J., & Bolfarini, C. (2016). Laser surface remelting of a Cu-Al-Ni-Mn shape memory alloy. Materials Science and Engineering: A, 661, 61-67.

[89] J.F.Ready, Handbook of Laser Materials Processing, Springer-Verlag,Berlin Heidelberg NewYork2001,pp.223–280.

[90] Dasgupta, R. (2014). A look into Cu-based shape memory alloys: Present scenario and future prospects. Journal of Materials Research, 29(16), 1681-1698.

[91]T.B. Massalski, C.G. Woychik, Modelling of the nucleation temperature of the f.c.c. Phase competing with glass formation in Cu-Ti alloys, Acta Met .33(10) (1985)1873–1886.

[92]J.D.Majumdar, R.Galun, B.L.Mordike, I.Manna, Effect of laser surface melting on corrosion and wear resistance of a commercial magnesium alloy, Mater.Sci. Eng. A61 (2013)119–1292003.

[93] Laakso, P., Riipinen, T., Laukkanen, A., Andersson, T., Jokinen, A., Revuelta, A., & Ruusuvuori, K. (2016). Optimization and simulation of SLM process for high density H13 tool steel parts. Physics Procedia, 83, 26-35.

[94] X.H. Lin, W.L.Johnson, Formation of Ti-Zr-Cu-Ni bulk metallic glasses,J.Appl. Phys. 78(1995)6514–6519.

[95] M.F. Ashby, K.E. Easterling, The transformation hardening of steel surfaces by laser beams-I.hypo-eutectoidsteels,ActaMet.32(11)(1984)1935–1948.

[96] Yadroitsev, I., & Smurov, I. (2010). Selective laser melting technology: from the single laser melted track stability to 3D parts of complex shape. Physics Procedia, 5, 551-560.

[97] Y.Sutou, T.Omori, J.J.Wang, R.Kainuma, K.Ishida, Characteristics of Cu–Al– Mn-based shape memory alloys and their applications, Mater.Sci. Eng.:A378 (1–2) (2004)278–282.

[98] Wang, G., Lang, L. H., Yu, W. J., Huang, X. N., & Li, F. (2016). Influences of hot-isostatic-pressing temperature on the microstructure, tensile properties and tensile fracture mode of 2A12 powder compact. Acta Metallurgica Sinica (English Letters), 29(10), 963-974.

[99] Mehrpouya, M., Gisario, A., & Elahinia, M. (2018). Laser welding of NiTi shape memory alloy: A review. Journal of Manufacturing Processes, 31, 162-186.

[100] Datta, S., Raza, M. S., Kumar, S., & Saha, P. (2018). Exploring the possibility of dissimilar welding of NiTi to Ti using Yb-fiber laser. Advances in Materials and Processing Technologies, 4(4), 614-625.

[101] Karbasi, H. (2010). COMSOL assisted simulation of laser engraving. In Proceedings of the Comsol Conference, Boston.

[102] Baek, S.H., D. D. Haas, D. B. Kay, D. Kessler, aand K. M. Sanger; Multichannel L Laserthermal printhead technology; Handbook of Optical and Laser Scanning, edited by G. F. Marshall, Marcel Dekker Inc., New York (2004), pp. 711–767.

[103] J. Förster , H. V. Excimer; Laser-annealing of amorphous silicon layers; Excerpt from the Proceedings of the COMSOL Conference,Stuttgart (2011).

[104] Darif, M., Semmar, N., & Orléans Cedex, F. (2008, November). Numerical simulation of Si nanosecond laser annealing by COMSOL multiphysics. In Proceedings of the COMSOL Conference 2008 Hannover (pp. 567-571).

[105] Biswas, A., L. Li, T. K. Maity, U. K. Chatterjee, B. L. Mordike, I. Manna, and J. Dutta Majumdar. "Laser surface treatment of Ti-6Al-4V for bio-implant application." Lasers Eng 17, no. 1-2 (2007): 59-73.

[106] S. Shiva, I.A. Palani, S.K. Mishra, C.P. Paul, L.M. Kukreja,“ Investigations on the influence of composition in the development of NiTi shape memory alloy using laser based additive manufacturing”, Opt Laser Technol, 69, 44-51(2015).

[107] Mahmood, K., Farid, N., Ghauri, I. M., Afzal, N., Idrees, Y., & Mubarik, F. E. (2010). Effects of laser irradiation on the mechanical response of polycrystalline titanium. Physica Scripta, 82(4), 045606.

[108] Yilbas, B. S., Ali, H., Al-Sharafi, A., & Al-Qahtani, H. (2019). Laser processing of Ti6Al4V alloy: wetting state of surface and environmental dust effects. Heliyon, 5(2), 01211.

[109] Nakae, H., Inui, R., Hirata, Y., & Saito, H. (1998). Effects of surface roughness on wettability. Acta materialia, 46(7), 2313-2318.

[110] Welding, Brazing and soldering. ASM Handbook 1993, Vol. 6, ASM International Materials Park, OH.

[111] Liu, L., Huang, R., Song, G., &Hao, X. (2008). Behavior and Spectrum Analysis of Welding Arc in Low-Power YAG-Laser–MAG Hybrid-Welding Process. IEEE Transactions on plasma science, 36(4), 1937-1943.

[112] Takata, Y., Hidaka, S., Cao, J. M., Nakamura, T., Yamamoto, H., Masuda, M., & Ito, T. (2005). Effect of surface wettability on boiling and evaporation. Energy, 30(2-4), 209-220.

[113] Khoo, Z. X., An, J., Chua, C. K., Shen, Y. F., Kuo, C. N., & Liu, Y. (2019). Effect of heat treatment on repetitively scanned SLM NiTi shape memory alloy. Materials, 12(1), 77.

[114] Khoo, Z. X., An, J., Chua, C. K., Shen, Y. F., Kuo, C. N., & Liu, Y. (2019). Effect of heat treatment on repetitively scanned SLM NiTi shape memory alloy. Materials, 12(1), 77.

[115] Ding, K., & Ye, L. (2006). Laser shock peening: performance and process simulation. Woodhead Publishing.

[116] Huang W (2002) On the selection of shape memory alloys for actuators. Materials & Design 23: 11–19.

[117] Liu, Y.; Humbeeck, J.V.; Stalmans, R.; Delaey, L. Some aspects of the properties of NiTi shape memory alloy.J. Alloys Compd. 1997, 247, 115–121.

[118] Ortega, A.M.; Tyber, J.; Frick, C.P.; Gall, K.; Maier, H.J. Cast NiTi shape-memory alloys. Adv. Eng. Mater.2005, 7, 492–507.

[119] Ladani L, Additive Manufacturing of Metals: Materials, Processes, Tests, and Standards, 2020.

[120] Lockett, H, Ding, J, Williams, S, et al . Design for wire arc additive manufacture: Design rules and build orientation selection. J. Eng. Des. 2017;28: 568–598.

[121]Ding D, Pan Z, Cuiuri D et al. A tool-path generation strategy for wire and arc additive manufacturing. Int. J. Adv. Manuf. Technol.2014; 73: 173–183.

[122] Reisgen U, Sharma R, Mann S, et al . Increasing the manufacturing efficiency of WAAM by advanced cooling strategies. Welding in the World, 2020; 64:1409-1416.

[123] Ding D, Pan Z, Cuiuri D et al. A tool-path generation strategy for wire and arc additive manufacturing. Int. J. Adv. Manuf. Technol.2014; 73: 173–183.

[124] Jiang, S Y, Zhang Y Q, Zhao Y N, et al. Influence of Ni_4Ti_3 precipitates on phase transformation of NiTi shape memory alloy. Trans. Nonferrous Met. Soc. China,2015; 25(12): 4063-4071.

[125] Singh S, Subramaniam K, Chittora N, et al. A.Studies on development of NiTi-integrated optical fiber sensor and its life cycle behavior. J Intell Mater Syst Struct 2020; 31(6): 869-881.

[126] Shiva S, Palani I A, Mishra S K, et al . Investigations on the influence of composition in the development of Ni–Ti shape memory alloy using laser based additive manufacturing. Opt Laser Technol 2015; 69: 44-51.

[127] Prabu S M, Madhu H C, Perugu S, et al. Shape memory effect, temperature distribution and mechanical properties of friction stir welded nitinol. J. Alloys Compd.2019; 776: 334-345.

[128] Hooper P A, Melt pool temperature and cooling rates in laser powder bed fusion. Addit. Manuf. 2018; 22:548-559.

[129] Lathers S, La Belle J, Additive Manufactured Biomimicking Actuator with Shape Memory Polymer Composite for Prosthetic Actuators., 3D Print Addit Manuf 2017;4(4): 201-213.

[130] Lehmann, T., Jain, A., Jain, Y., Stainer, H., Wolfe, T., Henein, H., & Qureshi, A. J. (2020). Concurrent geometry-and material-based process identification and optimization for robotic CMT-based wire arc additive manufacturing. Materials & Design, 194, 108841.

[131] Le, V. T., Doan, Q. T., Mai, D. S., Bui, M. C., Tran, H. S., Van Tran, X., & Nguyen, V. A. (2022). Prediction and optimization of processing parameters in wire and arc-based additively manufacturing of 316L stainless steel. Journal of the Brazilian Society of Mechanical Sciences and Engineering, 44(9), 1-16.

[132] Murphy, A. B., Tanaka, M., Yamamoto, K., Tashiro, S., Sato, T., & Lowke, J. J. (2009). Modelling of thermal plasmas for arc welding: the role of the shielding gas properties and of metal vapour. Journal of Physics D: Applied Physics, 42(19), 194006.

[132] Bewerse, C., Emery, A. A., Brinson, L. C., & Dunand, D. C. (2015). NiTi porous structure with 3D interconnected microchannels using steel wire spaceholders. Materials Science and Engineering: A, 634, 153-160.

[133] Jiang HC, Rong LJ. Ways to lower transformation temperatures of porous NiTi shape memory alloy fabricated by self-propagating high-temperature synthesis. Mater Sci Eng A – Struct Mater Prop Microstruct Proc. 2006;438:883–6.

[134] Chu CL, Chung JCY, Chu PK. Effects of heat treatment on characteristics of porous Ni-rich NiTiSMA prepared by SHS technique. Trans Nonferrous Metal Soc China. 2006;16:49–53.

[135] Biswas A. Porous NiTi by thermal explosion mode of SHS: processing, mechanism and generation of single phase microstructure. Acta Mater. 2005;53:1415–25.

[136] Zhao Y, Taya M, Kang YS, Kawasaki A. Compression behavior of porous NiTi shape memory alloy. Acta Mater. 2005;53:337–43.

[137] Lagoudas DC, Vandygriff EL. Processing and characterization of NiTi porous SMA by elevated pressure sintering. J Intel Mater Syst Struct. 2002;13:837–50.

[138] Yuan B, Zhang XP, Chung CY, Zhu M. The effect of porosity on phase transformation behavior of porous Ti–50.8 at.% Ni shape memory alloys prepared by capsule-free hot isostatic pressing. Mater Sci Eng A – Struct Mater Prop Microstruct Proc. 2006;438:585–8.
[139] Bertheville B. Porous single-phase NiTi processed under Ca reducing vapor for use as a bone graft substitute. Biomaterials. 2006;27:1246–50.

[140] Zhu SL, Yang XJ, Fu DH, Zhang LY, Li CY, Cui ZD. Stress-strain behavior of porous NiTi alloys prepared by powders sintering. Mater Sci Eng A – Struct Mater Prop Microstruct Proc. 2005;408:264–8.

[141] Grummon DS, Shaw JA, Gremillet A. Low-density open-cell foams in the NiTi system. Appl Phy Lett. 2003;82:2727–9.

[142] Qiu, C., Yue, S., Adkins, N. J., Ward, M., Hassanin, H., Lee, P. D., ... & Attallah, M. M. (2015). Influence of processing conditions on strut structure and compressive properties of cellular lattice structures fabricated by selective laser melting. Materials Science and Engineering: A, 628, 188-197.

[143] Wolf, T., Fu, Z., & Körner, C. (2019). Selective electron beam melting of an aluminum bronze: Microstructure and mechanical properties. Materials Letters, 238, 241-244.

[144] Lee, J., Choi, J. B., & Choi, K. (1996). Application of homogenization FEM analysis to regular and re-entrant honeycomb structures. Journal of Materials Science, 31(15), 4105-4110.

[145] Alderson, A., Rasburn, J., & Evans, K. E. (2007). Mass transport properties of auxetic (negative Poisson's ratio) foams. physica status solidi (b), 244(3), 817-827.
[146] Robert, F. (1985). An isotropic three-dimensional structure with Poisson’s ratio=− 1. J. Elast, 15, 427-

[147] Liu, L., Zhuang, Z., Liu, F., & Zhu, M. Additive manufacturing of steel–bronze bimetal by shaped metal deposition: interface characteristics and tensile properties. The International Journal of Advanced Manufacturing Technology, (2013), 69(9-12), 2131-2137.

[148]Belyaev S., Rubanik V., Resnina N., Rubanik V. Jr., Demidova E., Lomakin I. Bimetallic shape memory alloy composites produced by explosion welding: Structure and martensitic transformation, Journal of Materials Processing Technology, (2016) , 234 , 323–331.

[149].Konnov, Y. P., Kissel'man, M. A., &Konnova, I. Y.. Electroslag Surfacing with a Vertical Blank to Produce Corrosion Resistant Bimetals. Stal, (1993),(5), 26-30.

[150].Singh, S., Resnina, N., Belyaev, S., Jinoop, A. N., Shukla, A., Palani, I. A., C.P. Paul & Bindra, K. S.. Investigations on NiTi shape memory alloy thin wall structures through laser marking assisted wire arc based additive manufacturing. Journal of Manufacturing Processes, (2021),66, 70-80.

[151] Miranda, R. M., Assunção, E., Silva, R. J. C., Oliveira, J. P., & Quintino, L. Fiber laser welding of NiTi to Ti-6Al-4V. The International Journal of Advanced Manufacturing Technology, (2015), 81(9), 1533-1538.

[152] Oliveira, J. P., Panton, B., Zeng, Z., Andrei, C. M., Zhou, Y., Miranda, R. M., & Fernandes, F. B. (2016). Laser joining of NiTi to Ti6Al4V using a Niobium interlayer. Acta Materialia, 105, 9-15.

[153] Oliveira, J. P., Zeng, Z., Andrei, C., Fernandes, F. B., Miranda, R. M., Ramirez, A. J., ... & Zhou, N. (2017). Dissimilar laser welding of superelastic NiTi and CuAlMn shape memory alloys. Materials & Design, 128, 166-175.

[154] Shamsolhodaei, A., Oliveira, J. P., Schell, N., Maawad, E., Panton, B., & Zhou, Y. N. (2020). Controlling intermetallic compounds formation during laser welding of NiTi to 316L stainless steel. Intermetallics, 116, 106656.

[155] Miyazaki, S., Otsuka, K., & Suzuki, Y.. Transformation pseudoelasticity and deformation behavior in a Ti-50.6 at% Ni alloy. Scripta Metallurgica, (1981),15(3), 287-292.

[156] Attar, H., Ehtemam-Haghighi, S., Kent, D., Wu, X., &Dargusch, M. S. , Comparative study of commercially pure titanium produced by laser engineered net shaping, selective laser melting and casting processes. Materials Science and Engineering: A, (2017), 705, 385-393.

[157] Bartolomeu, F., Costa, M. M., Alves, N., Miranda, G., & Silva, F. S. (2020). Additive manufacturing of NiTi-Ti6Al4V multi-material cellular structures targeting orthopedic implants. Optics and Lasers in Engineering, 134, 106208.

[158] Miranda, R. M., Assunção, E., Silva, R. J. C., Oliveira, J. P., & Quintino, L. Fiber laser welding of NiTi to Ti-6Al-4V. The International Journal of Advanced Manufacturing Technology, (2015), 81(9), 1533-1538.

[159] Zoeram, A. S., & Mousavi, S. A. Laser welding of Ti–6Al–4V to Nitinol. Materials & Design,(2014), 61, 185-190

[160] Ahsan, M. R. U., Tanvir, A. N. M., Ross, T., Elsawy, A., Oh, M. S., & Kim, D. B. Fabrication of bimetallic additively manufactured structure (BAMS) of low carbon steel and 316L austenitic stainless steel with wire+ arc additive manufacturing.(2019) Rapid Prototyping Journal.

[161] Ke, W. C., Oliveira, J. P., Cong, B. Q., Ao, S. S., Qi, Z. W., Peng, B., & Zeng, Z. (2022). Multi-layer deposition mechanism in ultra high-frequency pulsed wire arc additive manufacturing (WAAM) of NiTi shape memory alloys. Additive Manufacturing, 50, 102513.

[162] Zeng, Z., B. Q. Cong, J. P. Oliveira, W. C. Ke, N. Schell, B. Peng, Z. W. Qi, F. G. Ge, W. Zhang, and S. S. Ao. "Wire and arc additive manufacturing of a Ni-rich NiTi shape memory alloy: Microstructure and mechanical properties." Additive manufacturing 32 (2020): 101051.

[163] Lin, Z., Song, K., & Yu, X. (2021). A review on wire and arc additive manufacturing of titanium alloy. Journal of Manufacturing Processes, 70, 24-45.

[164] Zhuo, Y., Yang, C., Fan, C., Lin, S., Chen, Y., Chen, C., & Cai, X. (2021). Grain refinement of wire arc additive manufactured titanium alloy by the combined method of boron addition and low frequency pulse arc. Materials Science and Engineering: A, 805, 140557.

[165] Bermingham, M. J., Thomson-Larkins, J., St John, D. H., & Dargusch, M. S. Sensitivity of Ti-6Al-4V components to oxidation during out of chamber Wire+ Arc Additive Manufacturing. Journal of Materials Processing Technology, (2018), 258, 29-37.

[166] Belyaev S., Rubanik V., Resnina N., Rubanik V., Lomakin I., Demidova E. ,.Reversible strain in bimetallic TiNi-based shape memory composites produced by explosion welding, Materials Today: Proceedings, (2017),4 4696-4701.

[167] Lathers, S., & La Belle, J. Additive Manufactured Biomimicking Actuator with Shape Memory Polymer Composite for Prosthetic Actuators. 3D Printing and Additive Manufacturing, 4(4), (2017), 201-213.

[168]Pieri, K., Felix, B. M., Zhang, T., Soman, P., & Henderson, J. H. (2021). Printing Parameters of Fused Filament Fabrication Affect Key Properties of Four-Dimensional Printed Shape-Memory Polymers. 3D Printing and Additive Manufacturing.

[169] Mirshekari, G. R., Saatchi, A., Kermanpur, A., & Sadrnezhaad, S. K. (2013). Laser welding of NiTi shape memory alloy: Comparison of the similar and dissimilar joints to AISI 304 stainless steel. Optics & Laser Technology, 54, 151-158.

[170] Pouquet, J., Miranda, R. M., Quintino, L., & Williams, S. (2012). Dissimilar laser welding of NiTi to stainless steel. The International Journal of Advanced Manufacturing Technology, 61(1), 205-212.

[171] Wang, J., Pan, Z., Wang, L., Su, L., Carpenter, K., Wang, J., ... & Li, H. (2020). In-situ dual wire arc additive manufacturing of NiTi-coating on Ti6Al4V alloys: Microstructure characterization and mechanical properties. Surface and Coatings Technology, 386, 125439.

[172] Li, H., Sun, D., Cai, X., Dong, P., & Gu, X. (2013). Laser welding of TiNi shape memory alloy and stainless steel using Co filler metal. Optics & Laser Technology, 45, 453-460.

[173] Gugel, H., Schuermann, A., & Theisen, W. (2008). Laser welding of NiTi wires. Materials Science and Engineering: A, 481, 668-671.

[174] Liu, Y. J., Wang, H. L., Li, S. J., Wang, S. G., Wang, W. J., Hou, W. T., ... & Zhang, L. C. (2017). Compressive and fatigue behavior of beta-type titanium porous structures fabricated by electron beam melting. Acta Materialia, 126, 58-66.

[175]Joshi, G. R., & Badheka, V. J. (2019). Processing of bimetallic steel-copper joint by laser beam welding. Materials and Manufacturing Processes, 34(11), 1232-1242.

[176] Zeng, Z., Oliveira, J. P., Yang, M., Song, D., & Peng, B. (2017). Functional fatigue behavior of NiTi-Cu dissimilar laser welds. Materials & Design, 114, 282-287.

[177] Zeng, Z., Oliveira, J. P., Yang, M., Song, D., & Peng, B. (2017). Functional fatigue behavior of NiTi-Cu dissimilar laser welds. Materials & Design, 114, 282-287.

[178] Z. Zeng, B. Panton, J. P. Oliveira, A. Han, Y.N. Zhou, Dissimilar laser welding of NiTi shape memory alloy and copper. Smart. Mater. Struct. 24 (2015) 1–8.

[179] Singh, S., Demidova, E., Resnina, N., Belyaev, S., Palani, I. A., Paul, C. P., & Prashanth, K. G. (2022). Mechanical Properties, Microstructure, and Actuation Behavior of Wire Arc Additive Manufactured Nitinol: Titanium Bimetallic Structures. 3D Printing and Additive Manufacturing.

[180] Mohamed, O. A., Masood, S. H., & Xu, W. (2022). Nickel-titanium shape memory alloys made by selective laser melting: a review on process optimisation. Advances in Manufacturing, 1-35.

[181] Z. Zeng, B. Panton, J. P. Oliveira, A. Han, Y.N. Zhou, Dissimilar laser welding of NiTi shape memory alloy and copper. Smart. Mater. Struct. 24 (2015) 1–8.

[182] Spierings, A. B., Herres, N., & Levy, G. (2011). Influence of the particle size distribution on surface quality and mechanical properties in AM steel parts. Rapid Prototyping Journal.

[183] Uzan, N.E.; Shneck, R.; Yeheskel, O.; Frage, N. Fatigue of AlSi10Mg specimens fabricated by additive manufacturing selective laser melting (AM-SLM). Mater. Sci. Eng. A 2017, 704, 229–237.

[184] Chu, F., Zhang, K., Shen, H., Liu, M., Huang, W., Zhang, X., ... & Huang, A. (2021). Influence of satellite and agglomeration of powder on the processability of AlSi10Mg powder in Laser Powder Bed Fusion. Journal of Materials Research and Technology, 11, 2059-2073.

[185] Spears, T. G., & Gold, S. A. (2016). In-process sensing in selective laser melting (SLM) additive manufacturing. Integrating Materials and Manufacturing Innovation, 5(1), 16-40.

[186] Han, Q., Setchi, R., & Evans, S. L. (2017). Characterisation and milling time optimisation of nanocrystalline aluminium powder for selective laser melting. The International Journal of Advanced Manufacturing Technology, 88(5), 1429-1438.

[187] Han, Q., Setchi, R., & Evans, S. L. (2017). Characterisation and milling time optimisation of nanocrystalline aluminium powder for selective laser melting. The International Journal of Advanced Manufacturing Technology, 88(5), 1429-1438.

[188]J.D.Majumdar, R.Galun, B.L.Mordike, I.Manna, Effect of laser surface melting on corrosion and wear resistance of a commercial magnesium alloy, Mater.Sci. Eng. A61 (2013)119–1292003.

[189] Ma, Z., Zhang, K., Ren, Z., Zhang, D. Z., Tao, G., & Xu, H. (2020). Selective laser melting of Cu–Cr–Zr copper alloy: Parameter optimization, microstructure and mechanical properties. Journal of Alloys and Compounds, 828, 154350.

[190] Kitano, H., Kusano, M., Tsujii, M., Yumoto, A., & Watanabe, M. (2021). Process parameter optimization framework for the selective laser melting of hastelloy X alloy considering defects and solidification crack occurrence. *Crystals*, *11*(6), 578.

[191] Wang, Z., Xiao, Z., Tse, Y., Huang, C., & Zhang, W. (2019). Optimization of processing parameters and establishment of a relationship between microstructure and mechanical properties of SLM titanium alloy. Optics & Laser Technology, 112, 159-167.

[192] Singh, S., Palani, I. A., Paul, C. P., Funk, A., & Konda Gokuldoss, P. (2022). Wire Arc Additive Manufacturing of NiTi 4D Structures: Influence of Interlayer Delay. 3D Printing and additive manufacturing.

[193] Guan, L., Wei, Z., Mao, H., Duan, R., Zhang, W., Hou, J., & Xu, H. (2020). Influence of Hot Isostatic Pressing Temperature on the Microstructure and Properties of AlSi7Cu2Mg Alloys. Journal of Wuhan University of Technology-Mater. Sci. Ed., 35(6), 1135-1141.

[194] De Damborenea, J. (1998). Surface modification of metals by high power lasers. Surface and Coatings Technology, 100, 377-382.

[195] da Silva, M. R., Gargarella, P., Gustmann, T., Botta Filho, W. J., Kiminami, C. S., Eckert, J., & Bolfarini, C. (2016). Laser surface remelting of a Cu-Al-Ni-Mn shape memory alloy. Materials Science and Engineering: A, 661, 61-67.

[196] Singh, S., Palani, I. A., Paul, C. P., Funk, A., & Konda Gokuldoss, P. (2022). Wire Arc Additive Manufacturing of NiTi 4D Structures: Influence of Interlayer Delay. 3D Printing and additive manufacturing.

[197] Alagha, A. N., Hussain, S., & Zaki, W. (2021). Additive manufacturing of shape memory alloys: A review with emphasis on powder bed systems. Materials & Design, 204, 109654.

[198] Wang, G., Lang, L. H., Yu, W. J., Huang, X. N., & Li, F. (2016). Influences of hot-isostatic-pressing temperature on the microstructure, tensile properties and tensile fracture mode of 2A12 powder compact. Acta Metallurgica Sinica, 29(10), 963-974

[199] Guan, L., Wei, Z., Mao, H., Duan, R., Zhang, W., Hou, J., & Xu, H. (2020). Influence of Hot Isostatic Pressing Temperature on the Microstructure and Properties of AlSi7Cu2Mg Alloys. Journal of Wuhan University of Technology-Mater. Sci. Ed., 35(6), 1135-1141.

[200] Khomutov, M., Potapkin, P., Cheverikin, V., Petrovskiy, P., Travyanov, A., Logachev, I., & Smurov, I. (2020). Effect of hot isostatic pressing on structure and properties of intermetallic NiAl–Cr–Mo alloy produced by selective laser melting. Intermetallics, 120, 106766.